

# Investigation of the Effect of Transient and Temporal Variations on Magnetic Reconnection

Using Kinetic PIC Simulations

---

Susanne Flø Spinnangr

Thesis for the degree of Philosophiae Doctor (PhD)  
University of Bergen, Norway  
2023

UNIVERSITY OF BERGEN



# **Investigation of the Effect of Transient and Temporal Variations on Magnetic Reconnection**

## Using Kinetic PIC Simulations

Susanne Flø Spinnangr



Thesis for the degree of Philosophiae Doctor (PhD)  
at the University of Bergen

Date of defense: 05.05.2023

© Copyright Susanne Flø Spinnangr

The material in this publication is covered by the provisions of the Copyright Act.

Year: 2023

Title: Investigation of the Effect of Transient and Temporal Variations on Magnetic Reconnection

Name: Susanne Flø Spinnangr

Print: Skipnes Kommunikasjon / University of Bergen

# Acknowledgements

During my time as a PhD student I have had three amazing supervisors. Michael Hesse, Paul Tenfjord and Cecilia Norgren, thank you for all your help, advice and support you have given me these four years! You have all gone above and beyond what was professionally required of you in your position, and I am truly grateful. Thank you Michael, for recognising my potential and encouraging me to apply for this PhD position, for everything you have taught me since, and for inspiring me to pursue difficult subjects. Thank you Paul and Cecilia, for always being ready and able to answer all my questions about science and beyond, for always generously sharing your time, insight and knowledge, and for all your help you have provided me with. Also, thank you Paul for being a great friend, and for being so patient with me every time you had to help me figure out how to make MATLAB do what I wanted it to do. Your ability to magically make computers stop messing around by just walking into the room is still a mystery to me.

Michael, Paul and Cecilia, you have all been wonderful leaders of our little research group. You have created a welcoming and safe work environment where everyone can feel free to express their opinions and share ideas, and to contribute to the progress of the whole group. And the rest of the SPPG group, thank you for contributing to make our group the best group at UiB. Thank you Håkon for being a perfect office mate! We've had some great and interesting discussions about plasma physics, the meaning of life and everything in between! Thank you Norah, Therese, Judit and Tai for all your insights, contributions and interesting conversations over the years.

Finally, thank you to my wonderful family and friends! Dave, thank you for agreeing to proofread, and putting in much more effort and attention to detail than I ever expected. Mom, Dad, Joakim, thank you for all your encouragement, support, patience and for keeping me relatively sane. Without you this thesis would never have been written.

Susanne Flø Spinnangr  
Bergen, February 2023



# Abstract

The vast majority of the Universe consists of different plasma environments. These are permeated by electromagnetic fields generated by the motion of the charged plasma particles. Since the plasma particles are free, their dynamics are often governed by their interaction with the collective electric and magnetic fields, rather than individual particle-particle interactions. One such interaction is called *magnetic reconnection*. It is arguably the most important plasma acceleration process in our near space environment, as well as in solar and different astrophysical plasma. Magnetic reconnection converts energy stored in magnetic fields into heat and bulk motion of the plasma particles through changes in the magnetic connectivity. It is facilitated by complex interactions between the electromagnetic fields and the charged plasma particles, and occurs in many different plasma environments and over vastly different spatial and temporal scales. This PhD-thesis is the result of four years of dedicated research of magnetic reconnection using fully kinetic Particle-In-Cell simulations. The goal has been to add pieces to the puzzle of knowledge and understanding of the physics of magnetic reconnection, which has been accumulated over decades of research by the scientific community.

We have investigated how magnetic reconnection is influenced by transient variations in the inflow regions, both in particle composition and magnetic field configuration. In paper I, we simulate a reconnection event including a dense population of cold ions in the inflow region. In paper II, we simulate a reconnection event where the direction of the inflow magnetic field is changed during reconnection. These two investigations show that the reconnection process is affected by the transient changes in the inflow conditions on both large and small scales. By close inspection of the small scale dynamics of the plasma particles and the electromagnetic fields, we explain how the large and small scale effects of the variations are connected. In paper I, the temporal inertia of the ions due to counter-streaming is shown to be the mediator between the different scales. In paper II, large scale, non-linear variations in the reconnection rate are shown to be caused by spatio-temporal changes in the inflow flux transport due to modifications of the magnetic tension. Additionally, the variations in the inflow region are shown to cause the outflow to be less laminar, with various signatures of the inflow variations surviving the

reconnection process. In paper III, we investigate how magnetic reconnection can initiate in a current sheet which is initially stable. By driving the simulation with an electric field at the boundaries, reconnection is initiated without an initial magnetic field perturbation imposed in the current sheet. We identify two characteristic signatures of reconnection onset in the electron phase-space distributions which were present immediately before the onset of reconnection took place. These signatures correspond to small scale changes in the electron dynamics associated with the thinning of the current sheet and acceleration by the out-of-plane electric field. The results of the research in these three papers contribute to the larger goal of collectively accumulating a full understanding of magnetic reconnection as a ubiquitous, physical process.

# Abstrakt

Vårt univers består for det meste av forskjellige plasmamiljø. Disse er gjennomsyret av elektromagnetiske felt som er generert av plasmapartiklenes bevegelser. Fordi plasmapartiklene er frie partikler vil dynamikken deres hovedsakelig være styrt av interaksjonen mellom dem og de kollektive elektromagnetiske feltene, ikke interaksjonene mellom individuelle partikler. Én slik interaksjon mellom plasmapartikler og elektromagnetiske felt kalles *magnetisk omkobling*. Man kan påstå at dette er den viktigste plasmapartikkel-akselerasjonsprosessen i vårt nære verdensrom, så vel som i forskjellige astrofysiske og solare plasma. Magnetisk omkobling konverterer energi lagret i magnetfeltene til varme og bevegelse av plasmapartiklene gjennom endringer i den magnetiske forbindelsen. Dette er fasilitert av komplekse interaksjoner mellom de elektromagnetiske feltene og de ladde plasmapartiklene, og det skjer i en rekke forskjellige plasmamiljø og over svært forskjellige romlige og temporale størrelsesordener. Denne doktorgradsavhandlingen er et resultat av fire år med dedikert forskning på magnetisk omkobling gjennom kinetiske Particle-In-Cell simulasjoner. Målet har vært å bidra med flere biter til puslespillet av kunnskap og forståelse rundt fysikken bak magnetisk omkobling som har blitt akkumulert gjennom flere tiår med forskning gjort av det vitenskapelige miljøet.

Vi har undersøkt hvordan magnetisk omkobling påvirkes av forbigående variasjoner i innstrømningsregionene, både i partikkelkomposisjonen og i konfigurasjonen til det magnetiske feltet. I artikkel I simulerer vi en omkoblingshendelse som inkluderer en tett populasjon av kalde ioner i innstrømningsregionene. I artikkel II simulerer vi en omkoblingshendelse hvor retningen på det magnetiske feltet endrer seg i løpet av omkoblingsprosessen. Begge disse undersøkelsene viser at omkoblingsprosessen blir påvirket av disse forbigående endringene i innstrømningstilstandene på både store og små skalaer. Ved å nøye undersøke dynamikken til plasmapartiklene på små skalaer forklarer vi hvordan effektene på store og små skalaer er koblet sammen. I artikkel I viser vi at det temporale tregghetsmomentet til ionene forårsaket av motgående partikkelbevegelser er opphavet til kommunikasjonen mellom de forskjellige skalaene. I artikkel II viser vi at store, ikke-lineære variasjoner i omkoblingsraten er forårsaket av romlig-temporale endringer i flukstransporten inn til omkoblingen, som igjen kommer



av modifikasjoner i den magnetiske spenningskraften. Videre viser vi at variasjonene i innstrømningsregionen gjør utstrømningsregionen mindre laminær, og flere signaturer av innstrømningsvariasjonene overlever omkoblingsprosessen. I artikkel III undersøker vi hvordan magnetisk omkobling kan starte i et strømnings sjikt som i utgangspunktet er stabilt. Ved å drive simulasjonen med et elektrisk felt langs grensene startes magnetisk omkobling uten bruk av en magnetisk perturbasjon i strømnings sjiktet. Vi identifiserer to karakteristiske signaturer på at omkobling starter i elektronfordistribusjonene i fase-rommet som er tilstede rett før omkoblingen starter. Disse signaturene korresponderer til småskala endringer i elektronenes dynamikk assosiert med at strømnings sjiktet blir tynnere og med akselerasjon fra det elektriske feltet som peker ut av planet. Resultatene av forskningen i disse tre artiklene bidrar til det overordnede målet om å til sammen akkumulere en full forståelse av magnetisk omkobling som en fysisk prosess som eksisterer overalt.

# Outline

This thesis and the three published papers included are submitted for the degree of philosophiae doctor (PhD) in physics at the Department of Physics and Technology, University of Bergen.

The thesis consists of an introductory part and three scientific papers published in international peer reviewed journals.

**Paper I** S.F. Spinnangr, M. Hesse, P. Tenfjord, C. Norgren, H.M. Kolstø, N. Kwagala, T.M. Jørgensen, *The Micro-Macro Coupling of Mass-Loading in Symmetric Magnetic Reconnection with Cold Ions*, Geophysical Research Letters, Vol. 48, Issue 13  
doi:10.1029/2020GL090690, 2021

**Paper II** S.F. Spinnangr, P. Tenfjord, M. Hesse, C. Norgren, H.M. Kolstø, N. Kwagala, T.M. Jørgensen, J.P. Jiménez, *Asymmetrically varying guide field during magnetic reconnection: Particle-In-Cell simulations*, Journal of Geophysical Research: Space Physics, Vol. 127, Issue 1  
doi:10.1029/2021JA029955, 2021

**Paper III** S.F. Spinnangr, M. Hesse, P. Tenfjord, C. Norgren, H.M. Kolstø, N. Kwagala, T.M. Jørgensen, T. Phan, *Electron behavior around the onset of magnetic reconnection*, Geophysical Research Letters, Vol. 49, Issue 23  
doi:10.1029/2022GL102209, 2022

During my PhD studies, I have also contributed to the following papers.

- A P. Tenfjord, M. Hesse, C. Norgren, S.F. Spinnangr, H.M. Kolstø, *The Impact of Oxygen on the Reconnection Rate*, Geophysical Research Letters, Vol. 46, Issue 12  
doi:10.1029/2019GL082175, 2019
- B H.M. Kolstø, M. Hesse, C. Norgren, P. Tenfjord, S.F. Spinnangr, N. Kwagala, *Collisionless Magnetic Reconnection in an Asymmetric Oxygen Density Configuration*, Geophysical Research Letters, Vol. 47, Issue 1  
doi:10.1029/2019GL085359, 2020
- C N. Kwagala, M. Hesse, T. Moretto, P. Tenfjord, C. Norgren, G. Toth, T. Gombosi, H. M. Kolstø, S.F. Spinnangr, *Validating the Space Weather Modeling Framework (SWMF) for applications in northern Europe - Ground magnetic perturbation validation*, Journal of Space Weather Space Climate, Vol. 10  
doi:10.1051/swsc/2020034, 2020
- D P. Tenfjord, M. Hesse, C. Norgren, S.F. Spinnangr, H.M. Kolstø, N. Kwagala, *Interaction of Cold Streaming Protons with the Reconnection Process*, Journal of Geophysical Research, Vol. 125, Issue 6  
doi:10.1029/2019JA027619, 2020
- E H.M. Kolstø, M. Hesse, C. Norgren, P. Tenfjord, S.F. Spinnangr, N. Kwagala, *On the Impact of a Streaming Oxygen Population on Collisionless Magnetic Reconnection*, Geophysical Research Letters, Vol. 47, Issue 22  
doi:10.1029/2020GL089462, 2020
- F M. Hesse, C. Norgren, P. Tenfjord, J.L. Burch, Y.H. Liu, L.J. Chen, S. Wang, H.M. Kolstø, S.F. Spinnangr, R. Ergun, T. Moretto, N. Kwagala, *A New Look at the Electron Diffusion Region in Asymmetric Magnetic Reconnection*, Journal of Geophysical Research, Vol. 126, Issue 2  
doi:10.1029/2020JA028456, 2020
- G C. Norgren, P. Tenfjord, M. Hesse, S. T. Redondo, W.Y. Li, N. Kwagala, S.F. Spinnangr, H.M. Kolstø, T. Moretto, *On the Pres-*

---

*ence and Thermalization of Cold Ions in the Exhaust of Antiparallel Symmetric Reconnection*, *Frontiers in Astronomy in Space Sciences*

doi:10.3389/fspas.2021.730061, 2021

H H.M. Kolstø, C. Norgren, M. Hesse, L.J. Chen P. Tenfjord, S.F. Spinnangr, N. Kwagala, *Magnetospheric Multiscale Observations of an Expanding Oxygen Wave in Magnetic Reconnection* *Geophysical Research Letters*, Vol. 48, Issue 19

doi:10.1029/2021GL095065, 2021

I J.P. Jiménez, P. Tenfjord, M. Hesse, C. Norgren, N. Kwagala, H.M. Kolstø, S.F. Spinnangr, *The Role of Resistivity on the Efficiency of Magnetic Reconnection in MHD*, *Journal of Geophysical Research*, Vol. 127, Issue 6

doi:10.1029/2021JA030134, 2022



# Contents

Acknowledgements	i
Abstract	iii
Abstrakt	v
Outline	vii
<b>1 Introduction</b>	<b>1</b>
1.1 Objective . . . . .	2
1.2 Outline . . . . .	3
<b>2 Some plasma physics</b>	<b>5</b>
2.1 Plasma, the fourth state of matter . . . . .	6
2.1.1 Near Earth plasma environments . . . . .	8
2.2 Single particle motion . . . . .	10
2.2.1 Single particle motion in external fields . . . . .	11
2.3 Kinetic plasma theory . . . . .	13
2.4 Fluid plasma description . . . . .	16
<b>3 Magnetic reconnection</b>	<b>23</b>

3.1	Early reconnection models . . . . .	28
3.2	Kinetic and multi-fluid model of reconnection . . . . .	32
<b>4</b>	<b>Studying Magnetic Reconnection through Numerical Simulation</b>	<b>47</b>
4.1	Particle-In-Cell simulation . . . . .	48
4.1.1	Macroparticles . . . . .	49
4.1.2	The cell grid . . . . .	54
4.1.3	Time evolution . . . . .	58
4.1.4	Normalization and stability . . . . .	63
<b>5</b>	<b>Introduction to the papers</b>	<b>65</b>
5.1	Paper I: The Micro-Macro Coupling of Mass-Loading in Symmetric Magnetic Reconnection with Cold Ions . . . . .	65
5.2	Paper II: Asymmetrically varying guide field during magnetic reconnection: Particle-In-Cell simulations . . . . .	66
5.3	Paper III: Electron behaviour around the onset of magnetic reconnection	67
<b>6</b>	<b>Conclusions and Future Prospects</b>	<b>69</b>
6.1	Conclusions . . . . .	69
6.2	Future prospects . . . . .	70
<b>7</b>	<b>Scientific results</b>	<b>87</b>
	<b>Paper I: The Micro-Macro Coupling of Mass-Loading in Symmetric Magnetic Reconnection with Cold Ions</b>	<b>89</b>
	<b>Paper II: Asymmetrically varying guide field during magnetic reconnection: Particle-In-Cell simulations</b>	<b>101</b>
	<b>Paper III: Electron behavior around the onset of magnetic reconnection</b>	<b>117</b>

# Chapter 1

## Introduction

Electromagnetic fields and plasma are found everywhere in the Universe, and their dynamics and interplay is an important factor in shaping space as we know it. Magnetic reconnection is a ubiquitous phenomenon where stored magnetic energy is converted into thermal and kinetic energy in the surrounding plasma (e.g. *Cassak and Shay, 2007; Dungey, 1961; Hesse and Schindler, 1988; Parker, 1957; Paschmann et al., 1979; Vasyliunas, 1975*). In many ways, magnetic reconnection can be considered a magnetic explosion. It is facilitated through a macroscopic change in the magnetic field topology, where an initially sheared configuration of the magnetic field is changed through complex kinetic processes taking place in a comparatively small region. Several plasma processes exhibiting particle acceleration, heating and large magnetic geometry changes are believed to be driven by magnetic reconnection, such as relativistic jets, solar flares, black hole flares, magnetospheric substorms, and the aurora, as well as sawtooth crashes in laboratory plasma on Earth (e.g. *Angelopoulos et al., 2008, 2020; Masuda et al., 1994; Ripperda et al., 2022; Shibata and Magara, 2011; Sironi et al., 2015; Yamada et al., 2010; Zweibel and Yamada, 2009*).

In the Earth's near space environment, magnetic reconnection is well known to occur both on the dayside and nightside of our magnetosphere (e.g. *Burch et al., 2016; Eastwood et al., 2010; Ergun et al., 2018; Fuselier and Lewis, 2011; Fuselier et al., 2010*). This allows for the coupling of the Earth's magnetic field with the Interplanetary Magnetic Field from the Sun, and facilitates the entry of plasma from the solar wind into the Earth's magnetosphere. The resulting energy release from reconnection into our magnetosphere has been estimated to reach up to  $10^{16} J$  (*Weiss et al., 1992*), which may give rise to large perturbations in the planetary magnetic field, which can induce strong voltages leading to currents in power grids on the Earth. This is part of a collection of phenomena referred to as space weather, which poses a risk to our highly electrified society on



Earth, as well as to equipment on satellites and astronauts in orbit. Since magnetic reconnection is the driving mechanism behind much of the large and small scale dynamics of our near space environment and the sun, it is imperative that we understand when, where, and how it occurs.

## 1.1 Objective

The objective of this thesis and the included research papers is to add to our collective scientific understanding of magnetic reconnection as a physical process. Magnetic reconnection is a significantly multi-scale phenomenon, with large scale topology changes and energy conversion being facilitated by processes occurring on comparatively microscopic scales. The coupling between what happens on the small, fast scales with the large, slow scales is not obvious, and is still not fully understood. This question goes hand in hand with the questions of what triggers magnetic reconnection, and what ultimately shuts it down. By investigating reconnection through specially designed Particle-In-Cell simulations, this thesis aims to be a contribution to our understanding of this ubiquitous physical process.

In Paper I, we compare two simulations of symmetric magnetic reconnection, where one simulation contains a population of cold ions in the inflow regions. This front of cold ions is propagated towards the current sheet, and eventually participates in the reconnection process. Such fronts of cold ions can be the result of for example ionospheric outflow or plasmaspheric plumes. We found that this impacts the reconnection rate, which is a large scale property, and the aspect ratio of the diffusion region, which is a small scale property. The communication between the large and small scale scales was found to be facilitated through the temporal inertia of the cold ion population.

In paper II, we compare two simulations of magnetic reconnection where one simulation contains variations in the magnetic field direction in one inflow region. These field variations were initiated some distance from the current sheet and propagated inwards and eventually participated in the reconnection process. Such field variations can for example originate in dayside reconnection due to variations in the Interplanetary Magnetic Field. We found that this impacts the reconnection rate in a non-linear fashion due to information about the field changes being propagated in front of the actual variations. This was facilitated by the magnetic tension force. We also found that the variations in the reconnection inflow has an effect on the reconnection outflow.

In paper III, we simulate reconnection onset in a tail-like configuration by driving the

simulation with an electric field driver at the boundaries. This is similar to how the geomagnetic tail is loaded with magnetic field by the solar wind. We identified non-gyrotropic signatures and signatures of acceleration in the electron distribution functions that could be indicative of an imminent reconnection onset. These features were shown to originate from acceleration by the out-of-plane electric field.

## 1.2 Outline

In chapter 2, some fundamental concepts about the physics of plasma are outlined, including what defines a plasma, where we find it in nature, and different descriptions of the interaction between the charged plasma particles and the electromagnetic fields. This is needed as a theoretical foundation to discuss magnetic reconnection. In chapter 3, magnetic reconnection as a physical phenomenon is discussed. Both historical and the modern kinetic models used to describe reconnection are introduced, and concepts fundamental for understanding the research in the three papers are presented. Naturally, since magnetic reconnection is such a diverse and intricate process, many important aspects of it will not be discussed, as it falls outside the scope of the thesis. The purpose of this chapter is to lay out a theoretical foundation for understanding the research that is later presented in the three papers. In chapter 4, the method of study we have used is presented. We have used a fully kinetic Particle-In-Cell code to simulate magnetic reconnection under different conditions, and the basic concepts of how the code solves this is presented. Finally, chapter 5 contains a brief summary of the research and results of the three papers included in this thesis, and chapter 6 contains the conclusions of the thesis, and some musings of the future prospects of research in this context.



# Chapter 2

## Some plasma physics

In our day to day life on Earth, we are used to consider the world as consisting of three different states of matter; solids, liquids, and gases. Almost everything we normally come into contact with, be that natural or man-made objects, can be sorted into one or more of these three categories. However, on a cosmic scale, "normal" matter is actually far less abundant than we would expect based on our everyday experiences. Less than 1% of the matter in the Universe is in one of these three states of matter! The rest exists in a fourth state of matter, called *plasma* (*Baumjohann and Treumann, 2012*). In general, just as an element or substance can undergo a phase transformation from solid to liquid to gas through an increase of energy, further increasing the energy of a gas can cause gas atoms or molecules to break apart into its constituent particles. When this happens, the particles become ionised, and the fourth state is reached, an ionised gas.

Plasma can look extremely different depending on the condition it is in. In space, both the stars and the seemingly empty space between them are made of plasma, just with vastly different temperatures and densities. The Earth is surrounded by a magnetic field and a surrounding plasma called a *Magnetosphere*, which again is constantly being bombarded with outflowing plasma and the co-moving magnetic field from the Sun called the *Solar Wind*. Even on the Earth, plasma can be found in man-made objects like neon lights, old plasma TVs, and nuclear fusion reactors, as well as in nature, for example lightning. Since all these different environments are defined as being in a plasma state, it can seem like a plasma is not a well defined concept. However, the criteria for defining a plasma are actually highly specific and clearly defined. In the next section, a thorough description of what a plasma is will be provided, followed by descriptions of how a plasma and its particles behave.

## 2.1 Plasma, the fourth state of matter

As stated in the introduction of this chapter, a plasma is an ionised gas. A normal gas of neutral particles is defined as a state of matter where the individual gas particles are free. A particle is considered free when its random kinetic energy is much higher than the potential energy from its closest neighbours. This means a gas particle is free to move without significant influence from the forces acting upon it from the other particles in the gas, barring particle collisions. A plasma is a more complicated system, as it contains charged ions which all produce their own, and are affected by each others electromagnetic fields. In nature, plasma can contain both neutral and charged particles which will interact with each other through collisions, and the charged particles additionally interact with each other through electromagnetic forces. Even though a plasma contains charged particles, it appears neutral on a large scale. This is because the number of positive and negative charge carriers in a given volume element of the plasma are roughly the same, making a plasma *quasineutral*.

There are three general plasma criteria that must be met in order for the ionized gas to be considered a plasma. The first regards the length scale of the plasma, the second regards the number of particles in the plasma, and the third is a criterion of the time scale between particle collisions.

For the plasma to appear neutral on large scales, the electric potential from each of the charge carriers must be shielded by the potential from the other charge carriers in the volume element with opposite charge. Each charge carrier carries an electric potential equal to the *Coloumb potential*, given by

$$\phi_C = \frac{q}{4\pi\epsilon_0 r} \quad (2.1)$$

where  $q$  is the charge of the particle,  $\epsilon_0$  is the free space permittivity and  $r$  is the distance from the particle. In a quasineutral plasma, the potential from each charge carrier is shielded by the other charges, and the new potential includes a shielding exponential function

$$\phi_D = \frac{q}{4\pi\epsilon_0 r} e^{-\frac{r}{\lambda_D}} \quad (2.2)$$

This new potential is the *Debye potential*, which tends to 0 when  $r > \lambda_D$ , i.e. at a distance away from the charge larger than *the Debye length*. Figure 2.1 shows a comparison between the Coloumb and Debye potential as a function of the distance from the charge. Close to the charge, the two potentials converge, while the Debye potential tends to 0 at distances greater than the Debye length. For any charge separation there will be an

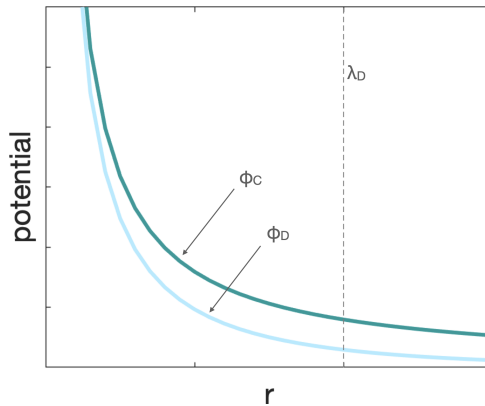


Figure 2.1: A comparison between the Coloumb and Debye potential as a function of  $r$ . The Debye length is marked by the dashed line.

electrostatic potential energy serving to bring the charges back together. At the same time, all the charges have random thermal movement in the gas which tends to perturb the charge neutrality. The Debye length is defined as the distance from any charge for which there is a balance between these forces. It is derived from Poisson's equation of a quasineutral plasma of protons and electrons with equal temperatures into which a positive charge is inserted, and Boltzmann's equation for the density of the electrons in the plasma, such that

$$\lambda_D = \sqrt{\frac{\epsilon_0 k_B T_e}{n_0 e^2}} \quad (2.3)$$

where  $k_B$  is the Boltzmann constant,  $e$  is the electron charge,  $T_e$  is the electron temperature in the plasma, and  $n_0$  is the quasineutral density of the ambient plasma. The first plasma criterion is that the physical dimensions of the system,  $L$ , must be much larger than the Debye length to ensure that the plasma is quasineutral

$$\text{First plasma criterion : } L \gg \lambda_D \quad (2.4)$$

Ensuring quasineutrality is also the root of the second plasma criterion. The shielding of charge on distances larger than the Debye length is a collective effect, meaning its effect depends on the number of particles present in a given volume element. In a spherical volume element with a radius equal to the Debye length, a *Debye sphere*, the number of particles is given by the volume of the sphere times the particle density. The *plasma parameter*,  $\Lambda$ , is defined as the product of the particle density and the Debye length cubed, and defines the second plasma criterion

$$\text{Second plasma criterion : } \Lambda = n_e \lambda_D^3 \gg 1 \quad (2.5)$$

This criterion also ensures that the particles in the plasma are free particles. As previously mentioned, a particle is free if the average potential energy on it from its closest neighbour, which is proportional to  $n_e^{1/3}$ , is much less than the average thermal energy of the particle, which is proportional to  $k_B T_e$ . By substituting equation 2.3 into the second plasma criterion, the resulting expression shows this explicitly

$$n_e^{-1/3} \frac{\epsilon_0 k_B T_e}{e^2} \gg 1 \quad (2.6)$$

The final plasma criterion is relevant for partially ionized plasma, which are plasma that consists of a mixture of charged and neutral particles. If the charge neutrality of the plasma is disturbed in any way, the light and mobile electrons will move to restore it. Even though the electrons have very little mass they still carry some inertia, which causes them to collectively oscillate around the equilibrium distance from the ions at a frequency called *the plasma frequency*. By considering the continuity of the particle density, the conservation of particle momentum and Poisson's law it can be shown that this collective oscillation of the electrons around the ions is a linear oscillator who's angular frequency is the plasma frequency, given by

$$\omega_{pe} = \sqrt{\frac{n_e e^2}{m_e \epsilon_0}} \quad (2.7)$$

When the electrons are oscillating in a plasma containing neutral particles, it is essential that the number of collisions between the neutrals and the electrons remains low enough for the electrons to still be free particles. This means that the characteristic time between electron-neutral collisions,  $\tau_n$ , must be larger than the characteristic time of the electron oscillations. This defines the third plasma criterion

$$\text{Third plasma criterion : } \omega_{pe} \tau_n \gg 1 \quad (2.8)$$

### 2.1.1 Near Earth plasma environments

As mentioned initially in this chapter, different plasma environments can have vastly different macroscopic properties like temperature and density. The Earth is constantly affected by several different plasma environments, which can profoundly influence life on Earth. The most visible and perhaps most influential plasma is the Sun itself, who's nuclear fusion reactions provide light and heat, and fuels all life on Earth. A less known plasma for most people provided by the Sun is the Solar Wind. It is a constant outflow of solar plasma, coupled with the solar magnetic field which bombards the Earth with electrons and protons at a velocity of about 500 *km/s* and magnetic field strength of

around  $5\text{ nT}$  (*Baumjohann and Treumann, 2012*). This magnetic field from the Sun that moves with the solar wind is called the *Interplanetary Magnetic Field* (IMF).

The Earth is surrounded by its own magnetic field and plasma environment, called *the Magnetosphere*. Dynamics in the interior of the Earth generates a dipole magnetic field around the globe. In this field, different species of plasma particles are trapped, but the most common ones are protons, electrons and some oxygen and helium ions resulting from outflow from *the Ionosphere*. The ionosphere is another plasma environment closer to the Earth, consisting of a mix of charged particles and neutrals. The Magnetosphere is not uniform and consists of regions of different magnetic field strength, plasma density, temperature, and pressure.

When the solar wind impacts on the dipole magnetic field of the Earth it is shocked and deflected around it, forming the *Bow Shock* and the *Magnetosheath* inside of it. The kinetic pressure of this impact causes the side of the dipole facing the Sun to be compressed (e.g. *Baumjohann and Treumann, 2012; Piddington, 1960*), increasing the magnetic field strength in this region to  $\sim 20\text{ nT}$  (*Toledo-Redondo et al., 2021*). The boundary between the shocked solar wind and the magnetosphere is called the *Magnetopause*. On the other side of the Earth, the dipole is stretched far away by the solar wind, forming the *Magnetotail*, which stretches many hundreds of Earth radii long. Figure 2.2 shows a very simplified rendition of the impact of the solar wind on the shape of the Earth's magnetosphere.

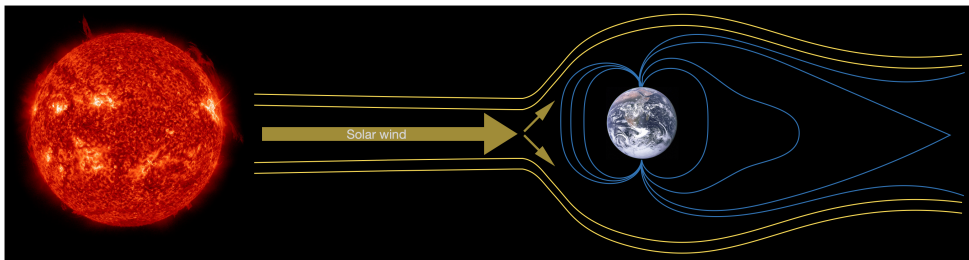


Figure 2.2: A simple artistic rendition of the shape of the Earth's magnetic field under the influence of the Solar wind.

Along the mid-plane of the magnetotail there is region of higher plasma density called the *Plasma sheet*, inside of which a duskward current is induced due to the opposite alignment of the magnetic field in the northern and southern part of the tail. Such current sheets are also formed in other regions of the magnetosphere between regions of oppositely aligned magnetic fields.



## 2.2 Single particle motion

In the previous section, the formal definitions of a plasma were presented, and a quick overview of plasma environments in the near Earth region was provided. This section will be a closer look at the behaviour and dynamics of the individual charged particles the plasma is constituted of. Describing the plasma through the behaviour of every individual constituent particle requires an enormous number of calculations, even for very small systems, since all the dynamic equations of each and every particle need to be calculated for every progression of the system. Also, this single particle approach, in which the feedback on the fields from the particle is not considered, is only valid in plasma where the magnetic fields generated by the motion of the charged particles is negligible compared to the external magnetic field they move in. For most geomagnetic plasma, this is not the case, and this approach is generally not feasible for any real systems. However, first having an understanding of the most basic motion of charged particles under the influence of external fields makes it easier to advance to more complex descriptions of realistic plasma systems later.

### Field lines

Before describing the behaviour of the plasma particles in the magnetic and electric fields it is convenient to introduce a way of visualizing what magnetic and electric fields are. The common way of visually representing a magnetic field is by drawing *field lines*, such as in the right panel of figure 2.3. The field lines are defined through the intensity of the field they represent. For a magnetic field, the field lines are defined as being everywhere tangential to the magnetic field along its length (*Gonzalez et al.*, 2016). It can be found by evaluating the unit tangent vector  $\mathbf{B}(\mathbf{x}_i)/|\mathbf{B}(\mathbf{x}_i)|$  at all locations  $\mathbf{x}_i$ , and integrating over the distance between each point,  $ds$  (see the left panel in figure 2.3). This gives the following relation for field line and the field

$$\mathbf{x}_{i+1} = \mathbf{x}_i + \mathbf{B}(\mathbf{x}_i)/|\mathbf{B}(\mathbf{x}_i)|ds \rightarrow \frac{dx_i}{ds} = \frac{B_i}{B} \quad (2.9)$$

The strength of a field is represented by the density of field lines in the same way as the density of contours on a topological map shows the steepness of the inclination. Since electromagnetic fields are directional they are vector fields. This requires the field lines to also have a defined direction which is often represented by arrows. The actual field lines do not exist in reality since the fields are continuous mediums. Still, they represent the real fields in the same way the contours on a topological map represents

the real inclination of the ground. The concept of field lines is closely related to how plasma particle dynamics are described, as for the majority of plasma environments the magnetic field and the plasma particles are connected and move together. In the rest of this chapter, the dynamics of the plasma particles and their interaction with the electromagnetic fields will be discussed.

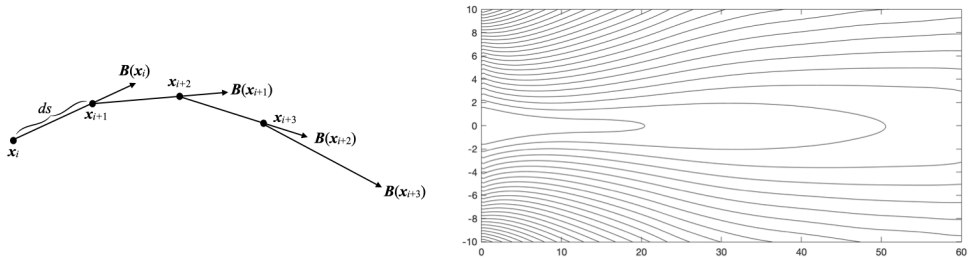


Figure 2.3: On the left is an illustration of the construction of a field line. The continuous field line is found by making  $ds$  infinitesimal. On the right is an example of how a plot of field lines can illustrate the topology of the magnetic field configuration.

### 2.2.1 Single particle motion in external fields

Any charged particle, with charge  $q$ , at rest is the source of an electrostatic field,  $\mathbf{E}$ . If a charged particle moves with a velocity,  $\mathbf{v}$ , it generates a current,  $\mathbf{j}$ , which is a source of a magnetic field,  $\mathbf{B}$ . Charged particles are the sources of the electromagnetic fields, and they are also influenced by them through the *Coloumb force*,  $\mathbf{F}_C = q\mathbf{E}$ , and the *Lorentz force*,  $\mathbf{F}_L = q\mathbf{v} \times \mathbf{B}$ . Using Newton's second law, we can derive the equation of motion for a single particle of mass  $m$  moving in an electromagnetic field

$$m \frac{d\mathbf{v}}{dt} = q(\mathbf{E} + \mathbf{v} \times \mathbf{B}) \quad (2.10)$$

Due to the cross product, the magnetic field can only accelerate the particle perpendicular to  $\mathbf{B}$ , while it can gain an acceleration parallel to the electric field by  $\mathbf{E}$ . This means that a charged particle under the influence of an electromagnetic field will gyrate around the magnetic field and drift along or perpendicular to the direction of the electric field depending on the field angles. The *gyrofrequency* or *cyclotron frequency* around the magnetic field line can be derived by assuming the electric field is zero and taking the second derivative of the equation of motion. The resulting expression is that of a harmonic oscillator with frequency given by the mass of the particle and the strength of the magnetic field

$$\omega_g = \frac{|q|B}{m} \quad (2.11)$$

The radius of rotation for a steady circular orbit is given by the ratio of the speed of the rotating object and the gyrofrequency, which gives us the *gyroradius* as a function of the velocity perpendicular to the magnetic field direction, the magnetic field strength, and the particle mass

$$r_g = \frac{v_{\perp}}{\omega_g} = \frac{mv_{\perp}}{|q|B} \quad (2.12)$$

The coupling between the charged particles and the electromagnetic fields are described through the well known *Maxwell's equations*

$$\nabla \cdot \mathbf{B} = 0 \quad (2.13)$$

$$\nabla \cdot \mathbf{E} = \frac{\rho}{\epsilon_0} \quad (2.14)$$

$$\nabla \times \mathbf{E} = -\frac{\partial \mathbf{B}}{\partial t} \quad (2.15)$$

$$\nabla \times \mathbf{B} = \mu_0 \mathbf{j} + \epsilon_0 \mu_0 \frac{\partial \mathbf{E}}{\partial t} \quad (2.16)$$

where  $\rho$  is the charge density,  $\mathbf{j}$  is the current density, and  $\epsilon_0$  and  $\mu_0$  is the permittivity and permeability of vacuum respectively. By solving equation 2.10 together with Maxwell's equations and the Newtonian equations of motion the dynamics of every single particle in a plasma could be calculated. However, a typical space plasma we would want to simulate has a particle density in the order of 1 – 10 particles per  $cm^3$  (e.g. *Toledo-Redondo et al., 2021*) which all interact with each other through Maxwell's equations, and a physical extent of at least several 1000  $km^3$ , making it an impossible number of calculations to solve. Additionally, the interesting quantities and properties of a plasma are all collective effects, making details on the level of single particle motions irrelevant for most purposes. Therefore, to make the calculations feasible a number of averaging schemes can be imposed on the plasma. The technique involving the least amount of averaging which gives the most accurate representation of the plasma and field interactions is a *Kinetic* description, which will be discussed in detail in the next section.

## 2.3 Kinetic plasma theory

In the previous section a short description of single particle motion was provided. In this section an alternative description will be derived which enables larger scale calculations through appropriate averaging schemes. The first step in this description is to define a new coordinate space called *phase space*.

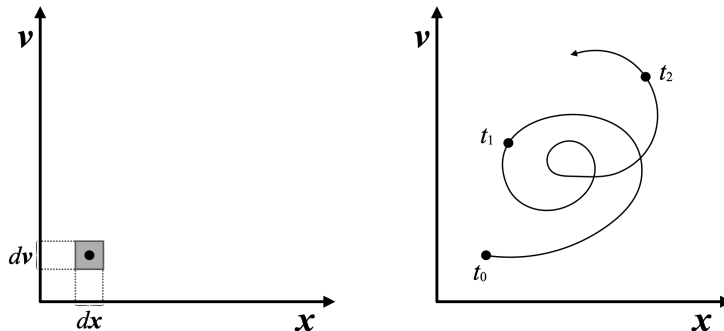


Figure 2.4: To the left is an illustration of phase space with a plasma particle contained in a phase-space volume-element defined by  $d\mathbf{x}$  and  $d\mathbf{v}$ . To the right, a possible phase-space trajectory for this particle is shown, starting from the initial state at  $t_0$ .

Phase space is an imagined space in which the complete state of a system can be described. In a Lagrangian description, one point in phase space represents one possible state a particle can be in, which is determined by its position and velocity at a given time. This means it is a six-dimensional space containing all possible spatial and velocity vectors a particle can have. This enables us to describe the full motion of a particle in three spatial dimensions and its velocity as a trajectory in phase space as time evolves. The phase-space trajectory of a system thus represents all the possible states the system can attain with the given initial conditions, while the full phase space represents all states that could be attained by any initial conditions. Figure 2.4 shows a particle contained in a phase-space volume-element defined by  $d\mathbf{x}$  and  $d\mathbf{v}$ , and how such a phase-space trajectory can look for the particle starting in some initial state at  $t_0$ . Representing a system in phase space can reveal information that was previously less obvious when analyzing it in normal spatial coordinates. For example, the phase-space trajectory of a pendulum swinging in two spatial dimensions will be a circle in phase space, clearly and concisely illustrating the periodicity of the system and the relationship between the velocity and the position of the pendulum through its full motion in one simple plot.

As mentioned earlier, a plasma is a system of many free particles interacting through the electromagnetic force. To describe the behaviour of a plasma it must therefore be

treated as a collective system, taking into account the interactions between the particles and the fields. A useful quantity to describe for a plasma in phase space is the exact microscopic phase space density

$$f_m(\mathbf{x}, \mathbf{v}, t) = \sum_{i=1}^N \delta(\mathbf{x} - \mathbf{x}_i(t)) \delta(\mathbf{v} - \mathbf{v}_i(t)) \quad (2.17)$$

It contains all possible positions and velocities that all the particles in a given plasma can attain. Here,  $N$  is the total number of particles in the plasma,  $\mathbf{x}$  and  $\mathbf{v}$  are Eulerian phase space coordinates, and  $\mathbf{x}_i(t)$  and  $\mathbf{v}_i(t)$  are the Lagrangian phase space coordinates describing the phase space trajectory of the  $i$ -th particle. The  $\delta$  is the *Dirac-Delta function*, which is zero everywhere except where its argument is zero, for which the function goes to infinity. This means that each particle in equation 2.17 will only give a contribution when its Eulerian and Lagrangian coordinates are the same, i.e. when the particle exists within the specific phase space volume element in question. Also, by integrating the product of the Dirac-Delta function and any other function over infinity, it returns the value of the function at the specific point where the argument of the Dirac-Delta function is zero, i.e.  $\int_{-\infty}^{\infty} f(x) \delta(x - a) dx = f(a)$ , which will be very useful later.

By taking the Lagrangian derivative of equation 2.17, the evolution of the plasma can be described. It is assumed that no particle is lost or added to the plasma, in which case this derivative equals zero. The resulting equation is called the *Klimontovich-Dupree equation* (Dupree, 1963), and contains information about the behaviour of all the particles in the plasma under the influence of the microscopic electromagnetic fields they produce

$$\frac{d}{dt} f_m(\mathbf{x}, \mathbf{v}, t) = \frac{\partial f_m}{\partial t} + \mathbf{v} \cdot \nabla_x f_m + \frac{q}{m} (\mathbf{E}_m + \mathbf{v} \times \mathbf{B}_m) \cdot \nabla_v f_m = 0 \quad (2.18)$$

Here, the  $\mathbf{E}_m$  and  $\mathbf{B}_m$  fields are the microscopic electromagnetic fields produced by the particles at the exact location of the  $i$ -th particle,  $\mathbf{x}_i$ , at some time  $t$ .

Since a plasma behaves as a collective system of particles it is useful to employ an averaging scheme to make the calculations easier and to extract the larger scale behaviour of the plasma. This involves integrating the exact phase space density over an appropriate volume of phase space,  $\Delta \mathbf{x} \Delta \mathbf{v}$ . This volume must be large compared to the average distance between the particles to make sure it contains a statistically significant number of particles, while at the same time be small compared to the size of the fluctuations in

the plasma so important processes are not missed. The distance between the particles is inversely proportional to the density, i.e. the lower limit of the integration volume must satisfy  $\Delta\mathbf{x} \gg n^{-1/3}$ . Small scale fluctuations in the fields and interactions between the plasma particles are shielded within the Debye sphere of the plasma. The upper limit of the integration volume is therefore the Debye sphere,  $\Delta\mathbf{x} < \lambda_D^3$ . The average phase space density is then the number of particles or states in phase space over the volume element defined by these limits

$$f(\mathbf{x}, \mathbf{v}, t) = \langle f_m(\mathbf{x}, \mathbf{v}, t) \rangle = \lim_{n^{-1/3} < \Delta\mathbf{x} \Delta\mathbf{v} < \lambda_D^3} \frac{\int_{\Delta\mathbf{x}} \int_{\Delta\mathbf{v}} f_m(\mathbf{x}, \mathbf{v}, t)}{\int_{\Delta\mathbf{x}} \int_{\Delta\mathbf{v}}} \quad (2.19)$$

The exact microscopic phase space density and the other properties of the plasma can now be written as the sum of this average distribution and the deviation from it. By definition, the average of the deviations from these average distributions must be equal to zero

$$\begin{aligned} f_m(\mathbf{x}, \mathbf{v}, t) &= f(\mathbf{x}, \mathbf{v}, t) + \delta f_m(\mathbf{x}, \mathbf{v}, t) & \langle \delta f_m(\mathbf{x}, \mathbf{v}, t) \rangle &= 0 \\ \mathbf{B}_m(\mathbf{x}, t) &= \mathbf{B}(\mathbf{x}, t) + \delta \mathbf{B}_m(\mathbf{x}, t) & \langle \delta \mathbf{B}_m(\mathbf{x}, t) \rangle &= 0 \\ \mathbf{E}_m(\mathbf{x}, t) &= \mathbf{E}(\mathbf{x}, t) + \delta \mathbf{E}_m(\mathbf{x}, t) & \langle \delta \mathbf{E}_m(\mathbf{x}, t) \rangle &= 0 \end{aligned} \quad (2.20)$$

Substituting equations 2.20 into the Klimontovich-Dupree equation (2.18) returns the *Vlasov equation*, which is a kinetic equation describing the average phase space distribution of the plasma under the influence of the average electromagnetic fields

$$\frac{\partial f}{\partial t} + \mathbf{v} \cdot \nabla_x f + \frac{q}{m} (\mathbf{E} + \mathbf{v} \times \mathbf{B}) \cdot \nabla_v f = 0 \quad (2.21)$$

The Vlasov equation is a valid description in collisionless plasmas. Most space plasma are collisionless (*Baumjohann and Treumann, 2012*), but in the case of collisional plasma, the appropriate distribution is the Maxwell equation, which sets the right hand side of the Vlasov equation equal to some collision term,  $(\partial f / \partial t)_c$ . By integrating, macroscopic quantities of the plasma can be derived from the phase space distribution. The distribution function describes the probability of finding a particle within a certain phase space volume element, and it is analogous to counting the number of points in phase space at a given time. Since the position and velocity of the particle are independent variables in phase space, the dependence on one of the variables can be eliminated from the dis-

tribution through integration. By integrating over the full velocity space, the spatial distribution of the plasma can be obtained, which multiplied with the particle charge gives the charge distribution of the plasma

$$\rho(\mathbf{x}, t) = \sum_s q_s \int f_s(\mathbf{x}, \mathbf{v}, t) d\mathbf{v} \quad (2.22)$$

The subscript  $s$  indicates the different particle species of the plasma. Multiplying equation 2.22 with the particle velocities returns the current density in the plasma

$$\mathbf{j}(\mathbf{x}, t) = \sum_s q_s \int \mathbf{v}_s f_s(\mathbf{x}, \mathbf{v}, t) d\mathbf{v} \quad (2.23)$$

The Vlasov equation, together with Maxwell's equations, and the charge and current densities constitutes a full kinetic description of a collisionless plasma. With these, the full behaviour of the collisionless plasma can be described at all times, with no loss of information for scales larger than the Debye length. However, since it is a system of self-consistent, non-linear equations it is very difficult to solve. For large scale plasma systems where the microscopic interactions are not governing the dynamics it is therefore more convenient to use further averaging schemes to make the description easier. A brief discussion about this is provided in the next section.

## 2.4 Fluid plasma description

A first step towards gaining useful information about a plasma from the distribution functions is to take the velocity moments of them. This extracts macroscopic quantities of the plasma from the distributions. The method of taking the moments of a distribution involves integrating the product of the distribution and the velocity to some order over the full phase space

$$M_i(\mathbf{x}, t) = \int \mathbf{v}^i f(\mathbf{x}, \mathbf{v}, t) d\mathbf{v} \quad (2.24)$$

The factor  $i$  gives the order of the moment, and can have any value from zero to infinity. By doing this, the velocity dependence is removed, and properties depending on the spatial and temporal coordinates are returned. Taking the moments of the distribution function returns macroscopic properties of the plasma which describe the large scale

evolution of the plasma system as a whole. It is an approach that treats the plasma more like a fluid than a set of individual particles. By doing this, some microscopic details of the behaviour of the particles is lost, since it returns average properties. However, in many cases this is more than enough information to gain an understanding of the evolution of the plasma system, particularly when it is subject to slow temporal evolution and large spatial scales. The zeroth order moment is just the spatial distribution of states in the plasma, i.e. the density of species  $s$  in the plasma,  $n_s$ , which multiplied with the charge is what creates the charge density in equation 2.22.

$$n_s(\mathbf{x}, t) = \int f_s(\mathbf{x}, \mathbf{v}, t) d\mathbf{v} \quad (2.25)$$

The first order moment gives the average velocity or bulk flow of the species.

$$\mathbf{v}_{sb} = \frac{1}{n_s} \int \mathbf{v}_s f_s(\mathbf{x}, \mathbf{v}, t) d\mathbf{v} \quad (2.26)$$

The plasma pressure is defined through the deviations from this average flow, and can be found using the second moment of the distribution, letting the difference from the bulk flow be the velocity ( $\mathbf{w}_s = \mathbf{v}_s - \mathbf{v}_{sb}$ )

$$\mathbf{P}_s = m_s \int \mathbf{w}_s \mathbf{w}_s f_s(\mathbf{x}, \mathbf{v}, t) d\mathbf{v} \quad (2.27)$$

In a similar manner, higher and higher order moments can be used to derive further properties of the plasma from the distribution functions. While these can be useful and necessary in a variety of systems and applications we do not discuss them further in this thesis since in our calculations we have truncated the system of equations at the pressure tensor, as will be discussed later.

To extract information about the larger scale evolution of the plasma, the method of moments can be applied to the Vlasov equation (2.21)

$$\int \mathbf{v}^i \left( \frac{\partial f}{\partial t} + \mathbf{v} \cdot \nabla_x f + \frac{q}{m} (\mathbf{E} + \mathbf{v} \times \mathbf{B}) \cdot \nabla_v f \right) d\mathbf{v} = 0 \quad (2.28)$$

The zeroth order moment of the Vlasov equation returns the *continuity equation*, which shows that in the absence of processes creating or annihilating particles, the total number density of the plasma is conserved. Since time and velocity are independent variables in phase space, the integral and the time derivative can be exchanged in the first term



on the left side of equation 2.28. Using equation 2.25, the first term in equation 2.28 returns the Eulerian part of the derivative of the density. The same argument about the independence of the phase space variables can be applied to the second term of equation 2.28 to exchange the integral and the spatial derivative. Using equation 2.26, the second term then returns the Lagrangian part of the derivative. By rewriting the third term in equation 2.28 using the total differential and utilizing some vector algebraic relations, it can be shown that it does not contribute. The continuity equation then becomes

$$\frac{\partial n_s}{\partial t} + \nabla \cdot (n_s \mathbf{v}_{sb}) = 0 \quad (2.29)$$

The continuity equation is conservative, telling us that in a collisionless plasma which follows the Vlasov equation, the number of particles in the plasma is unchanged. Using similar methods, the first order moment of the Vlasov equation returns the *momentum density equation*, which describes the evolution of the bulk momentum of the plasma.

$$\frac{\partial(n_s \mathbf{v}_{sb})}{\partial t} + \nabla \cdot (n_s \mathbf{v}_{sb} \mathbf{v}_{sb}) + \frac{1}{m_s} \nabla \cdot \mathbf{P}_s - \frac{q_s n_s}{m_s} (\mathbf{E} + \mathbf{v}_{sb} \times \mathbf{B}) = 0 \quad (2.30)$$

Both the continuity equation and the momentum density equation must hold for all the particle species of the plasma individually. In this sense, they form the basis of a multi-fluid treatment of the plasma. Each of the particle species in the plasma are treated as their own fluid, which interact with each other, but are also free to move relative to each other.

For each moment taken of the Vlasov equation a conservation equation can be derived. The second moment of the Vlasov equation defines the energy density conservation equation, which describes the heat transfer in a plasma, and is the evolution of the pressure tensor in the momentum density conservation equation (2.30). Similarly, equation 2.30 is also the evolution equation of the bulk flow in the continuity equation (2.29). This pattern of always needing the next higher moment to describe the evolution of the current variables makes it necessary to truncate the system of equations at some level in order to solve them and describe the plasma behaviour. A common way to do this, is to define some *equation of state* which defines the heat transfer as negligible such that 2.30 is the highest order moment necessary. This is also the level at which we have truncated the system of equations in our research. What equation of state is most appropriate depends on the plasma system in question, but typical choices in collisionless space plasma systems are the ideal gas equation, both isotropic ( $\mathbf{P} = p\mathbf{I}$ ,  $p = nkT$ ) or non-isotropic ( $\mathbf{P} = p_{\perp}\mathbf{I} + (p_{\parallel} - p_{\perp})\mathbf{e}_{\parallel}\mathbf{e}_{\parallel}$ ,  $p_i = nkT_i$ ,  $i = \parallel, \perp$ ), or some form of adiabatic equation that eliminates the heat transfer. With such an equation for the pressure, equations 2.25, 2.26,

2.29 and 2.30 together with Vlasov's and Maxwell's equations form a closed set of equations that describe the the plasma behaviour approximated as multiple individual, but interacting fluids.

### Magnetohydrodynamics

Building on the fluid treatment of the plasma system just described, an even simpler description of the plasma can be derived through yet another averaging scheme. This involves assuming the plasma behaves as a single conducting fluid which carries electromagnetic fields and currents, and where no distinction is made between the particle species constituting the plasma. For each particle species in the plasma, the closed system of equations in the multi-fluid description must hold. Since the plasma is neutral as seen from the outside, the concept of quasineutrality requires that the number of positive and negative charge carriers in the plasma is equal. By choosing the appropriate forms of the density, mass and velocity of the total particles in the plasma, these can be inserted into the multi-fluid description to derive the single-fluid description called *Magnetohydrodynamics*, or MHD. For a plasma consisting of one ion species and electrons, the density, mass and velocity of the single-fluid then takes the form

$$n = \frac{m_e n_e + m_i n_i}{m_e + m_i} \quad (2.31)$$

$$m = m_e + m_i = m_i \left( 1 + \frac{m_e}{m_i} \right) \quad (2.32)$$

$$\mathbf{v} = \frac{m_e n_e \mathbf{v}_e + m_i n_i \mathbf{v}_i}{m_e n_e + m_i n_i} \quad (2.33)$$

Adding the continuity equation (2.29) and the momentum equation (2.30) for each species and rewriting them in terms of these total fluid variables returns the MHD continuity equation,

$$\frac{\partial n}{\partial t} + \nabla \cdot (n\mathbf{v}) = 0 \quad (2.34)$$

and the MHD equation of motion

$$\frac{\partial(mn\mathbf{v})}{\partial t} + \nabla \cdot (mn\mathbf{v}\mathbf{v}) = -\nabla \cdot \mathbf{P} + \mathbf{j} \times \mathbf{B} \quad (2.35)$$

To close the set of equations for MHD, an evolutionary equation for the current density,  $\mathbf{j}$  is needed. Since the current density is defined by the difference in the velocity of negative and positive charge carriers, this can be derived by subtracting the two-fluid momentum equations for ions and electrons. For generality, a term describing the collisions between electrons and ions ( $\mathbf{R}/m_s$ ) can be added to the two-fluid equations before they are subtracted from each other. The result is the *Generalized Ohm's law*, which is most often expressed as an equation for the electric field

$$\mathbf{E} + \mathbf{v} \times \mathbf{B} = \frac{1}{ne} (\mathbf{j} \times \mathbf{B} - \nabla \cdot \mathbf{P}) + \frac{m_e}{ne^2} \left( \frac{\partial \mathbf{j}}{\partial t} + \nabla \cdot \left( \mathbf{v}\mathbf{j} + \mathbf{j}\mathbf{v} - \frac{\mathbf{j}\mathbf{j}}{ne} \right) \right) + \eta \mathbf{j} \quad (2.36)$$

In an ideal plasma, all the terms on the right side of equation 2.36 is equal to zero, and the plasma and magnetic field are *frozen in*, meaning they move together. The first parenthesis on the right hand side of equation 2.36 is the *Hall* term and the contribution from the pressure divergence, the second parenthesis can be described as the electron inertia, and the last term is a resistive term that came from the collision term added to the two-fluid equations ( $\eta$  is the plasma resistivity). Often, the inertia of the electrons is neglected since the electron mass is so small that the electrons are free to move immediately in response to any electric fields that might arise from charge separation in the plasma. The generalized Ohm's law is therefore a way to determine the electric field through the plasma dynamics in the MHD approximation. A way to interpret it physically is that the electric field assumes the value it must have in order to prevent charge separation between ions and electrons which would break the quasi-neutrality constraint in a large scale plasma (*Vasyliūnas*, 2011). The MHD approximation is valid in many space plasma systems, and describes excellently the collective behaviour of processes that occur on large spatial and long temporal scales. For MHD to be valid, it is necessary that the variations in both the electromagnetic fields and the plasma fluid are on larger scales than the characteristic scales of the heaviest species in the plasma. This means the length scale of the variations must be larger than the ion gyroradius,  $L > r_i$ , and the frequency of the variations must be lower than the ion gyrofrequency,  $\omega < \omega_i$ .

In this chapter the most basic plasma properties have been discussed. First, the defining characteristics of a plasma as a fourth state of matter were presented, followed by a brief discussion about how different plasma systems in our near space environment can look as well as where to find them. We then looked at the detailed motion of single plasma particles in electromagnetic fields, whose dynamics are coupled through Maxwell's equations. Since a plasma environment is a large scale system, this single particle description was extended to contain distribution functions, which provides information about the probability of each particle being in a specific state determined by its position and velocity. This was further simplified by averaging away all fluctuations on scales smaller than the Debye length, and the Vlasov equation was derived. The Vlasov equation, together with Maxwell's equations, and the charge and current density derived from the Vlasov distribution, which couple the distribution function to the Maxwell's equations for the fields, constitute a full kinetic description of the coupled system of plasma and electromagnetic fields. The multi-fluid moments of this provides fluid variables for the constituent species of the plasma, which is a good approximation for most plasma processes. For large spatial and temporal scales this can be further simplified to the single-fluid MHD description which captures the large scale fluid behaviour of a plasma system. In the next chapter we will look at magnetic reconnection, which is a complex interaction between magnetic fields and plasma responsible for some of the largest energy conversion processes in the universe.



# Chapter 3

## Magnetic reconnection

Magnetic reconnection is an energy release process where stored magnetic energy is converted into kinetic and thermal plasma energy. This energy conversion is caused by a macroscopic change in the magnetic field topology. The process of magnetic reconnection was first proposed by *Giovanelli* (1947) to explain the transport of magnetic flux associated with sunspots. Here the presence of a magnetic neutral point was suggested as a necessary condition for the fast transport of plasma and magnetic flux observed in association with solar flares around sunspots. Although the existence of the Earth's magnetic field and the Solar Wind was already known, the idea of magnetic reconnection occurring between the IMF and the magnetic field of our Magnetosphere was not suggested until 14 years later by *Dungey* (*Dungey*, 1961). He argued that magnetic reconnection in the dayside and nightside of the magnetosphere would explain the observed convection patterns over the polar cap, as well as allow for the necessary influx of particles to generate the aurora. Today, magnetic reconnection is known to occur in many plasma environments in space, the Sun and the magnetosphere, as well as in plasma laboratories and fusion reactors on Earth (*Yamada et al.*, 2010). It has also been proposed to occur in high energy astrophysical environments much further away from the Earth, such as in magnetars (*Lyutikov*, 2003) and black hole accretion discs (*Comisso and Asenjo*, 2021; *Ripperda et al.*, 2022). Since the magnetic field is closely coupled to the dynamics of the plasma particles, how magnetic reconnection evolves is highly dependent on the conditions of the field and plasma environment in which it occurs. The most basic elements of magnetic reconnection in our magnetosphere are still explained in the same way as it was in *Dungey's* first suggestion, but the knowledge about the details of its initiation, interaction, evolution and cessation have been vastly improved since then (*Fuselier and Lewis*, 2011). Today it is well known that magnetic reconnection is an example of a highly multi-scale process, both on spatial and temporal scales. This is true for each reconnecting system individually, as well as comparatively between different types of

reconnecting systems. For example, in the magnetosphere of the Earth, the full reconnecting system can be on spatial scales in the order of  $10^5$  km, while the region where the actual reconnection and magnetic topology change occurs is on scales in the order of 10 – 100 km. The same regions will be on vastly different scales in other reconnecting systems, such as in the solar corona or in fusion reactors. Significant multi-scale differences in configuration, evolution, and efficiency of the reconnection process have been shown to depend on both the initial symmetry, shear and magnitudes of the magnetic field (e.g. *Pritchett and Coroniti, 2004; Spinnangr et al., 2021a; Swisdak et al., 2003*), and the temperature, composition, distribution, and dynamics of the plasma (e.g. *Dargent et al., 2017, 2019; Kolstø et al., 2020a,b; Spinnangr et al., 2021b; Tenfjord et al., 2018, 2019, 2020; Toledo-Redondo et al., 2021*). While magnetic reconnection has been an active field of study for more than 60 years, it has seen a significant jump in the recent decades due to the almost explosive increase in available computational power and the recent launch of satellite missions well suited, and explicitly designed, for observing magnetic reconnection in our magnetosphere.

In this chapter, magnetic reconnection will be discussed in detail, starting with the introduction of some fundamental concepts common for all varieties of magnetic reconnection. Then some simpler models of reconnection significant for the historical development of the modern descriptions will be presented, before the current kinetic, multi-scale descriptions will be discussed.

### General overview of magnetic merging and topology change

Depending on the initial conditions of the reconnecting system and which plasma scheme is used to describe it, the dynamics, drivers and various physical processes which we can describe with theory will be different. However, the most basic elements of magnetic reconnection are common across the different schemes. These are illustrated schematically in figure 3.1. The top row illustrates the 2D topology change of the magnetic field during reconnection. Two regions of initially oppositely-aligned magnetic fields start to move towards each other due to some driving force which produces an inflow, illustrated by the blue arrows. When the field lines meet in the middle, magnetic reconnection takes place, and new magnetic connectivity is created. These new magnetic field lines are then pushed out, creating an outflow as illustrated by the pink arrows. The regions of different magnetic topology are separated by a separatrix, which is a collective term for the field lines that meet exactly at the x-point where the magnetic field is zero and reconnection takes place.

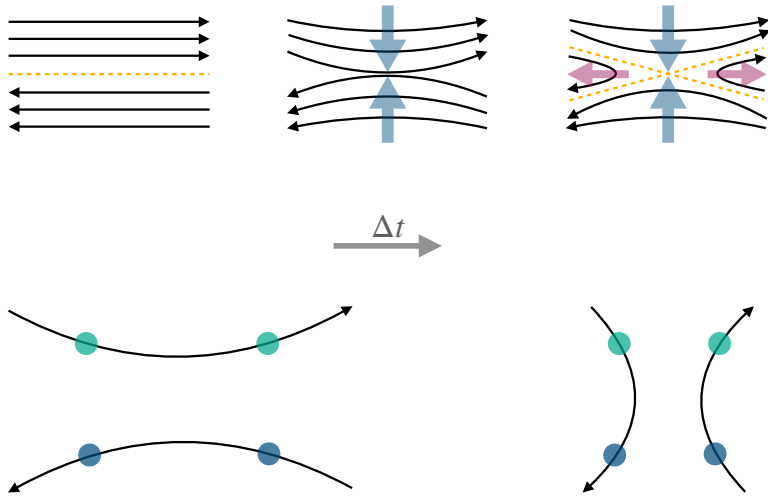


Figure 3.1: A schematic illustration of the most basic elements of magnetic reconnection. The black arrows illustrate the magnetic field in all sketches. The blue and pink arrows in the top row are the plasma inflow and outflow respectively. The regions of different magnetic topology are separated by a separatrix, illustrated by the yellow dotted lines in the rightmost sketch in the top row. The point where the separatrices meet in the middle is the x-point. The bottom row illustrates how magnetic reconnection breaks the connectivity of plasma elements that originally existed on the same field line.

The bottom row of figure 3.1 illustrates the breaking of connectivity between plasma elements that occur during magnetic reconnection. The plasma elements, illustrated by blue and turquoise dots, are initially connected to a specific field line. After reconnection has taken place, the plasma elements that were originally connected to the same field line have now lost this connectivity, and new connectivity has been created between plasma elements from different field lines. This change in connectivity between different plasma elements is the essence of magnetic reconnection, and is what separates it from normal magnetic field annihilation between magnetic fields in a neutral medium which for example occurs between two normal bar magnets that are pushed close together. In this way, magnetic reconnection allows, for example, plasma that originates from the solar wind to enter into the magnetosphere of the Earth.

### Magnetic diffusion

A plasma particle in a constant, external magnetic field will perform a gyration motion around a field line due to the influence by the Lorentz force,  $\mathbf{F}_B = (q/m)\mathbf{v} \times \mathbf{B}$ , which is perpendicular to the magnetic field direction. If an electric field exists, the *guiding center* of the particle, i.e. the center of the particle gyromotion, will also move in a



direction dependent on the angle between the magnetic and electric field. The plasma and magnetic field are said to be *frozen in* when they move together and the plasma particles continue to gyrate around the same magnetic field line, which occurs in an *ideal plasma*. In an ideal plasma, Ohm's law reduces to the ideal Ohm's law,  $\mathbf{E} = -\mathbf{v} \times \mathbf{B}$ . If the external magnetic and electric field are not parallel, this will lead to a general drift of the particle in the direction perpendicular to both the magnetic and electric field, called the  $E \times B$  drift,  $\mathbf{v}_{E \times B} = (\mathbf{E} \times \mathbf{B})/B^2$ . If the plasma is ideal, the magnetic field will also move with this drift. Other drifts can occur when the fields vary, such as the electric polarization drift, the magnetic gradient and curvature drifts, or when other sources of force on the particles is present, such as the gravitational drift or the diamagnetic drift. In general, a drift caused by some force acting on the plasma can be found through the *general force drift equation*

$$\mathbf{v}_D = \frac{1}{\omega_g} \left( \frac{\mathbf{F}}{m} \times \frac{\mathbf{B}}{B} \right) \quad (3.1)$$

When the plasma and magnetic field move, the magnetic field can experience a change. This change can be described by combining Ampère's law (2.16 neglecting the displacement current), Faraday's law (2.15) and Ohm's law (2.36 neglecting all other terms than the  $\mathbf{v} \times \mathbf{B}$ -drift and the resistive term).

$$\frac{\partial \mathbf{B}}{\partial t} = \nabla \times \mathbf{v} \times \mathbf{B} + \frac{\eta}{\mu_0} \nabla^2 \mathbf{B} \quad (3.2)$$

The first term on the right hand side of equation 3.2 describes the convection of the magnetic field with the moving plasma. As long as the plasma is frozen in, this is the only contributing term to the variations in  $\mathbf{B}$ . If the variations in the electromagnetic fields are on large spatial scales and slow the plasma can be assumed to be frozen in. However, spatial variations on the scale of the gyroradius or temporal variations on the scale of the gyroperiod of the plasma particles can cause the plasma to lose its frozen-in behaviour, and the particles and magnetic field can start to move across each other (Vasyliunas, 1975). When this happens, it is possible for magnetic diffusion to occur, which is described by the second term on the right hand side of equation 3.2. For magnetic reconnection to occur it is necessary that the frozen-in behaviour of the plasma breaks down to allow magnetic diffusion. Most of the plasma in regions where reconnection takes place is frozen in. It is only in a comparatively small region in the reconnecting system where the frozen-in behaviour is violated and magnetic diffusion can take place. This is the *diffusion region*, which is located at the intersection between regions of oppositely aligned magnetic fields. Within the diffusion region some or all

of the non-ideal terms in Ohm's law become large enough that they can no longer be neglected from the calculations since their influence on the particle dynamics is too significant.

### The reconnection rate

The rate at which magnetic flux is converted during magnetic reconnection is called the *reconnection rate*. It describes how efficiently magnetic flux,  $\Phi_{rec}$ , is transported into and out of the reconnection site and can be expressed through the *reconnection electric field* by using Faraday's law (equation 2.15)

$$\frac{\partial}{\partial t} \Phi_{rec} = \frac{\partial}{\partial t} \iint_A \mathbf{B} \cdot d\mathbf{A} = - \iint_A \nabla \times \mathbf{E} \cdot d\mathbf{A} = - \oint_C \mathbf{E} \cdot d\mathbf{l} \quad (3.3)$$

where  $A$  is an area bounded by the curve  $C$  intersecting the reconnection site as illustrated in figure 3.2. The teal area in the center represents the diffusion region and the black curved lines are the magnetic field lines. The reconnection site is usually referred to as the *x-point* or the *x-line* and is situated at the center of this diffusion region.

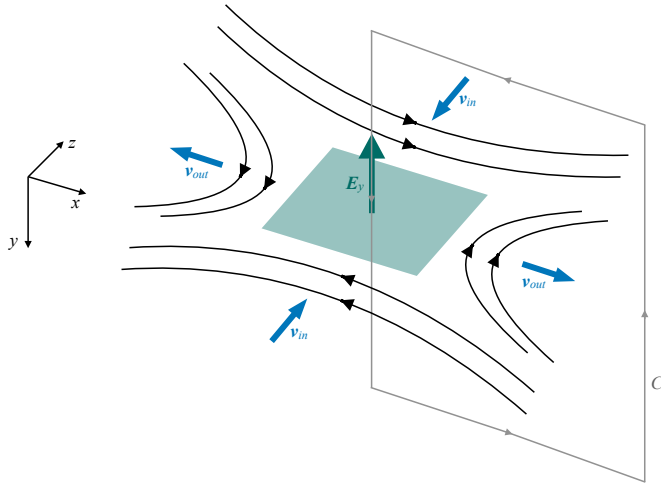


Figure 3.2: A schematic diagram illustrating how the reconnection rate is calculated.

The inflow and outflow direction are illustrated with the blue velocity vectors, and the dark teal vector shows the direction of the reconnection electric field in this setup. The direction for the line integral in the last expression of equation 3.3 is given by the arrows on  $C$ . This figure also shows the spatial orientation employed in the rest of this thesis and the included published work. The inflow direction is defined along  $z$ , the outflow

direction along  $x$ , and the initial current direction in the current sheet between the regions of opposite magnetic field is oriented along  $y$ . In this configuration, the reconnection electric field points along the  $y$ -direction, and the reconnection rate reduces to  $\partial\Phi_{rec}/\partial t = \int E_y dy$ . Assuming the reconnection electric field is equal to zero far away from the  $x$ -point further simplifies this expression, and the reconnection rate simply becomes the value of the reconnection electric field at the  $x$ -point. In any other reconnecting geometry, the reconnection rate can always be identified as the reconnection electric field along the  $x$ -line (Vasyliunas, 1975). As will be discussed later, many models of reconnection have their own expressions for the reconnection rate that fits within the parameter scheme of each model, but they all describe the same process of flux transport and magnetic topology change.

### 3.1 Early reconnection models

One of the first models of magnetic reconnection had its beginning during a lecture held by Sweet in 1956 about how the formation of magnetic neutral points could explain some observed features of solar flares, which was not published until two years later (Sweet, 1958). The ideas of Sweet were expanded upon and quantized by Parker in the meantime (Parker, 1957), and the *Sweet-Parker* model was created. This model treats the plasma as an MHD fluid, and is based on the assumption of conservation of mass, momentum, energy, and magnetic flux through an extended diffusion region (Treumann and Baumjohann, 1997). The length of the diffusion region along the outflow direction,  $L$ , is assumed to be the same as the full length of the reconnecting system,  $\Lambda$ , while the thickness along the inflow direction,  $d$ , is assumed to be much smaller, i.e. the diffusion region is a thin, elongated area between two regions of symmetric but oppositely aligned magnetic fields as illustrated by the orange region in figure 3.3.

In the Sweet-Parker model, the inflow magnetic field,  $B_i$ , is transported with the plasma flow,  $v_i$ , into the diffusion region where magnetic reconnection takes place and magnetic energy is converted to heat and kinetic energy of the plasma fluid. The less energetic, newly reconnected field,  $B_o$ , is transported away with the accelerated and heated outflowing plasma flow,  $v_o$ . By considering the force balance between the inflow and outflow region, the outflow velocity can be estimated. In the inflow region, the transport is governed by both plasma and magnetic variables. Since the Sweet-Parker model is a steady state model the temporal derivative can be neglected, and through Ampère's law (equation 2.16) the MHD momentum equation reduces to

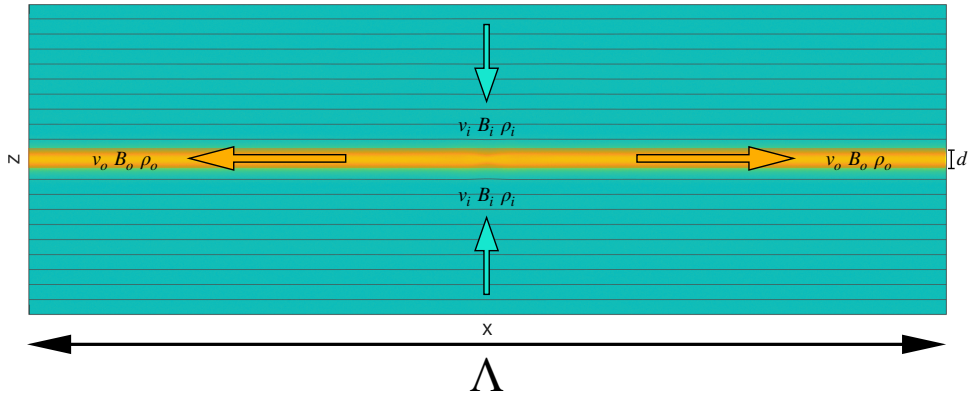


Figure 3.3: An illustration of a reconnecting system as described in the Sweet-Parker model. The orange region is the diffusion region, while the black lines are the contours of the magnetic field. The arrows indicate the direction of the flux transport.

$$\rho_i(\mathbf{v}_i \cdot \nabla)\mathbf{v}_i = -\nabla p_i + \mathbf{j}_i \times \mathbf{B}_i = -\nabla \left( p_i + \frac{B_i^2}{2\mu_0} \right) + \frac{1}{\mu_0} \mathbf{B}_i \cdot \nabla \mathbf{B}_i \quad (3.4)$$

The first term on the right-hand side represents the gradient of the sum of the isotropic plasma pressure and the magnetic pressure in the system, while the second term represents the magnetic tension which results from the bending of the field lines towards the  $x$ -point. In the inflow region above and below the diffusion region the magnetic pressure tends to push the plasma towards the  $x$ -point while the plasma pressure gradient and the magnetic tension tends to work against this in an effort to make the field lines straight again. By symmetry arguments we can neglect all derivatives in the  $x$ -direction, and we assume that the inflow velocities are small. The expression then reduces to

$$0 \approx \frac{\partial}{\partial z} \left( p_i + \frac{B_i^2}{2\mu_0} \right) \quad (3.5)$$

Inside the diffusion region, the magnetic pressure vanishes, and only the thermal pressure remains. By virtue of pressure balance, the pressure in the diffusion region,  $p_d$ , must equal the pressure in the inflow region. In the outflow region, the magnetic field is assumed to be weak, while the particle velocities are high. The momentum equation then reduces to

$$\rho_o(\mathbf{v}_o \cdot \nabla)\mathbf{v}_o = -\nabla p_o + \mathbf{j}_o \times \mathbf{B}_o \approx -\nabla p_o \quad (3.6)$$

In the outflow region, only the  $x$ -derivatives are assumed to contribute, and the expres-

sion further simplifies to

$$\frac{\partial}{\partial x} \left( \frac{\rho_o v_o^2}{2} + p_o \right) \approx 0 \quad (3.7)$$

Again due to pressure balance, the pressure in the outflow region must be equal to the pressure in the diffusion region. Also, since the model is based on the assumption of mass conservation and incompressibility, mass densities in the different regions must be the same. By assuming the plasma pressure remains constant, the outflow velocity can with this be expressed through the inflow variables

$$p_i + \frac{B_i^2}{2\mu_0} = p_d = \frac{\rho_o v_o^2}{2} + p_o \rightarrow v_o = \frac{B_i}{\sqrt{\mu_0 \rho}} = v_{Ai} \quad (3.8)$$

The final expression in this equation is the *Alfvén velocity*. It is the group velocity of an electromagnetic-hydrodynamic wave produced in a plasma (*Alfvén*, 1942). The group velocity of a wave is the velocity with which information travels, and the Alfvén velocity in a plasma is thus synonymous to the sound velocity in neutral matter. Equation 3.8 also shows that in the Sweet-Parker model, all the magnetic energy coming in from the inflow is converted to plasma energy in the outflow.

The Sweet-Parker reconnection rate can be derived by Ohm's law and continuity arguments. Starting from the simplest form of the non-ideal Ohm's law,  $\mathbf{E} = -\mathbf{v} \times \mathbf{B} + \eta \mathbf{j}$ , the expression for the reconnection electric field at the x-point can be related to inflow and outflow variables by recognizing that the field is the same inside and at the boundary of the diffusion region. In the inflow, the plasma is frozen in, and  $\mathbf{E} = -\mathbf{v}_i \times \mathbf{B}_i$ , while in the diffusion region it is described by the current,  $\mathbf{E} = \eta \mathbf{j}$ . Since the MHD fluid is incompressible and the mass, energy, and momentum are conserved throughout the reconnection process, the speed at which magnetic flux can be processed is limited by the speed at which the plasma can be ejected from the reconnection site, i.e. by the inflow Alfvén speed given by equation 3.8. This means that the plasma in the diffusion region is divergence free, and the amount of mass flux entering the diffusion region must equal the amount of flux being ejected, i.e.  $v_i L = -v_o d$ . Using Ampère's law to write the current in terms of the magnetic field, the reconnection electric field becomes

$$E = -v_i B_i = \eta j = \eta \frac{B_i}{\mu_0 d} = v_o B_o \quad (3.9)$$

This can be rewritten as an expression for the inflow velocity

$$v_i = -\eta \frac{1}{\mu_0 d} = \frac{\eta}{\mu_0} \frac{v_o}{v_i L} = \frac{\eta}{\mu_0} \frac{v_{Ai}}{v_i L} \quad (3.10)$$

This can finally be rewritten as an expression for the ratio between the inflow and outflow velocities, which is the same as the reconnection rate, with the assumptions upon which the Sweet-Parker model is founded

$$\frac{v_i}{v_{Ai}} = \sqrt{\frac{\eta}{\mu_0 L v_{Ai}}} = \frac{1}{\sqrt{S}} \quad (3.11)$$

Here the *Lundquist number*,  $S$ , is introduced, which is the magnetic *Reynolds number* for the Alfvén velocity, describing the ratio between the time-scales of convection and diffusion for the plasma (*Baumjohann and Treumann, 2012*).

The Sweet-Parker model is a simple description of magnetic reconnection based on the MHD equations for a plasma which describes the large-scale behaviour of a reconnecting system well. It was therefore very well received at the time, and the hope was that it would describe the observed parameters associated with solar flares. Unfortunately, the Lundquist number is very large in real space plasma systems, and the Sweet-Parker reconnection rate is several orders of magnitude too small compared to the observed rates (*Baumjohann and Treumann, 2012*). A notable attempt to improve the Sweet-Parker model to predict faster rates was made by Petschek (*Petschek, 1964*), who suggested that neglecting the magnetic field in the outflow was the source of the problem with the model. In the *Petschek model*, the length of the diffusion region is significantly reduced. Outside the diffusion region in the outflow, the outflow magnetic field is finite and is separated topologically from the inflow magnetic field by stationary slow shocks, as illustrated in figure 3.4. By allowing convection of the magnetic field in the outflow region outside of the shorter diffusion region, the Petschek model successfully reproduces a fast enough reconnection rate to explain the observed energies in solar flares. However, the solution is unstable and has never been successfully reproduced in simulations with constant resistivity or observed in nature, although solutions with a localized resistivity have been reproduced in simulations (*Baumjohann and Treumann, 2012; Kulsrud, 2001; Vasyliunas, 1975*).

Both the Sweet-Parker model and the Petschek model assumes the reconnecting system can be described as an MHD fluid. Other attempts at modeling reconnection have started from a single particle description, where the dynamics of every plasma particle is calculated explicitly, such as the model developed by Dessler, Alfvén and Cowley

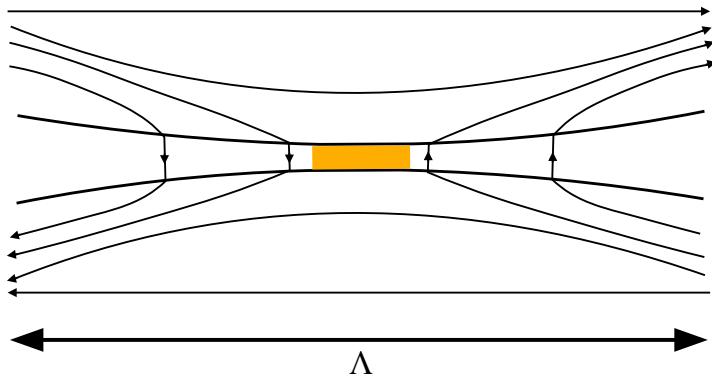


Figure 3.4: A sketch of the magnetic topology during reconnection as described in the Petschek model. The orange area in the center represents the diffusion region, and the thicker black lines are the stationary shock fronts.

(*Dessler*, 1968, 1971; *Vasyliunas*, 1975). However, this model can be treated as a special case of the Petschek model for reconnection taking place in a collisionless plasma in the extremely-low-density limit (*Vasyliunas*, 1975). Models based on modified versions of MHD theory that allow for more complex physical processes have also been used to describe magnetic reconnection. For example *Hall-MHD*, where the electron and ion fluids are allowed to separate causing the generation of *Hall electric fields* in the distance between the electron and ion demagnetization scales away from the x-point, is a better approximation than the one-fluid MHD description. Still, the fluid approximations are unable to reproduce the micro-scale processes of reconnection inside and close to the diffusion region, and are best treated as a global or large scale approximation to describe the most general features of magnetic reconnection. In the rest of this chapter, the description of magnetic reconnection treating the plasma as a kinetic system will be presented. Allowing the various particle species of the plasma to have different dynamics based on their different intrinsic scale lengths introduces new physics to the reconnection region which can more accurately reproduce the dynamics of real plasma systems.

## 3.2 Kinetic and multi-fluid model of reconnection

In the previous section several models of magnetic reconnection based on one-fluid MHD theory was discussed. Although they depict the large scale features of reconnection such as the general magnetic topology change and plasma flow, they are unable to accurately predict the reconnection rate and energy conversion, or to reproduce any of the particle dynamics taking place on scales smaller and faster than the ion inertial length and gyrofrequency. Indeed, in collisionless plasma systems where the resistivity is negligible

they are even unable to explain how reconnection would occur in the first place. To describe magnetic reconnection accurately it is therefore necessary to include the small and fast scale dynamics of the plasma, and treat the reconnecting system as a kinetic plasma with self-consistently generated magnetic and electric fields.

The kinetic plasma description treats the plasma as a set of individual particles that behave collectively, each generating their own electromagnetic fields and each being affected by the collective fields of the other particles. It is therefore distinct from the single-particle description, where particles move in prescribed external fields, by this collective and self-consistent interaction. It builds on the kinetic description of plasma behaviour as described in chapter 2, which we will repeat some of here. The corner stone of the description is the interaction between the plasma particles and the self-consistently generated electromagnetic fields, which is described through Maxwell's equations

$$\nabla \cdot \mathbf{E} = \frac{\rho_s}{\epsilon_0} \quad (3.12)$$

$$\nabla \cdot \mathbf{B} = 0 \quad (3.13)$$

$$\nabla \times \mathbf{E} = -\frac{\partial \mathbf{B}}{\partial t} \quad (3.14)$$

$$\nabla \times \mathbf{B} = \mu_0 \mathbf{j}_s + \epsilon_0 \mu_0 \frac{\partial \mathbf{E}}{\partial t} \quad (3.15)$$

The plasma itself is a collection of charged particles which can be described by their distribution in phase space through their average phase-space density given in equation 2.19. The evolution of this equation is the Vlasov equation, which gives the plasma behaviour in a collisionless plasma

$$\frac{\partial f_s}{\partial t} + \mathbf{v}_s \cdot \nabla_x f_s + \frac{q_s}{m_s} (\mathbf{E} + \mathbf{v}_s \times \mathbf{B}) \cdot \nabla_v f_s = 0 \quad (3.16)$$

The connection between the particle dynamics and the electromagnetic fields are incorporated in Maxwell's equations through the charge and current densities, which can be found from the particle distribution functions

$$\rho_s(\mathbf{x}, t) = \sum_s q_s \int f_s(\mathbf{x}, \mathbf{v}, t) d\mathbf{v} \quad (3.17)$$

$$\mathbf{j}_s(\mathbf{x}, t) = \sum_s q_s \int \mathbf{v}_s f_s(\mathbf{x}, \mathbf{v}, t) d\mathbf{v} \quad (3.18)$$



From this kinetic basis some fluid moments are incorporated to describe bulk properties of the plasma as a collective system of charged particles. Unlike in MHD, all the individual particle species are treated as separate fluids, and have different dynamics on different spatial and temporal scales. For each species separately, moments, as described by equation 2.24, can be taken of the distribution function and Vlasov's equation to return the particle density, bulk velocity and pressure, and the evolution of these, which are described by the continuity equation (2.29), the momentum equation (2.30), and the equation for the heat flux. For many space plasma systems it is assumed that the pressure behaves adiabatically to truncate the set of equations and neglect the heat flux and all higher order moments. Lastly, from the momentum equation Ohm's law can be derived to give an expression for the electric field

$$\mathbf{E} = -\mathbf{v}_s \times \mathbf{B} + \frac{1}{q_s n_s} \nabla \cdot \mathbf{P}_s + \frac{m_s}{q_s} \left( \mathbf{v}_s \cdot \nabla \mathbf{v}_s + \frac{\partial \mathbf{v}_s}{\partial t} \right) \quad (3.19)$$

Figure 3.5 shows an example of how the different terms in Ohm's law supports the reconnection electric field in and around the diffusion region. The set of equations listed here constitutes a full description of the self-consistent interaction between the plasma and the electromagnetic fields. In the remaining part of this chapter, features of magnetic reconnection important for the work done in the three papers included in this thesis that are captured through this description will be presented.

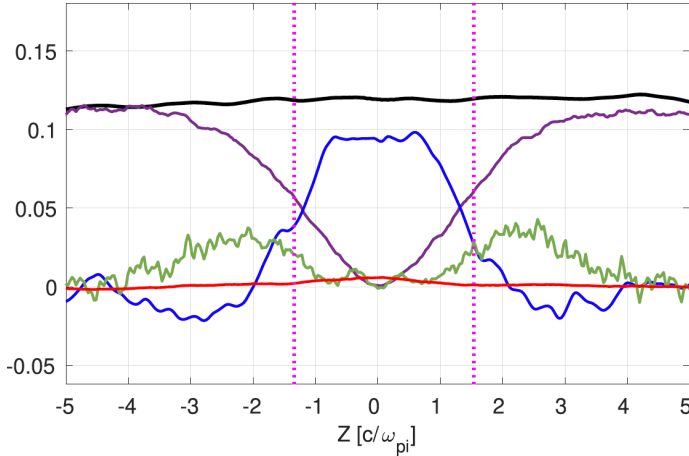


Figure 3.5: The reconnection electric field (black) along a cut in  $z$  through the x-point during reconnection in the baseline run from paper I in this thesis. The terms in Ohm's law supporting this field are the  $\mathbf{v} \times \mathbf{B}$  drift (purple), the pressure divergence (blue), and the spatial (green) and temporal (red) inertia.

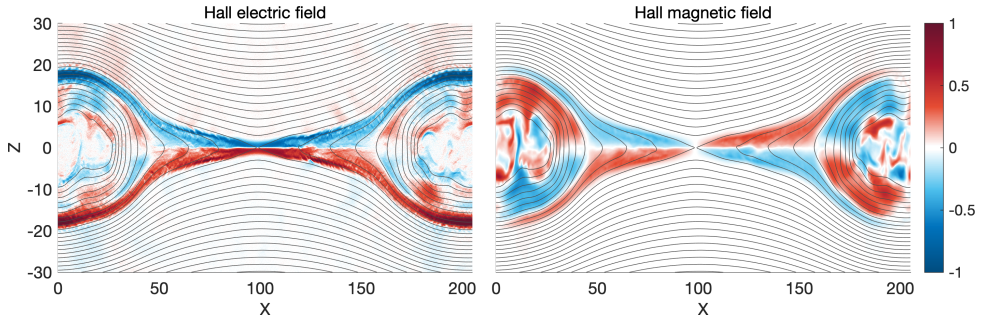


Figure 3.6: The Hall fields around an active reconnection site. The black contour lines show the topology of the magnetic field. This figure was created using data from the baseline run made for Paper II in this thesis.

### The Hall fields

Electrons and ions have vastly different intrinsic scales due to their different masses. The mass ratio between a proton and an electron is  $m_p/m_e \approx 1836$ . This means that the electrons have much less inertia than the protons, and will respond to changes in the electromagnetic fields much more easily, which is analogous to saying that the electrons are much more strongly coupled to the fields than the protons are. The gyrofrequency and gyroradius of a plasma particle around a magnetic field line is dependent on the particle mass, as seen in equations 2.11 and 2.12. When the plasma in the inflow region of magnetic reconnection approaches the reconnection site, the electrons and ions will react differently due to this difference in scales. The demagnetisation length scale of a particle, or its *inertial length*, is the same as its gyroradius for a particle gyrating at the Alfvén speed (Vasyliunas, 1975). This causes the protons to decouple from the magnetic field earlier than the electrons, allowing them to move across the magnetic field while the electrons are still frozen in. In this region, an electric field pointing towards the neutral line is generated due to the charge separation that occurs between the protons and electrons, called the *Hall electric field*, and the region itself is often referred to as the Hall region.

In the same region, the magnetic field exhibits a quadrupole structure in the initial current direction, perpendicular to the inflow and outflow. This is caused by the *Hall currents*, which are generated by the decoupled motion between the electrons and ions (M. Øieroset et al., 2001; Pritchett, 2003). The electrons are expelled into the outflow from the x-point at high velocity, creating electron jets along the x-direction. This constitutes a current in the opposite direction, which is closed by electrons flowing towards the x-point around the separatrix. The characteristic quadrupolar pattern of the Hall magnetic field is the result of these Hall currents. An example of the Hall fields dur-

ing active reconnection is given in figure 3.6. The presence of these Hall electric and magnetic field structures during reconnection have been both modeled and observed extensively (e.g. *Birn et al.*, 2001; *Eastwood et al.*, 2010; *M. Øieroset et al.*, 2001; *Shay et al.*, 1998)

### Multi-scale diffusion regions

The difference in the decoupling scale of the electrons and ions has fundamental impact on the diffusion region of magnetic reconnection. Since the heavier protons decouple from the magnetic field earlier than the light electrons, they can diffuse across the magnetic field further away from the reconnection site than the electrons can. This leads to a multi-scale diffusion region, where the diffusion region of the electrons will be a much smaller region embedded in the proton diffusion region. If the plasma also contains heavier particle species, such as helium or oxygen ions, the diffusion region will be further partitioned, with the lighter species diffusion regions being embedded in that of the heavier species, like a Matryoshka doll. The picture becomes even more nuanced when the particle temperature is taken into consideration. Both the gyroradius and gyrofrequency of a particle is dependent on its thermal velocity, and particles of the same species but with different temperatures will therefore have different demagnetization scales. Colder particles will behave as if they are lighter than their warmer counterparts since they will have a smaller gyroradius, and each species-determined diffusion region can therefore be further partitioned into temperature-determined subregions. A sketch of a multi-scale diffusion region in a plasma containing electrons, cold and warm protons and the heavy species oxygen is given in figure 3.7.

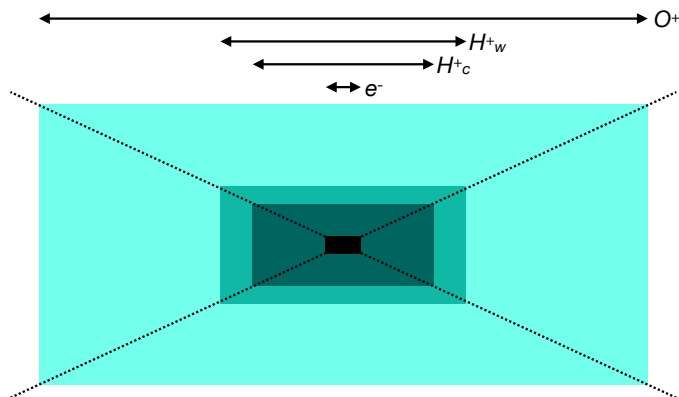


Figure 3.7: A schematic representation of a multi-scale diffusion region in a plasma consisting of electrons, cold and warm protons, and oxygen. The black dotted lines represent the separatrix.

The comparative size between the different regions is not to scale, but is meant for purely illustrative purposes. In reality, assuming the demagnetization scale is the gyroradius and the particles have the same temperature, the proton diffusion region is  $\sqrt{1836}$  times larger than the electron diffusion region due to their difference in mass (since  $r_g \sim \sqrt{mT}$ , and the oxygen diffusion region is a further 4 times larger than this again).

As mentioned earlier, magnetic reconnection can only take place when the frozen-in condition is broken for all particle species in the plasma. This means that reconnection only actually takes place in the electron diffusion region, since this is the particle species most closely coupled to the magnetic field. Still, the difference in demagnetization scales and consequentially the partitioning of the diffusion region have both been modelled and observed to affect the reconnection process in several ways, both in particle dynamics, field structure and reconnection efficiency (e.g. *Alm et al.*, 2019; *André et al.*, 2016; *Spinnangr et al.*, 2021b; *Tenford et al.*, 2018, 2019; *Toledo-Redondo et al.*, 2021).

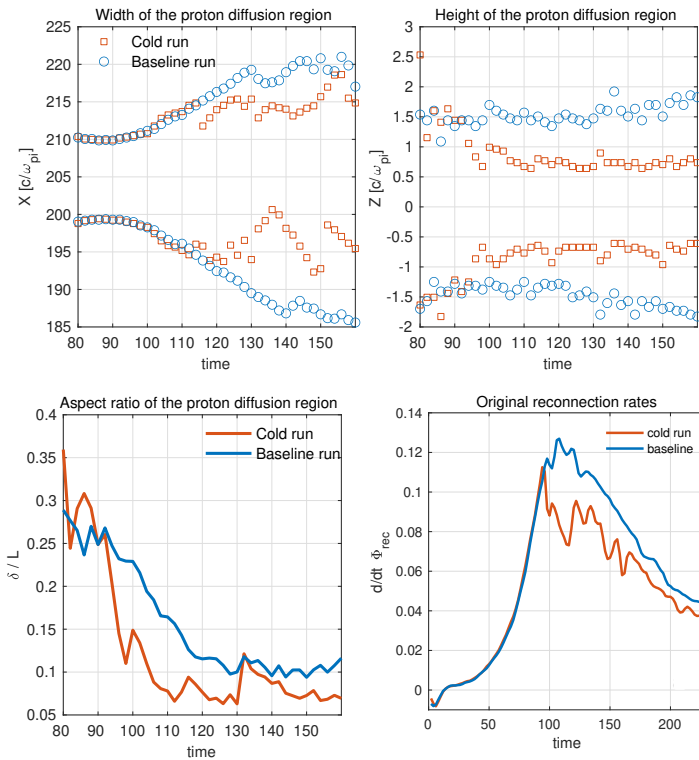


Figure 3.8: The top row shows the diffusion region width and height as a function of time for the total proton population in a simulation both cold and warm protons (red) and one containing only warm protons (blue). The bottom row shows the ratio between the height and width, i.e. the aspect ratio of the diffusion regions, and the reconnection rates. The figure is a modified version of figures from Paper I in this thesis.

Figure 3.8 shows an example of this from *Spinnangr et al.* (2021b). Here a cold proton population is inserted into the inflow region of a typical reconnection event, which eventually reaches the reconnection site and is allowed to interact with the reconnection process. As this happens, the size of the total proton diffusion region becomes smaller, and its aspect ratio is similarly affected. Based on Sweet-Parker scaling analysis, the aspect ratio of the ion diffusion region can be used to estimate the reconnection rate (*Vasyliunas, 1975*), and as can be seen in figure 3.8 there is a similar reduction in the reconnection rate as the proton diffusion region is reduced.

### Scaling of the reconnection rate

The reduction of the reconnection rate associated with the reduction in the aspect ratio of the diffusion region can also be explained by mass-loading arguments. In *Spinnangr et al.* (2021b), the cold ions increased the inertia of the inflow flux tubes and slowed down the reconnection process. The reconnection electric field, which is just another expression for the reconnection rate, scales with the factor  $B_x v_A$  (*Cassak et al., 2017; Comisso and Bhattacharjee, 2016; Liu et al., 2017*), with both  $B_x$  and  $v_A$  measured in close vicinity to the diffusion region. When we mass-load the inflow region by adding additional mass which slows down the flux transport, we effectively reduce the Alfvén velocity by a factor given through the mass density in the inflow,  $\sqrt{1 + n_{i^*} m_{i^*} / n_i m_i}$  where the asterisk indicates the mass-loading species. As shown in *Spinnangr et al.* (2021b), the reconnection rate was not affected until the cold ion front reached the current sheet and participated in the reconnection process. There, the mass-loading was due to an additional density front of cold ions of the same species as the other ions in the system, but it can also be due to interaction with heavier ions such as oxygen (*Kolstø et al., 2020a; Tenfjord et al., 2019*). Mass-loading effects on magnetic reconnection has also been observed in both day-side and night-side reconnection (e.g. *Fuselier et al., 2017, 2019; Su et al., 2000; Walsh et al., 2013, 2014a; Wang et al., 2015*), and the predicted reduction in the reconnection rate has been estimated to be up to 20 – 30% (*Fuselier et al., 2019; Wang et al., 2015*).

If the inflow regions of the reconnecting system are not symmetric, the reconnection rate will also be affected. This is typical in for example reconnection on the dayside of the Earth’s magnetosphere, where the density, temperature, magnetic field strength and the shear angle between the reconnecting fields might be significantly different across the separating current sheet. *Cassak and Shay (2007)* found a general expression for the

reconnection electric field in any asymmetric configuration

$$E \sim \left( \frac{B_1 B_2}{B_2 + B_1} \right) v_{out} \frac{2\delta}{L} \quad (3.20)$$

where  $B_1$  and  $B_2$  are the asymmetric magnetic field magnitudes in the inflow regions,  $v_{out}$  is the outflow speed, and  $\frac{\delta}{L}$  is the aspect ratio of the ion diffusion region. Equation 3.20 can be interpreted as the reconnection electric field based on the effective magnetic field in the inflow. A general scaling relation for asymmetric magnetic reconnection allows us to scale reconnection rates to be comparable across different parameter schemes such that symmetric systems, as well as systems with various asymmetries can be compared. Both simulations and observations of various reconnecting systems have shown that in general the steady-state reconnection rate has a value in the order of  $\sim 0.1$  (e.g. *Cassak et al.*, 2017; *Comisso and Bhattacharjee*, 2016; *Dargent et al.*, 2020; *Liu et al.*, 2017; *Shay et al.*, 1999; *Yamada et al.*, 2010)

### The origin of the reconnection electric field

Magnetic reconnection can only be enabled by a small diffusion region where the reconnection electric field exists, which is necessary to break the frozen-in condition and allow particles to diffuse across magnetic field lines. In collisionless magnetic reconnection, the origin of this electric field is not obvious, but it can be understood by taking a closer look at Ohm's law (equation 3.19). For each particle species in the plasma, this equation must hold everywhere. Since the electrons are most tightly coupled to the magnetic field, the reconnection electric field must be supported by their dynamics. At the x-point where reconnection takes place, the magnetic field vanishes, and since the electrons are so light and fast, the contribution from the inertia terms is negligible. This assumption breaks down for very thin current sheets comparable to the electron inertial length, where the electron inertia again becomes important and might produce very fast reconnection rates (*Hesse et al.*, 1999). For thicker current sheets, the only remaining term to support the electric field is then the pressure divergence. It has been shown extensively that for current sheets with a thickness comparable to the ion inertial length, the reconnection electric field is generated through the non-gyrotropic contributions of the electron pressure tensor (e.g. *Cai and Lee*, 1997; *Hesse and Schindler*, 2001; *Hesse and Winske*, 1993; *Hesse et al.*, 1999, 2001a; *Kuznetsova et al.*, 1998; *Vasyliunas*, 1975). In symmetric magnetic reconnection without a guide field and the directions of the coordinate system defined as described earlier in this chapter, the contribution to the reconnection electric field becomes

$$E_y = -\frac{1}{n_e e} \left( \frac{\partial P_{exy}}{\partial x} + \frac{\partial P_{eyz}}{\partial z} \right) \quad (3.21)$$

The origin of the reconnection electric field from the non-gyrotropic electron pressure can be thought of as an inertial effect resulting from the random motion of thermal electrons as they bounce in the electron diffusion region. By investigating the contributing terms to the evolution of the current density, it has been shown that the main role of the reconnection electric field is to maintain the current density at and around the x-point, which would otherwise have been disrupted by the random thermal motions of the electrons (*Hesse et al.*, 2018). The existence of the reconnection electric field is also a consequence of Ampère’s law (equation 2.16) for a reconnecting geometry. If for some reason the curl of the magnetic field and the current density are not balanced, an electric field will be generated to make up for this difference, which is described by the time derivative term in Ampère’s law, often referred to as the displacement current. Since the electrons are so light, this happens almost instantaneously, and this time derivative of the electric field is often neglected since it will be very small. However, the continuous effect of the displacement current is to regulate the current density such that it balances the magnetic geometry, and the reconnection electric field can therefore be understood as a necessary consequence of the plasma dynamics in the electron diffusion region (*Hesse et al.*, 2018).

### Asymmetric and guide field reconnection

In real reconnecting systems in nature, the magnetic fields in the inflow region are not necessarily exactly equal and oppositely aligned. The field strength might be different in the two inflow regions, and the magnetic shear angle between the regions might not be exactly 180°. The first case is referred to as asymmetric reconnection, while the latter case is referred to as *guide field reconnection* or *component reconnection*, since only the components of the total magnetic field that are exactly oppositely aligned will reconnect. A reconnecting system might be both asymmetric without a guide field, asymmetric with a uniform guide field, or asymmetric with an asymmetric guide field, and transitions between these states can happen during a reconnection event. When the magnetic fields are asymmetric, the density and temperature of the plasma are also oppositely asymmetric due to the force balance between the electromagnetic forces and the plasma pressure forces which holds the system in an equilibrium. Arguably, the most obvious example of such a system is at the dayside of the magnetosphere, where the warmer, denser solar wind plasma with the IMF meets the Earth’s magnetic field with its colder, less dense magnetospheric plasma. During asymmetric reconnection, the geometry and dynamics of the electron diffusion region become more complicated

compared to symmetric reconnection. Since the inflow magnetic fields have different magnitudes, the particle velocities must be oppositely asymmetric for the flux transport to be symmetric. This means that the electron flow stagnation point will be displaced further into the high magnetic field side than the x-point (e.g. *Birn et al.*, 2008; *Cassak and Shay*, 2007; *Hesse et al.*, 2014, 2021). The electron flow across the x-point towards the flow stagnation point carries a current, causing the current maximum to be positioned between these two locations (*Hesse et al.*, 2021). On larger scales, the geometry of the Hall electric and magnetic fields are also modified for asymmetric reconnection. On the high density and low magnetic field side of the reconnection region they are expanded over a larger area since the outflow tends to expand towards this side (*Eastwood et al.*, 2013; *Mozer et al.*, 2008; *Pritchett*, 2008).

The presence of a guide field alters the reconnection process in several ways, which has been shown through large-scale modeling and theoretical efforts, as well as through observations (e.g. *Fuselier et al.*, 2011; *Trattner et al.*, 2007, 2017). In most cases of day-side reconnection, where the Earth’s magnetic field connects directly with the IMF, the magnetic fields are not strictly anti-parallel, and observations of nightside reconnection including a guide field have also been made (*M. Øieroset et al.*, 2001). Compared to a strictly anti-parallel scheme, the presence of a guide field alters the dynamics and global behaviour of the reconnection process on all scales, both through the kinetic behaviour of the particles in the diffusion region (*Goldman et al.*, 2011; *Pritchett and Mozer*, 2009) and the global configuration and efficiency of reconnection as a whole (*Pritchett*, 2005a; *Pritchett and Coroniti*, 2004; *Swisdak et al.*, 2005; *Trattner et al.*, 2017). The reconnection rate has been shown to be lower during guide field reconnection than anti-parallel reconnection. From theoretical predictions, reconnection with a strong guide field is expected to reconnect in the order of 30% slower (*Hesse et al.*, 2004; *Pritchett*, 2001), while some observations suggest guide field reconnection could be as much as 10 times slower (*Fuselier et al.*, 2010; *Mozer and Retinò*, 2007). The geometry of the Hall electric and magnetic fields are also affected by a guide field, and a left-right asymmetry will occur. For the Hall magnetic field, the two regions of the quadrupole pointing in the same direction as the guide field will be enhanced, while the remaining two will be suppressed. Due to the outflow electrons accelerated by the guide field ( $E_z \sim v_x B_y$ ), the Hall electric field will be modified with an additional contribution. The electron dynamics are also modified by the guide field, which causes the electron outflow jets to be deflected along the separatrices (*Goldman et al.*, 2011).

In paper II of this thesis (*Spinnangr et al.*, 2021a), we investigated how reconnection was affected by having a varying guide field in one of the inflow regions. Among our results were clear variations in the reconnection rate and flux transport associated with the variations in the force balance between the inflow regions, and significant changes



in the structure of the reconnection outflow. By comparing to a strictly anti-parallel simulation, we found that it converted about 12% more magnetic energy in the same amount of time than when the magnetic field direction was varying, consistent with reconnection with a uniform guide field (*Huba, 2005; Ricci et al., 2004; Swisdak et al., 2005*).

### Diamagnetic effects

In chapter 2 some plasma drifts resulting from single particle dynamics were described. Since the plasma is a collection of interacting particles, important plasma drifts can also originate from collective effects in the plasma. One of these is the diamagnetic drift, which occurs if there is a pressure gradient in the plasma transverse to the direction of the magnetic field. The diamagnetic drift is directed perpendicular to both the magnetic field and pressure gradient, and can be derived by assuming the pressure is anisotropic and taking the cross product of the equation of motion with  $\mathbf{B}/B^2$  (*Baumjohann and Treumann, 2012*)

$$\mathbf{v}_{sD} = \frac{\nabla p_{s\perp} \times \mathbf{B}}{q_s n_s B^2} \quad (3.22)$$

Since the diamagnetic drift velocity is charge dependent, electrons and ions will drift in the opposite direction, generating a diamagnetic current from the total pressure gradient  $p_{\perp} = p_{i\perp} + p_{e\perp}$

$$\mathbf{j}_D = \frac{\nabla p_{\perp} \times \mathbf{B}}{B^2} \quad (3.23)$$

There is no net transport of particles associated with a diamagnetic current or drift, it rather originates from a difference in the gyration around the magnetic field between regions of different pressure. The pressure gradient sustaining a diamagnetic drift can be due to a difference in particle density or temperature, or a combination of both, since  $\nabla p = \nabla(nT) = \nabla nT + n\nabla T$  (*Liu and Hesse, 2016*). If the pressure gradient originates from a gradient in the density, the diamagnetic drift is explained by the difference in the number of particles, which are moving in the opposite direction of each other during their gyration along the density gradient. None of the gyrocenters of the particles are actually moving in the drift direction, but the net result of their gyration is that more particles are gyrating in one direction where the density is high compared to where the density is lower. This is illustrated in figure 3.9.

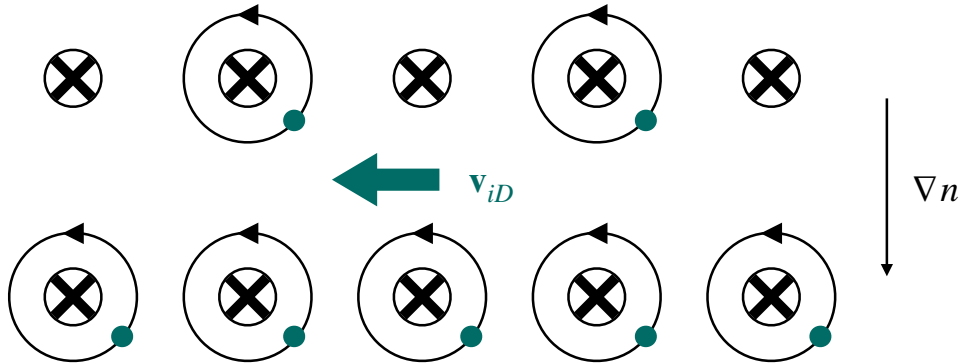


Figure 3.9: An illustration of diamagnetic drift of positive ions resulting from a density gradient. The magnetic field points into the plane, and the gyrating particles are represented by the green dots.

One of the most important diamagnetic currents in space physics is the *neutral sheet current*, which separates the northern and southern lobe of the geomagnetic tail (*Baumjohann and Treumann, 2012*). It points in the dawn-dusk direction, and is generated due to the pressure gradients pointing southward in the northern lobe and northward in the southern lobe. When magnetic reconnection occurs in the geomagnetic tail, it initially does so in this pre-existing current sheet, and the resulting reconnection current points in the same direction as the diamagnetic current. In paper I of this thesis (*Spinnangr et al., 2021b*), we investigated how reconnection was affected by the inclusion of cold ions in the inflow regions. One of the main results involved the reduction of the reconnection electric field due to a negative contribution from the temporal inertia caused by the cold ions as they entered the reconnection site. We showed that this was a transient effect of the cold ion dynamics which were later overcome by the diamagnetic drift as the cold ions gained enough temperature.

Even though there is no net plasma transport caused by the diamagnetic drift, the magnetic field can still be transported as a consequence of it. If the reconnecting system includes some contribution from a guide field near the field reversal region, a diamagnetic drift can occur in the reconnection plane. This can lead to a convection of the x-point in the outflow direction consistent with the in-plane diamagnetic drift of the electrons (*Swisdak et al., 2003*). This causes a left-right asymmetry in the reconnection outflow velocities, since the total outflow becomes the sum of the reconnection outflow and the diamagnetic drift, which on one side of the reconnection site will enhance each other, while on the other they will work in opposite directions. Consequentially, it has been shown that such in-plane diamagnetic convection of the x-point can inhibit magnetic reconnection by limiting the efficiency of the reconnection outflow. This is

called *diamagnetic suppression* and can severely limit the reconnection rate for high values of the diamagnetic drift, and even completely suppress it for drift speeds on the order of the Alfvén velocity (*Beidler and Cassak, 2011; Eastwood et al., 2013; Liu and Hesse, 2016; Swisdak et al., 2003*). This velocity limit for diamagnetic suppression,  $v_D > v_A$ , can be rewritten in terms of the plasma- $\beta$ , which is the ratio between the plasma and magnetic pressures in the plasma, where magnetic reconnection does not occur if the suppression criteria is achieved

$$\beta_x > \frac{B_y}{B_x} \frac{2L_p}{c/\omega_{pi}} \quad (3.24)$$

where  $\beta_x = 8\pi nT/B_x$  and  $L_p$  is the scale length of the pressure gradient. A recent statistical survey of data of interlinked magnetic field line events at the dayside magnetosphere showed a possible connection between the diamagnetic suppression criterion and flux pile-up before magnetic reconnection, suggesting reconnection had been suppressed until the plasma- $\beta$  had been sufficiently reduced (*Maheshwari et al., 2022*).

---

In this chapter, the process of magnetic reconnection has been discussed in detail. Different models have been presented, ranging from older, simple models such as the Sweet-Parker model to the modern, multi-scale, kinetic descriptions used today. The literature in this field of research is extensive, and the amount of research and knowledge about magnetic reconnection has seen an explosive growth in the past few decades with the advance of computer power and spacecraft technology. The scope of this thesis is to create a foundation of knowledge relevant for the research performed and presented in the three papers of this thesis, and naturally many aspects related to magnetic reconnection that might be important in other scenarios have not been discussed. In the next chapter, Particle-In-Cell simulations will be discussed, which is the method we have employed to do our investigations of magnetic reconnection in the three papers.



## Chapter 4

# Studying Magnetic Reconnection through Numerical Simulation

The development of computers had its early beginning in the late 1930's (*Computer History Museum (n.d.)*). The first computer program was successfully developed in Manchester and run on a computer in 1948 and contained only 17 instructions. During the next two decades the computation technology had a slow and steady development, and it wasn't until the early 1970's the first microprocessor was introduced, capable of performing 90000 operations per second. During the early 1970's, the first parallel computing machine was used at NASA Ames Research Center. It had a computational speed of 200 million instructions per second and 1 billion bits per second. The development of faster and more reliable supercomputers continued through the late twentieth century, with an ever increasing number of calculations performed per second. Notable developments were Intel's Touchstone in 1992, which was capable of performing 32 billion computations per second, and IBM's ASCI Red only five years later in 1997 which was capable of 1.3 trillion computations per second. The speed of supercomputers and computer technology in general sees an explosive development during the 2000's and until today, while the technology also becomes ever smaller in physical size. Today the speed of supercomputers are in the range of several petaflops and parallel computing capabilities are considered a given. For example, the supercomputer Betzy in Trondheim, which the simulation in Paper III of this thesis is performed on (*Spinnangr et al., 2022*), is capable of running 6.2 thousand trillion computations per second (*Sigma2/NRIS, 2023*).

The increase in computer power seen in the last decades has enabled increasingly complex models of physical processes to be performed. Computer simulations offer a third alternative method to investigate nature in addition to analytical theory and observations, and has had a tremendous impact on our ability to study and understand plasma

physics on both large and small scales (*Pritchett, 2003*). The two main approaches to simulate plasma physics are fluid simulations based on the magnetohydrodynamic equations, which is well suited for large scale plasma phenomena, and the kinetic approach which treats the plasma as a collection of individual particles and is best suited for the small and fast scale processes in a plasma system (*Pritchett, 2003*). A limit on our ability to simulate real, large plasma systems in great detail will always be the sheer number of necessary calculations needed to recreate the real system of interacting plasma particles and electromagnetic fields. Particle-In-Cell (PIC) models are among the most sophisticated simulation systems used for scientific modeling today, and is very well suited for simulating kinetic plasma processes due to its capability of accurately tracking the plasma position and velocity during dynamical processes.

In this chapter, a detailed presentation of PIC as a simulation tool for magnetic reconnection will be provided. Starting from an assumed initial magnetic geometry with a current sheet structure and an initial particle distribution, PIC simulations solve the fully kinetic equations for the plasma particle dynamics in the self-consistently generated electromagnetic fields. Emphasis will be given to the description of the step-by-step process in which the calculations are performed which enables the simulation of reconnection through a set of self-consistent, non-linear, fully kinetic equations as discussed in chapter 3. There are several different ways of setting up a PIC code to solve a variety of plasma systems, including different spatial grid configurations, time advancing schemes, different solvers and ways of representing the particles, and different interpolation methods. These are well documented in the literature (e.g. *Büchner et al., 2003*; *Dawson, 1983*; *Forsslund, 1985*; *Pritchett, 2003*), and for the most part only what is relevant for the PIC code used in the three papers in this thesis will be discussed in detail here. This code was originally developed by Michael Hesse, and has been well-proven to successfully predict features of reconnection later verified by in-situ observations (e.g. *Hesse et al., 1999, 2001b, 2011, 2014*)

## 4.1 Particle-In-Cell simulation

The modern PIC method is based on the simulation of *macroparticles*, which is a representation of a set of real particles, existing on a grid of distinct cells. This method was developed in order to reduce the computational cost of simulating each particle as a distinct point in space and calculating the forces acting on each particle explicitly by the interaction with the remaining ( $N - 1$ ) particles (*Pritchett, 2003*). In PIC simulations, macroparticles move freely across the spatial grid, but their current density and charge are interpolated onto the grid for each calculation step, where the field equations

are solved. The forces acting on the particles resulting from this interaction are then interpolated back to the position of the macroparticle. This method reduces the number of necessary computations for each calculation step from  $\sim N^2$  to  $\sim N \log N$ , which enables the simulation of much more realistic plasma systems (Pritchett, 2003). When simulating magnetic reconnection using kinetic PIC simulations, a system with certain initial conditions is first defined which is then evolved using the coupled system of equations comprised of Maxwell's equations for the fields and Newton's equation of motion for the macroparticles (Lapenta, 2015; Markidis et al., 2010; Pritchett, 2003). The new particle position and velocity after one time step,  $\Delta t$ , is given by

$$\begin{aligned}\mathbf{x}_p^{new} &= \mathbf{x}_p^{old} + \mathbf{v}_p^{old} \Delta t \\ \mathbf{v}_p^{new} &= \mathbf{v}_p^{old} + \frac{\mathbf{F}_p}{m_p} \Delta t\end{aligned}$$

where  $\mathbf{F}_p = \sum_{p'}^N \mathbf{F}_{pp'}$  is the the sum of the electromagnetic forces on the particle. The collisionless transport of the macroparticles in phase space is described by the Vlasov equation, and the system of equations is often referred to as the Maxwell-Vlasov system (Markidis et al., 2010). Depending on how the initial system is defined, this allows us to simulate a huge amount of different dynamical plasma processes. In all the simulations in this thesis, the reconnecting system has been initiated as a central current sheet with a magnetic topology including two oppositely aligned regions above and below it. One of the most common setups for the current sheet is the *Harris sheet*, which is defined by a magnetic field profile and a density profile given by (Birn et al., 2001; Harris, 1962)

$$B_x(z) = B_0 \tanh(z/L) \quad (4.1)$$

$$n(z) = n_0 \operatorname{sech}^2(z/L) \quad (4.2)$$

A plot of these profiles is given in figure 4.1.

### 4.1.1 Macroparticles

A macroparticle or computational particle is a collection of real particles which exist close to each other and move with the same velocity. In other words, each macroparticle is a discrete section of phase space. In this way, the Particle-In-Cell approach is based



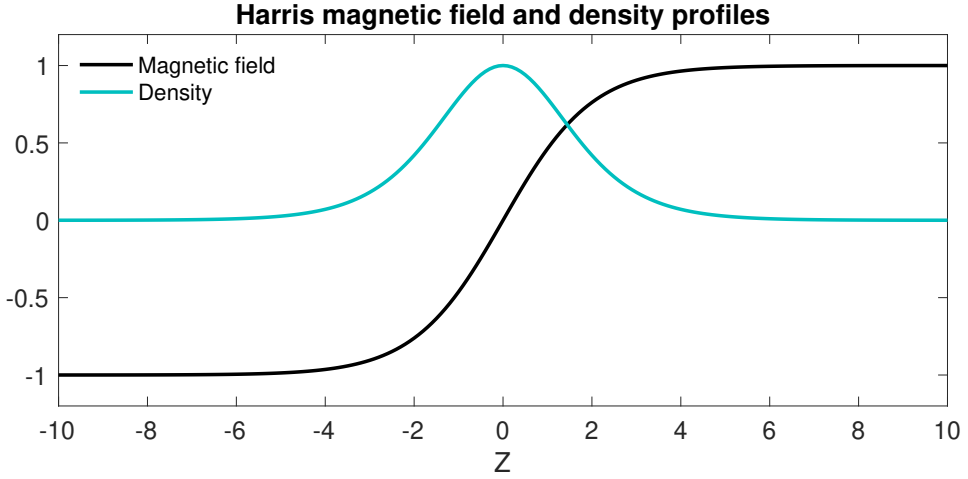


Figure 4.1: An example of the typical profiles of the Harris magnetic field and density configuration used as initial conditions in many PIC simulations.

on the discretization of the phase space distribution function,  $f(\mathbf{x}, \mathbf{v}, t)$ . Similarly to the way the electric potential from point particles are modified to the Debye potential due to shielding effects in a plasma, the electric potential of macroparticles is different from that of point particles. To simulate the collective behaviour of a real plasma with comparatively few macroparticles, the macroparticles must still behave as free particles influenced by the collective field of a large collection of other particles, i.e. as a collection of weakly interacting particles. This means the plasma parameter as defined in chapter 2 must still be large,  $\Lambda \gg 1$ , which is just another way of saying the potential energy from each macroparticle must be much less than the collective thermal energy. This is achieved by letting the macroparticles behave like charged clouds that are allowed to pass through each other (Dawson, 1983). The macroparticles then behave like point particles when the separation between them is large, but the electric potential drops to zero when they overlap instead of approaching infinity which is the case for point particles. This behaviour is illustrated in the left panel in 4.2 for spherical macroparticles. The modified behaviour of the electric potential of macroparticles facilitates the simulation of realistic plasma interactions using fewer particles, which significantly decreases the computation time and memory cost (Lapenta, 2015).

The shape of the macroparticle in phase space is defined by shape functions, which define how the density and charge is distributed in the macroparticle (Dawson, 1983). For each particle species in the plasma there exists a distribution function,  $f_s(\mathbf{x}, \mathbf{v}, t)$ , who's evolution in a collisionless plasma is described by the Vlasov equation as defined in chapter 2. In PIC, this distribution function is given by the superposition of the distribution functions of all the macroparticles,  $f_p(\mathbf{x}, \mathbf{v}, t)$  (Lapenta, 2015)

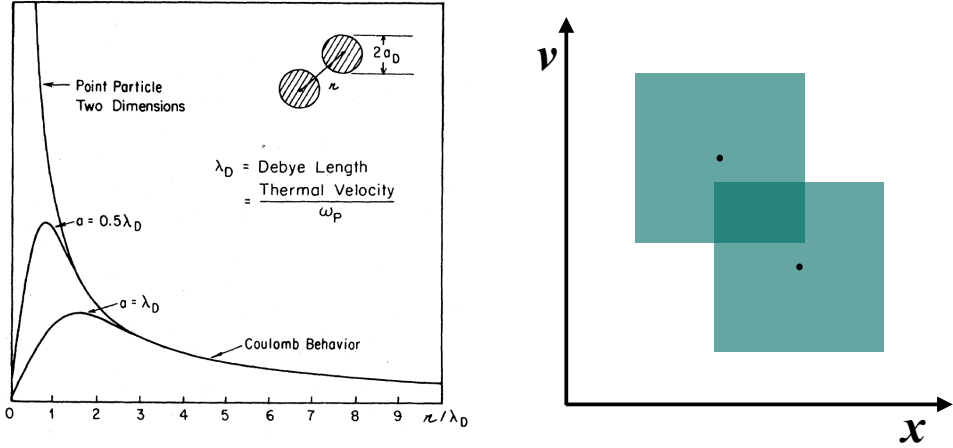


Figure 4.2: The left panel shows a comparison between the Coloumb potential and the potential of two spherical macroparticles as a function of separation. Reproduced from (Dawson, 1983). The left panel shows two quadratic macroparticles in phase space. Where they overlap the electric potential goes to zero. The black dots mark the center of the macroparticles.

$$f_s(\mathbf{x}, \mathbf{v}, t) = \sum_p f_p(\mathbf{x}, \mathbf{v}, t) \quad (4.3)$$

The shape functions,  $S$ , define how the macroparticle is distributed in phase space, which together with the number of real particles the macroparticle represents gives the distribution function of each macroparticle

$$f_p(\mathbf{x}, \mathbf{v}, t) = N_p S_x(\mathbf{x} - \mathbf{x}(t)) S_v(\mathbf{v} - \mathbf{v}(t)) \quad (4.4)$$

The functional form of the shape functions can vary, but by definition they should be zero outside a defined region of phase space, and their integral over the full phase space should equal unity,  $\int_{-\infty}^{\infty} S_\xi(\xi - \xi_p) d\xi = 1$ , where  $\xi$  is any phase space coordinate. The shape functions are also often chosen to be symmetrical,  $S_\xi(\xi - \xi_p) = S_\xi(\xi_p - \xi)$  to make it easier, though it is not a necessary requirement (Lapenta, 2015). The restrictions on the shape functions leave room for choice in both phase space directions. A typical choice for the velocity shape function is the Dirac-delta function defined in chapter 2, since it ensures that the particles within the phase space element defined as a macroparticle stay together during its evolution

$$S_v(\mathbf{v} - \mathbf{v}(t)) = \delta(\mathbf{v} - \mathbf{v}(t)) \quad (4.5)$$

In configuration space, the shape functions are typically defined by different orders of the b-spline functions (*Lapenta, 2015; Markidis et al., 2010; Shalaby et al., 2017*). These are  $n$ -dimensional basis functions which can build spline functions through linear combination and takes the general form (*de Boor, 1978*)

$$b_n(\xi) = \int_{-\infty}^{\infty} d\xi' b_0(\xi - \xi') b_{n-1}(\xi') \quad (4.6)$$

where the zeroth order b-spline,  $b_0$  is defined as

$$b_0(\xi) = \begin{cases} 1, & \text{if } \xi < \frac{1}{2} \\ 0, & \text{otherwise} \end{cases} \quad (4.7)$$

The first three orders of the b-spline function are shown in figure 4.3. Using these functions, the configurational shape function is defined as

$$S_{\mathbf{x}}(\mathbf{x} - \mathbf{x}(t)) = b_n \left( \frac{\mathbf{x} - \mathbf{x}(t)}{\Delta \mathbf{x}} \right) \quad (4.8)$$

where  $\Delta \mathbf{x}$  is the size of the grid cells (*Lapenta, 2015*). For particles defined with the zero-order b-spline, the size of the particle is the same as the grid size (*Dawson, 1983*). In the simulations used in this thesis we use the zeroth order b-spline function, which is often referred to as the Cloud-In-Cell method (*Lapenta, 2015; Markidis et al., 2010*) since it simulates the macroparticles as a finite, square charge cloud in configurational space and with an infinitesimal spread in velocity space.

Since the total distribution function for each particle species,  $f_s(\mathbf{x}, \mathbf{v}, t)$  satisfies the Vlasov equation, and it is a linear superposition of the distribution function of the macroparticles,  $f_p(\mathbf{x}, \mathbf{v}, t)$ , they must also satisfy the Vlasov equation. This can be verified by taking the moments of the Vlasov equation as described in chapter 2, using the macroparticle distribution function to derive the conservation equation for the particle number and their equations of motion. The zeroth moment returns the conservation of particle number for the macroparticles,  $N_p$ , since only the first term in the Vlasov equation contributes

$$\iint \frac{\partial f_p}{\partial t} + \mathbf{v} \frac{\partial f_p}{\partial \mathbf{x}} + \frac{q_s}{m_s} (\mathbf{E} + \mathbf{v} \times \mathbf{B}) \frac{\partial f_p}{\partial \mathbf{v}} d\mathbf{x} d\mathbf{v} = 0 \quad \rightarrow \quad \frac{dN_p}{dt} = 0$$

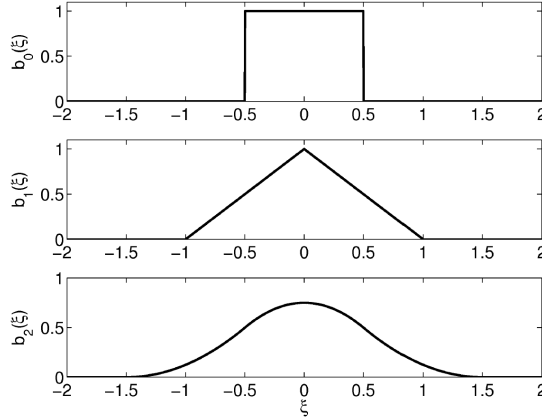


Figure 4.3: The first three orders of the b-spline function. Reproduced from (*Lapenta, 2015*).

The first order moment in  $\mathbf{x}$  gains a contribution from the first and second term, which together give the equation for the macroparticle velocity,  $\mathbf{v}_p$ , based on its position,  $\mathbf{x}_p$

$$\begin{aligned} \iint \mathbf{x} \frac{\partial f_p}{\partial t} + \mathbf{x} \mathbf{v} \frac{\partial f_p}{\partial \mathbf{x}} + \mathbf{x} \frac{q_s}{m_s} (\mathbf{E} + \mathbf{v} \times \mathbf{B}) \frac{\partial f_p}{\partial \mathbf{v}} d\mathbf{x} d\mathbf{v} = 0 &\rightarrow \frac{dN_p \mathbf{x}_p}{dt} - N_p \mathbf{v}_p = 0 \\ &\rightarrow \frac{d\mathbf{x}_p}{dt} = \mathbf{v}_p \end{aligned}$$

Similarly, the first order moment in  $\mathbf{v}$  gains a contribution from the first and last term, which returns the expression for the acceleration of the macroparticle due to the electromagnetic forces

$$\begin{aligned} \iint \mathbf{v} \frac{\partial f_p}{\partial t} + \mathbf{v} \mathbf{v} \frac{\partial f_p}{\partial \mathbf{x}} + \mathbf{v} \frac{q_s}{m_s} (\mathbf{E} + \mathbf{v} \times \mathbf{B}) \frac{\partial f_p}{\partial \mathbf{v}} d\mathbf{x} d\mathbf{v} = 0 \\ \rightarrow \frac{dN_p \mathbf{v}_p}{dt} + N_p \frac{q_s}{m_s} (\mathbf{E}_p + \mathbf{v}_p \times \mathbf{B}_p) = 0 \rightarrow \frac{d\mathbf{v}_p}{dt} = \frac{q_s}{m_s} (\mathbf{E}_p + \mathbf{v}_p \times \mathbf{B}_p) \end{aligned}$$

The final equations from this are on the same form as the familiar Newtonian equations of motion for real particles

$$\frac{dN_p}{dt} = 0 \quad , \quad \frac{d\mathbf{x}_p}{dt} = \mathbf{v}_p \quad , \quad \frac{d\mathbf{v}_p}{dt} = \frac{q_s}{m_s} (\mathbf{E}_p + \mathbf{v}_p \times \mathbf{B}_p) \quad (4.9)$$

where the electromagnetic fields are the average fields acting on the macroparticle which comes from the integration with the distribution function (*Markidis et al.*, 2010)

$$\mathbf{E}_p = \mathbf{E} \int S_{\mathbf{x}}(\mathbf{x} - \mathbf{x}(t))d\mathbf{x} \quad , \quad \mathbf{B}_p = \mathbf{B} \int S_{\mathbf{x}}(\mathbf{x} - \mathbf{x}(t))d\mathbf{x} \quad (4.10)$$

To use this to simulate realistic plasma, the PIC method introduces a grid of Eulerian cells which the macroparticles move in and across. By interpolating between the position of the macroparticles and the grid, the number of calculations needed for each time step in the evolution is greatly reduced (*Eastwood*, 1986; *Shalaby et al.*, 2017).

### 4.1.2 The cell grid

The PIC method is based on the discretization of space by introducing an Eulerian grid of Cartesian cells which the macroparticles move across. Since the use of macroparticles with the zeroth order b-spline function distributes the charge density evenly over the size of the particle, the size of the grid cells are usually the same as the size of the macroparticle when using this shape function (*Dawson*, 1983). For higher order b-spline functions, the macroparticle will be larger than the grid size. Figure 4.4 shows an illustration of one cell in the grid such as it is defined in our simulations in this thesis. The grid is staggered, with one grid representing the actual cells and another identical grid shifted half a grid-size to intersect the center of each cell. This shift is done to enable the calculation of the spatial gradients of the fields and the current (*Pritchett*, 2003). The coloured points in the grid to the left in figure 4.4 indicate the position of control points, where the quantities necessary for calculations are interpolated to. The dark blue points mark the corners of the cell, where  $E_y$  is defined. The dark red points on the cell vertices mark where  $B_z$  and  $E_x$  are defined, while the pink points mark where  $B_x$  and  $E_z$  are defined. Finally, the turquoise point at the center of the cell mark where  $B_y$  is defined.

As mentioned earlier, the macroparticles are free to move across the grid. However, for each time the forces are calculated, the charge and current density of the particles must be defined on the same grid points as the electromagnetic fields (*Birdsall and Langdon*, 1991). This is achieved by interpolating the charge and current density of the macroparticles who's center is within a cell onto the control points on the cell vertices. The density is distributed to the points on the corners of the cell, and what fraction of the density is given to each point is determined by weight functions,  $w$ , which are directly proportional to the distance between the center of the macroparticle and the cell corners. This is illustrated for one macroparticle in the panel to the right in figure

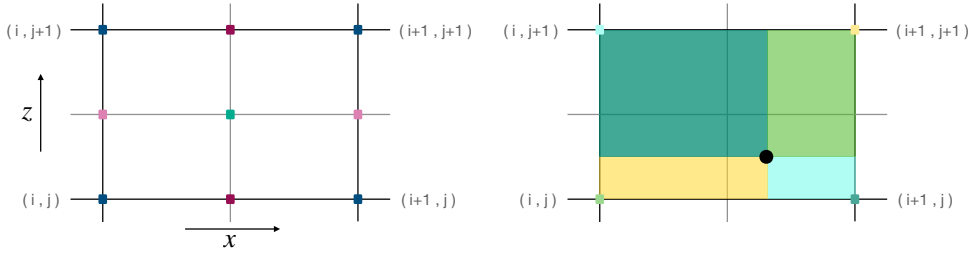


Figure 4.4: The left panel shows an illustration of one cell in the cell grid with the control points illustrated by coloured points. The dark blue points mark the corners of the main cell, while the lighter grey lines indicate the position of the additional grid intersecting the center of each cell. The panel on the right illustrates how the particle charge is distributed on the grid points. The black dot indicates the position of the center of a macroparticle.

4.4. The macroparticle is closest to the corner at  $(i + 1, j)$  and furthest from  $(i, j + 1)$ . The horizontal and vertical size of the cell is  $\Delta x$  and  $\Delta z$  respectively, and the distance from the particle to the corner at  $(i, j)$  is given by  $\delta_x$  and  $\delta_z$ . The weight functions for a given corner can then be calculated by calculating the area spanned by the particle position and the corner directly opposite to the relevant corner.

For example, the weight function for the corner at  $(i + 1, j + 1)$  in figure 4.4, normalized to 1 by dividing on the full cell area, is given by the yellow area

$$w_{(i+1,j+1)} = \frac{\delta_x \delta_z}{\Delta x \Delta z} \quad (4.11)$$

while the weight function for the closest corner at  $(i + 1, j)$  is given by the large teal area

$$w_{(i+1,j)} = \frac{\delta_x (\Delta z - \delta_z)}{\Delta x \Delta z} \quad (4.12)$$

The charge density deposited on for example this corner by one macroparticle with charge  $q_p$  is then given by

$$\rho_{(i+1,j)} = q_p w_{(i+1,j)} \quad (4.13)$$

Similarly, all the components of  $B$  and the  $x$  and  $z$  components of  $E$  are interpolated to the cell corners by finding the average field from the nearest neighbor points where they are defined. For  $E_x$ ,  $E_z$ ,  $B_x$  and  $B_z$  this is an average over two grid points, while it is an average over four grid points for  $B_y$ . Since  $E_y$  is already defined at the cell corners,

it is not averaged. Once the charge, current density and all the electromagnetic fields are known on the corner grid points, Maxwell's equations can be solved to calculate the new electromagnetic fields. These can then be interpolated back to the position of the particle. Letting  $W$  be the interpolation function, which is just the weight functions for a given corner of the grid cells, the communication of the charge and current density to the grid, and the communication of the fields back to the particle position can be written on the same form. For a total number of  $N_s$  macroparticles of  $s$  different particle species and a total charge  $q_s = q_p N_p$  in a cell  $i$ , the charge and current density interpolated to the points on the grid becomes

$$\rho_i = \sum_s \sum_p^{N_s} q_s W(\mathbf{x}_i - \mathbf{x}_p) \quad \mathbf{J}_i = \sum_s \sum_p^{N_s} q_s \mathbf{v}_p W(\mathbf{x}_i - \mathbf{x}_p) \quad (4.14)$$

Similarly, the electromagnetic fields acting on the particle that were calculated on the grid,  $\mathbf{E}_i$  and  $\mathbf{B}_i$ , can be interpolated to the particle position

$$\mathbf{E}_p = \sum_i \mathbf{E}_i W(\mathbf{x}_i - \mathbf{x}_p) \quad \mathbf{B}_p = \sum_i \mathbf{B}_i W(\mathbf{x}_i - \mathbf{x}_p) \quad (4.15)$$

Once the new electromagnetic fields have been calculated and interpolated to the particle position, the new particle velocity and position can be calculated according to equations 4.9. In addition to correctly setting up the grid of cells and interpolating the information back and forth between the particle positions and the grid points for every time step, what happens at the boundary of the simulation domain must be defined properly in order to ensure the simulation is stable and does not produce nonphysical results.

### Boundary conditions

The simulation domain is a limited region in space inside which the plasma processes of interest are simulated. To ensure that the real physical processes are accurately represented it is essential to have appropriate boundary conditions at the edges of the simulation domain. The boundaries can be closed, in which case the particle number is conserved, or open, which allows particles to escape the simulation domain. Depending on the simulation, appropriate source terms for particles and/or fields can be imposed on the boundaries. In the papers in this thesis, two different types of closed boundary conditions for the plasma particles have been employed: periodic and reflective. When the boundaries are periodic, particles that exit the simulation domain with a certain velocity at one boundary are inserted at the opposite boundary with the same velocity. For ex-

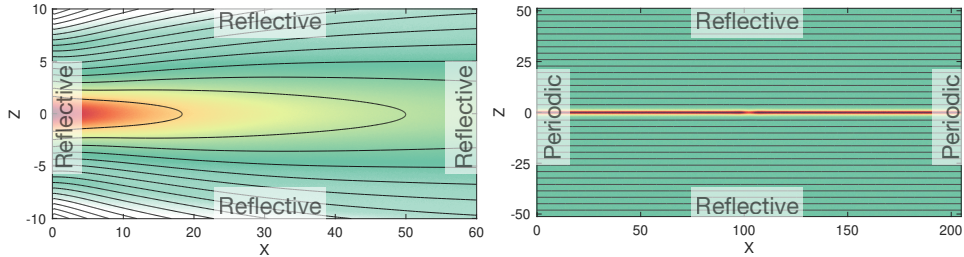


Figure 4.5: The boundary conditions used in the papers in this thesis. The left panel is for paper III, and the right panel is for papers I and II.

ample, if the particle impacts the boundary in a 2D simulation domain at  $(x_{max}, 0)$  with velocity  $v_x$ , it will be inserted at  $(x_{min}, 0)$  with the same velocity,  $v_x$ . Periodic boundary conditions are only suitable if the simulation domain is symmetric along the direction of the boundary, and also requires ghost cells at each boundary to ensure that particles are not duplicated on impact with the boundary. For reflective boundaries, particles impacting the boundary with a certain velocity are specularly reflected into the simulation domain from the same spatial coordinate with an oppositely directed velocity. In a 2D simulation domain with reflective boundaries, a particle impacting the boundary at  $(0, z_{max})$  with velocity  $v_z$  will be inserted at  $(0, z_{max})$  with velocity  $-v_z$ . Certain simulation schemes require specific boundary conditions to be able to solve the governing equations, such as simulations where the spatial derivatives are calculated using fast Fourier Transforms, which requires periodic boundaries in all directions (*Pritchett, 2003*). In other simulations, the most suitable boundary conditions can be determined by what process and plasma system is being investigated. In paper I and II, the boundary conditions at  $x_{min}$  and  $x_{max}$  are periodic, while the boundaries at  $z_{min}$  and  $z_{max}$  are reflective. In paper III, all boundaries are reflective since the simulated system was not symmetric along the  $x$ -direction. This is illustrated in figure 4.5.

For the electromagnetic fields, the boundary conditions are determined by constraints on their divergence or imposed directly by assigning the value at the boundary. The out-of-plane electric field,  $E_y$ , is defined to be zero at the boundaries to preserve the magnetic flux conservation in the simulation domain. In Paper III, the simulation is driven for a short time period by imposing  $E_y$  at the  $x_{min}, z_{min}$  and  $z_{max}$  boundaries before it is set to zero. The remaining boundary conditions are determined by  $\nabla \cdot \mathbf{B} = 0$ ,  $\nabla \times \mathbf{B} = \mu_0 \mathbf{J}$  and  $\nabla \cdot \mathbf{E} = \rho / \epsilon_0$ .



### 4.1.3 Time evolution

Advancing a PIC code in time can be a very involved process, requiring the variables to be defined at both current and intermediate time steps to accurately solve the temporal derivatives in Maxwell's equations (Pritchett, 2003). One of the most common temporal integration schemes is the time centered leapfrog scheme, which is accurate to the second order (Dawson, 1983; Eastwood, 1986; Lapenta, 2015; Pritchett, 2003). Figure 4.6 shows an illustration of the leapfrog integration scheme as it is set up in the simulations used in this thesis, where the particle velocity and the current are known at integration times, while the remaining variables are defined at an intermediate time half-way between the integration times. Other leapfrog schemes might have other variable combinations at the different times (e.g. Pritchett, 2003), but the procedure of the leapfrog scheme is still the same. The variables defined at whole time steps are calculated using variables at half time steps, and vice versa.

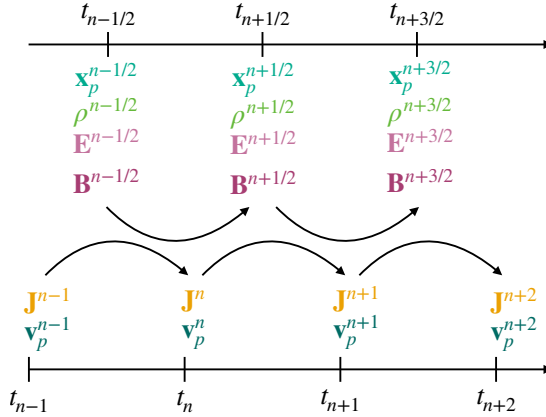


Figure 4.6: An illustration of the leapfrog integration scheme. The current and particle velocities are known at integration times, while the electromagnetic fields, particle position and charge density are known at intermediate times.

The leapfrog scheme described above is an example of an explicit integration scheme, but both the equations of motion and Maxwell's equations can be solved either explicitly or implicitly. In an explicit solver, all new variables are calculated using variables already known from previous integration times (Birdsall and Langdon, 1991; Lapenta et al., 2006; Markidis et al., 2010; Pritchett, 2003). Explicit solvers therefore follow a simple step-by-step procedure in time, but are limited by stability constraints. First, the grid spacing must satisfy the Courant-Friedrichs-Lewy condition (Courant et al., 1967), meaning that the grid size must be larger than the distance travelled by the fastest traveling wave in the simulation (Dawson, 1983; Forslund, 1985; Lapenta et al., 2006), which in our case is the speed of light,  $\Delta x > c\Delta t$ . Additionally, the grid size must be larger than the distance

the electrons travel during their oscillations around the ions,  $\Delta x > \omega_{pe} \Delta t$ . Finally, the grid size must be smaller than the Debye length,  $\Delta x < \lambda_D$  (Forsslund, 1985). The first restraint is a consequence of the discretization of the electromagnetic fields on the finite grid, while the two remaining restraints are a consequence of the discretization of the equations of motion for the particles and the interpolation between the particle position and the grid (Lapenta *et al.*, 2006). Even though the increase in computational power has made it possible to simulate many plasma systems explicitly, these restraints severely limit the applicability of explicit solvers, especially for simulations of large spatial and temporal scales (Brackbill and Forsslund, 1985; Lapenta *et al.*, 2006; Markidis *et al.*, 2010). As a way to get around this, implicit solvers were created, which remedies the stability concerns of explicit solvers at the price of making the calculations more complex.

Implicit solvers have the advantage of not being restricted in the choice of grid spacing like the explicit solvers are, and can provide accurate solutions for the evolution of the plasma for any size of the integration time step (Brackbill and Forsslund, 1985). However, they require knowledge of variables from both previous and future times in order to solve the governing equations. To calculate the new particle positions and velocity, implicit solvers require knowledge about the future electromagnetic fields, and to calculate these fields the future values of the charge and current density (Lapenta *et al.*, 2006). Consequentially, the necessary system of equations to be solved becomes non-linear, and all the particle and field equations must be solved self-consistently. The result of solving the equations implicitly is that otherwise exponentially growing, unstable wave modes are damped, and the solutions are stable for low frequency phenomena requiring a larger time step to describe efficiently (Forsslund, 1985).

The code used in this thesis utilizes both explicit and implicit integration schemes. The particle trajectories, i.e. their position and velocity, is calculated explicitly, while the electromagnetic fields are calculated implicitly. In order to advance the simulation in time, the equations of motion (equations 4.9) and Maxwell's equations must be discretized in time. For a time step  $\Delta t$ , the new particle position at  $t = n + 3/2$  and velocity at time  $t = n + 1$  can be expressed as

$$\mathbf{x}_p^{n+3/2} = \mathbf{x}_p^{n+1/2} + \mathbf{v}_p^{n+1} \Delta t \quad (4.16)$$

$$\mathbf{v}_p^{n+1} = \mathbf{v}_p^n + \frac{q_p \Delta t}{m_s} (\mathbf{E}^{n+1/2} + \mathbf{v}_p^{n+\alpha} \times \mathbf{B}^{n+1/2}) \quad (4.17)$$

where  $\alpha$  in the cyclotron part of the particle velocity denotes an intermediate calculation time. In our code,  $\alpha = 0.5$ , and the velocity at  $t = n + \alpha$  is solved by taking it as an

average between the present and future value, such that  $\mathbf{v}_p^{n+\alpha} = (1 - \alpha)\mathbf{v}_p^n + \alpha\mathbf{v}_p^{n+1}$ . Equation 4.17 then becomes

$$\mathbf{v}_p^{n+1} = \mathbf{v}_p^n + \frac{q_p \Delta t}{m_s} (\mathbf{E}^{n+1/2} + [(1 - \alpha)\mathbf{v}_p^n + \alpha\mathbf{v}_p^{n+1}] \times \mathbf{B}^{n+1/2}) \quad (4.18)$$

which can be rewritten through algebraic manipulation and using vector identities to an expression for  $\mathbf{v}_p^{n+1}$  given by the electromagnetic fields at  $t = n + 1/2$  and  $\mathbf{v}_p$  at  $t = n$

$$\mathbf{v}_p^{n+1} = \mathbf{\Phi} + \kappa [-\alpha \frac{q_p \Delta t}{m_s} (B^2 \mathbf{\Phi} - \mathbf{\Phi} \cdot \mathbf{B} \mathbf{B}) + \mathbf{\Phi} \times \mathbf{B}] \quad (4.19)$$

with

$$\mathbf{\Phi} = \mathbf{v}_p^n + \frac{q_p \Delta t}{m_s} (\mathbf{E}^{n+1/2} + (1 - \alpha)\mathbf{v}_p^n \times \mathbf{B}^{n+1/2}) \quad (4.20)$$

and

$$\kappa = \frac{\alpha \Delta t q / m}{1 + (\alpha \Delta t q / m)^2 B^2} \quad (4.21)$$

Next, Maxwell's equations must be time discretized in an appropriate way to express the implicit electromagnetic fields that are needed to advance the particles. Starting by time discretizing Ampère's and Faraday's laws, they can be expressed as

$$\mathbf{E}^{n+3/2} - \mathbf{E}^{n+1/2} = c^2 \Delta t (\phi \nabla \times \mathbf{B}^{n+3/2} + (1 - \phi) \nabla \times \mathbf{B}^{n+1/2} - \mu_0 \mathbf{J}^{n+1}) \quad (4.22)$$

$$\mathbf{B}^{n+3/2} - \mathbf{B}^{n+1/2} = -\Delta t (\phi \nabla \times \mathbf{E}^{n+3/2} + (1 - \phi) \nabla \times \mathbf{E}^{n+1/2}) \quad (4.23)$$

The  $\phi$  parameter indicates how much weight is given to the future values in the implicit integration. We have used  $\phi = 0.55$ , meaning that we give slightly more weight to the future values than the past. An expression for the magnetic field at  $t = n + 3/2$  can be found by inserting equation 4.22 into equation 4.23

$$\mathbf{B}^{n+3/2} - \mathbf{B}^{n+1/2} = -\Delta t (\phi \nabla \times (c^2 \Delta t (\phi \nabla \times \mathbf{B}^{n+3/2} + (1 - \phi) \nabla \times \mathbf{B}^{n+1/2} - \mu_0 \mathbf{J}^{n+1})) + \nabla \times \mathbf{E}^{n+1/2}) \quad (4.24)$$

This can be rewritten on a form which expresses  $\mathbf{B}$  at  $t = n + 3/2$  only from variables at earlier times, using vector identities and the fact that  $\mathbf{B}$  is divergence free

$$(1 - (c\phi\Delta t)^2\nabla^2)\mathbf{B}^{n+3/2} = \mathbf{B}^{n+1/2} + (c\Delta t)^2\phi[(1 - \phi)\mathbf{B}^{n+1/2} + \mu_0\nabla \times \mathbf{J}^{n+1}] - \Delta t\nabla \times \mathbf{E}^{n+1/2} \quad (4.25)$$

This is a second order elliptic equation for  $\mathbf{B}^{n+3/2}$  which provides the implicit magnetic field used in the explicit particle calculations. It is also used in equation 4.22 to find the corresponding implicit electric field.

The magnetic field at  $t = n + 3/2$  can be expressed as

$$\mathbf{B}^{n+3/2} = \mathbf{S} + (c\phi\Delta t)^2\nabla^2\mathbf{B}^{n+3/2} \quad (4.26)$$

where  $\mathbf{S}$  is the right hand side of equation 4.25 with  $\mathbf{B}$  and  $\mathbf{E}$  taken at  $t = n + 1/2$ , and  $\mathbf{J}$  taken at  $t = n$ . With the grid as illustrated in figure 4.4, the components of the quantity  $\mathbf{S}_{i,j}$  can be expressed as

$$\begin{aligned} S_{x_i,j}^{n+3/2} &= B_{x_i,j}^{n+1/2} + \frac{\Delta t}{\Delta z} \left[ (E_{y_{i,j+1}}^{n+1/2} - E_{y_{i,j}}^{n+1/2}) + \phi c^2 \Delta t (J_{y_{i,j+1}}^n - J_{y_{i,j}}^n) \right] \\ &+ (1 - \phi)\phi(c\Delta t)^2 \left[ \frac{B_{x_{i+1,j}}^{n+1/2} - 2B_{x_{i,j}}^{n+1/2} + B_{x_{i-1,j}}^{n+1/2}}{(\Delta x)^2} + \frac{B_{x_{i,j+1}}^{n+1/2} - 2B_{x_{i,j}}^{n+1/2} + B_{x_{i,j-1}}^{n+1/2}}{(\Delta z)^2} \right] \end{aligned}$$

$$\begin{aligned} S_{y_{i,j}}^{n+3/2} &= B_{y_{i,j}}^{n+1/2} - \Delta t \left[ \frac{E_{x_{i,j+1}}^{n+1/2} - E_{x_{i,j}}^{n+1/2}}{\Delta z} - \frac{E_{z_{i+1,j}}^{n+1/2} - E_{z_{i,j}}^{n+1/2}}{\Delta x} \right] \\ &+ \frac{\phi}{2}(c\Delta t)^2 \left[ \frac{J_{x_{i,j+1}}^n - J_{x_{i,j}}^n + J_{x_{i+1,j+1}}^n - J_{x_{i+1,j}}^n - J_{z_{i,j+1}}^n - J_{z_{i,j}}^n + J_{z_{i+1,j+1}}^n + J_{z_{i+1,j}}^n}{\Delta x} \right] \\ &+ (1 - \phi)\phi(c\Delta t)^2 \left[ \frac{B_{y_{i+1,j}}^{n+1/2} - 2B_{y_{i,j}}^{n+1/2} + B_{y_{i-1,j}}^{n+1/2}}{(\Delta x)^2} + \frac{B_{y_{i,j+1}}^{n+1/2} - 2B_{y_{i,j}}^{n+1/2} + B_{y_{i,j-1}}^{n+1/2}}{(\Delta z)^2} \right] \end{aligned}$$

$$\begin{aligned} S_{z_{i,j}}^{n+3/2} &= B_{z_{i,j}}^{n+1/2} - \frac{\Delta t}{\Delta x} \left[ (E_{y_{i+1,j}}^{n+1/2} - E_{y_{i,j}}^{n+1/2}) - \phi c^2 \Delta t (J_{y_{i+1,j}}^n + J_{y_{i,j}}^n) \right] \\ &+ (1 - \phi)\phi(c\Delta t)^2 \left[ \frac{B_{z_{i+1,j}}^{n+1/2} - 2B_{z_{i,j}}^{n+1/2} + B_{z_{i-1,j}}^{n+1/2}}{(\Delta x)^2} + \frac{B_{z_{i,j+1}}^{n+1/2} - 2B_{z_{i,j}}^{n+1/2} + B_{z_{i,j-1}}^{n+1/2}}{(\Delta z)^2} \right] \end{aligned}$$

Note that the superscripts on  $\mathbf{S}$  in the expressions above refer to the corresponding time step of  $\mathbf{B}$  in equation 4.26. The Laplacian derivatives are expressed by the finite difference approximation over the neighbouring grid points, and the currents are averaged in  $x$  and  $z$  inside the expression for  $S_y$ .

$$\mathbf{B}_{i,j} = \frac{\mathbf{S}_{i,j} + k_x(\mathbf{B}_{i+1,j} - \mathbf{B}_{i-1,j}) + k_z(\mathbf{B}_{i,j+1} - \mathbf{B}_{i,j-1})}{1 + 2k_x + 2k_z} \quad (4.27)$$

with  $k_l = (c\phi\Delta t/|\Delta l|)^2$  and  $l = [x, z]$ . Once the magnetic field is calculated, it can be used to find the implicit electric field from equation 4.22 together with the current from  $t = n + 1$ , which gives the components

$$\begin{aligned} E_{x_i,j}^{n+3/2} &= E_{x_i,j}^{n+1/2} + c^2 \Delta t \left[ \frac{-\phi(B_{y_i,j}^{n+3/2} - B_{y_i,j-1}^{n+3/2}) - (1-\phi)(B_{y_i,j}^{n+1/2} - B_{y_i,j-1}^{n+1/2})}{\Delta z} - J_{x_i,j}^{n+1} \right] \\ E_{y_i,j}^{n+3/2} &= E_{y_i,j}^{n+1/2} + c^2 \Delta t \left[ \frac{\phi(B_{x_i,j}^{n+3/2} - B_{x_i,j-1}^{n+3/2}) + (1-\phi)(B_{x_i,j}^{n+1/2} - B_{x_i,j-1}^{n+1/2})}{\Delta z} \right] \\ &\quad + c^2 \Delta t \left[ \frac{-\phi(B_{z_i,j}^{n+3/2} - B_{z_i-1,j}^{n+3/2}) - (1-\phi)(B_{z_i,j}^{n+1/2} - B_{z_i-1,j}^{n+1/2})}{\Delta x} - J_{y_i,j}^{n+1} \right] \\ E_{z_i,j}^{n+3/2} &= E_{z_i,j}^{n+1/2} + c^2 \Delta t \left[ \frac{\phi(B_{y_i,j}^{n+3/2} - B_{y_{i-1},j}^{n+3/2}) + (1-\phi)(B_{y_i,j}^{n+1/2} - B_{y_{i-1},j}^{n+1/2})}{\Delta x} - J_{z_i,j}^{n+1} \right] \end{aligned}$$

Before the particles can be advanced by the new implicit fields, we must ensure that charge conservation has been maintained. This is done with an iterative Langdon-Marder-type correction routine to the electric field (*Hesse et al.*, 1999; *Langdon*, 1992; *Marder*, 1987). When the simulation is initiated, Gauss' law is fulfilled, i.e.  $\epsilon_0 \nabla \cdot \mathbf{E} = \rho$ . The Langdon-Marder-type correction allows for the grid spacing to be nonuniform, and calculates a correction to the electric field based on Poisson's equation

$$\mathbf{E}^{n+3/2} = \mathbf{E}_0^{n+3/2} + \Delta t \nabla [d(\nabla \cdot \mathbf{E}_0^{n+3/2} - \rho^{n+3/2})] \quad (4.28)$$

where the zero indicates the uncorrected electric field from the implicit integration, and  $d$  is a numerical factor which is chosen to appropriately balance the generation and dissipation rate of the correction term at the boundaries (*Marder*, 1987).

To summarise, in one cycle of the code, the first step is to advance the particle velocities from  $t = n$  to  $t = n + 1$ , using the electromagnetic fields at  $t = n + 1/2$ . We thereafter

use the new velocities at  $t = n + 1$  to advance the particle positions from  $t = n + 1/2$  to  $t = n + 3/2$ . Finally, the new electromagnetic fields at  $t = n + 3/2$  are calculated and, the cycle repeats. This is illustrated in figure 4.7.

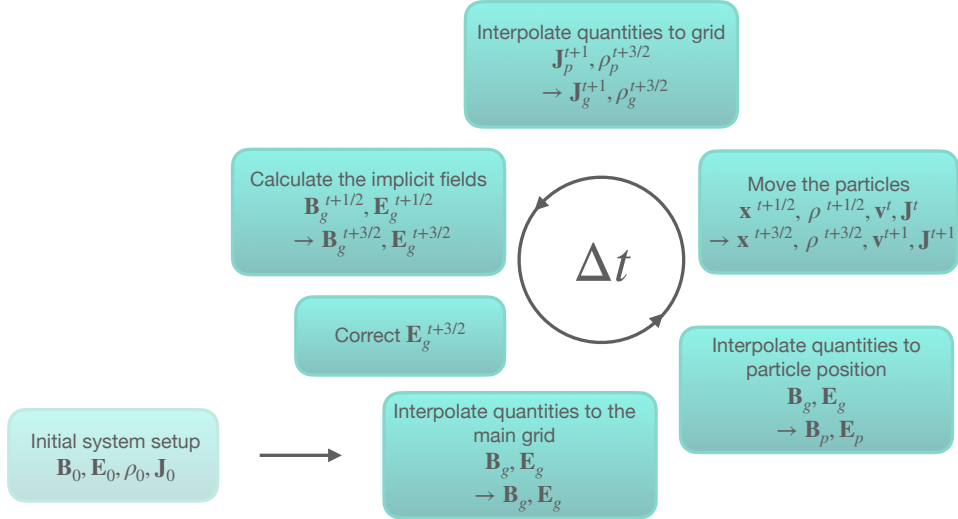


Figure 4.7: An illustration of the order in which the code solves the system of equations.

#### 4.1.4 Normalization and stability

The PIC method of solving the coupled Maxwell-Vlasov system of equations described in this chapter can be applicable for any collisionless plasma and magnetic field configuration if the system is normalized appropriately. This is done by defining all variables in a unitless fashion. In our code, we employ a Vlasov scaling which is referenced to the electrons, which we later convert to ion units in our data analysis. This is summarized in table 4.1. In the code, time is normalized to the inverse plasma frequency,  $\omega_{pe}^{-1}$ , and in the articles in this thesis we have used integration time steps of 0.5 and 1, meaning we perform the calculations every half or every whole plasma oscillation. This large time step is made possible by the implicit integration scheme for the electromagnetic fields, which allows for time steps which does not fulfill the Courant-Friedrichs-Lewy condition. Velocities are normalized to the speed of light,  $c$ , since this is the velocity of the fastest wave speed in the simulation. To ensure stability, the grid spacing should not be larger than the Debye length, and the time step should not be so large that too many particles cross more than one cell boundary per calculation. The density and the magnetic field are both normalized to their values which are determined from the initial setup of the simulation (equations 4.1 and 4.2), the density from the peak value of the Harris current

Quantity	Code	Analysis
Time	$\omega_{pe}^{-1}$	$\Omega_{ci}^{-1}$
Length	$c/\omega_{pe}$	$c/\omega_{pi}$
Density	$n_0$	$n_0$
Velocity	$c$	$v_A$
B	$\omega_{pe}/\Omega_{ce}B_0$	$B_0$
E	$c \omega_{pe}/\Omega_{ce}B_0$	$v_A B_0$
$\rho$	$en_0$	$en_0$
Current	$c en_0$	$v_A en_0$

Table 4.1: A summary of the normalizations used for the quantities needed for the calculations in our PIC code. The code is normalized to the electron units and the speed of light, which we convert to ion units and the ion Alfvén velocity in our post-processing of the data for the analysis.

sheet, and the magnetic field from its asymptotic value in the inflow far away from the current sheet. To reduce noise, there should always be at least 100 electrons per cell. The more particles per cell, the smoother the results, but it also makes the code more computationally heavy and requires more memory. To remedy this, the mass ratio of the simulation particles can be manipulated, which can later be scaled for when comparing to real observations. For the particles in this thesis we have used a mass ratio of  $m_i/m_e = 25$  for the two first articles, and  $m_i/m_e = 100$  in the last article. This means we have simulated either very heavy electrons, or very light ions, depending on which normalization scheme we look at them in. The remaining normalizations are defined by a combination of the already mentioned quantities, such as length, which is given by the ratio of the speed of light and the plasma frequency, and the electric field, which is given by the product of the velocity and the magnetic field.

By normalizing all quantities, the calculations are applicable to a variety of different plasma environments, and the same simulation can be scaled to fit different conditions. For example, one can simulate a reconnection event with symmetric inflow regions and some initial streaming velocity along the inflow magnetic fields. By inserting the proper values for the magnitude of the magnetic field and the particle velocity, results from this one simulation can be applicable to both nightside reconnection in the Earth’s magnetosphere, or to reconnection in the solar magnetic field. This is an important aspect of what makes PIC simulations and computer simulations in general a very powerful tool to both predict and to understand the underlying physics of specific observations of real reconnection events.

# Chapter 5

## Introduction to the papers

### 5.1 Paper I: The Micro-Macro Coupling of Mass-Loading in Symmetric Magnetic Reconnection with Cold Ions

In this paper, we investigate how magnetic reconnection is affected by the presence of a dense, cold ion distribution in the inflow regions. We compare two fully kinetic, 2.5D PIC simulations, one without cold ions which we refer to as the baseline run, and one including cold ions which we refer to as the cold run. In the cold run, the cold ions are initiated at a distance of  $z = \pm 4.5d_i$  away from the current sheet. This front of cold ions propagates towards the current sheet with the reconnection inflow, and eventually participates in the reconnection process. Spacecraft observations have shown that such populations of cold ions are commonly present in the magnetosphere, and might in some cases constitute the dominant particle species (*André and Cully, 2012; André et al., 2015; Fuselier et al., 2017; Walsh et al., 2014b*). Such fronts of cold ions can be the result of for example ionospheric outflow or plasmaspheric plumes. As discussed in section 3.2, the presence of cold or heavy particle species has a significant impact on characteristic temporal and spatial scales associated with the diffusion region (*Alm et al., 2019; André et al., 2016; Dargent et al., 2017, 2019; Divin et al., 2016; Toledo-Redondo et al., 2015, 2016*). We found that the cold ion population has an impact on both the reconnection rate, and the aspect ratio of the diffusion region. The reconnection rate was reduced when the cold ions participated in the reconnection process, by a factor which corresponded to the mass-loading factor,  $\sqrt{1 + n_{i*}m_{i*}/n_im_i}$ . To estimate the height and width of the ion diffusion region, we employed two different methods. The height was estimated by finding the distance at which the non-ideal contribution to the reconnection electric



field dominated over the contribution from the  $\mathbf{v} \times \mathbf{B}$ -drift. The width we estimated by finding the limit where the local gyroradius was equal to the distance from the x-point. Together, these two factors define the aspect ratio of the diffusion region, which we found to exhibit a similar reduction as the reconnection rate. This could be expected since the aspect ratio and the reconnection rate can be linked through fluid scaling arguments (*Vasyliunas, 1975*). The question was rather how the large scale reduction in the rate is coupled to the small scale reduction in the aspect ratio. We found that this coupling was facilitated through the temporal inertia of the cold ion population. The cold and warm ions exhibited a transient counter-streaming behaviour caused by the oppositely directed diamagnetic drift of the warm population and the acceleration and turning of the cold population by the Hall electric field and  $B_x$ . This produced a significant negative temporal inertia contribution to the reconnection electric field until the cold population had been heated enough to participate in the diamagnetic drift such that it became dominant. In summary, we showed that the large scale mass-loading effect on the reconnection rate by the cold ions was coupled to the small scale change in aspect ratio of the diffusion region through the cold ion dynamics in and around the ion diffusion region.

## 5.2 Paper II: Asymmetrically varying guide field during magnetic reconnection: Particle-In-Cell simulations

In this paper, we investigate how magnetic reconnection is affected by having variations in the direction of the inflow magnetic field. We compared two fully kinetic, 2.5D PIC simulations of magnetic reconnection, one with symmetric, non-varying fields which we refer to as the baseline run, and one where the magnetic field direction varied in one of the inflow regions, which we refer to as the varying run. The field variations in the varying run were initiated in bands some distance from the current sheet and they propagated inwards and eventually participated in the reconnection process. The magnetic field only changed direction in the bands, as we initiated them such that the total magnetic field magnitude was constant. Therefore, the magnetic field energy is still symmetric above and below the current sheet, but the magnetic shear angle varies between being symmetric and not. Changes in the magnetic shear angle could be caused by for example variations in the IMF, flux rope coalescence (*Akhavan-Tafti et al., 2019, 2020; Zhou et al., 2017*) and re-reconnection (*Poh et al., 2019*). As discussed in section 3.2, magnetic reconnection behaves significantly different during symmetric reconnection and asymmetric and guide

field reconnection. The magnetic shear angle has been shown to have an impact on both large and small scales, such as on the reconnection rate, the configuration of the reconnecting system, and the particle dynamics (e.g. *Goldman et al.*, 2011; *Pritchett*, 2005a; *Pritchett and Coroniti*, 2004; *Pritchett and Mozer*, 2009; *Swisdak et al.*, 2005; *Trattner et al.*, 2017).

In our paper, we wanted to investigate what would happen if the shear angle changed during active reconnection. We found that this leads to non-linear variations in the reconnection rate due to modifications of the flux transport into the reconnection site. Since only the anti-parallel component of the magnetic fields reconnect, the transport of flux into the reconnection site was higher in the bands where the magnetic field had a component into the plane. Based on the work by *Cassak and Shay* (2007), we developed a scaling factor which we used to show that the rate variations could not be explained by the asymmetry in the magnitude of the reconnecting components alone. The non-linearity of the rate variations was caused by information about the field changes being propagated in front of the actual variations. By close inspection of the contributions to the total momentum transport in the inflow regions, we found that this was made possible by the magnetic tension force, which was reduced in the bands where the magnetic field had a component into the plane. This allowed the region to expand more easily, causing the increased transport of flux ahead of the region.

We also found that the variations in the reconnection inflow have an effect on the reconnection outflow. By comparing with the baseline run, we showed that the field variations survived the reconnection process, and that the outflow became less laminar. By considering the timing of the variations in the inflow and outflow, and by comparing with the baseline run, we suggested that the transient structures in the outflow on the varying run were a result of the inflow variations, meaning that the reconnection process does not act as a filter.

### 5.3 Paper III: Electron behaviour around the onset of magnetic reconnection

In this paper we investigate how magnetic reconnection can start in an initially stable field configuration. We initiate a tail-like equilibrium configuration of the magnetic field and current (*Birn et al.*, 1975) in a fully kinetic, 2.5D PIC simulation. To establish a converging flow towards the current sheet, we employ an initial electric field driver at the boundaries which leads to magnetic field pile-up through Faraday's law. This is similar to how the solar wind loads the magnetic field in the magnetotail lobes (e.g. *Hesse et al.*,

2001a; Liu *et al.*, 2014; Pritchett, 2005b, 2010). The driver is turned off long before reconnection onset eventually takes place. By looking at the evolution of the  $z$ -directed magnetic field, we establish the last data output time before reconnection has started and investigate the electron dynamics at this time. The choice of investigation time was supported by the evolution of the necessary non-gyrotropic pressure gradients for the existence of the reconnection electric field (Hesse *et al.*, 1999, 2001a; Kuznetsova *et al.*, 1998; Vasylunas, 1975). As mentioned in section 3.2, the frozen-in condition must be broken for all particle species in the simulation at the same time for reconnection to take place. Since the electrons are most coupled to the magnetic field, signatures of the onset of reconnection should be associated with this species. By close investigation of the electron velocity distributions around the location where the  $x$ -point eventually forms, we identified non-gyrotropic signatures and signatures of acceleration that could be indicative of an imminent reconnection onset. The first signature was non-gyrotropy in the  $v_x v_y$ -plane which took the form of shifted semicircles along the  $y$ -direction, which we show originates from acceleration by the out-of-plane electric field. The shifted semicircles can be explained by looking at the history of the particle in the electric field, which exhibits a reversal at this point. Particles entering from the left and the right side of the field reversal point will experience opposite acceleration by the out-of-plane electric field, which leads to the shifted semicircles. The second signature we identified was lemon shaped distributions in the  $v_x v_z$ -plane. By following the trajectory of test-particles integrated backwards in time, we show that this is also caused by energization from the out-of-plane electric field. As the electrons gyrate around the  $x$ -directed magnetic field in the thinning current sheet, they are accelerated by this electric field when they are at the turning point in their orbit, when the velocity and the electric field are mostly parallel. These two signatures in the electron velocity distributions, together with a thinning current sheet could be observable by the Magnetospheric Multiscale (MMS) satellites (Burch *et al.*, 2016; Pollock *et al.*, 2016), a satellite mission specifically designed by NASA to study the small scale dynamics of magnetic reconnection. If we could identify current sheets which are about to reconnect, we could expand our data pool of conditions which are favourable for reconnection, which might help answering why some thin current sheets reconnect while others do not.

# Chapter 6

## Conclusions and Future Prospects

### 6.1 Conclusions

The research conducted in this thesis is a part of a larger effort to understand why, how, when and where magnetic reconnection occurs. To answer these questions, we must understand how magnetic reconnection behaves under ideal conditions, and how the reconnection process is affected by variations in the surrounding plasma and electromagnetic field configuration. We must also understand which conditions are favorable for reconnection to occur, and which conditions can lead to reconnection shutting down or not initiating at all. The aim of this thesis has been to add some pieces to the collective puzzle of information needed to answer these questions.

We have found that the reconnection process is affected by transient variations in the inflow region. The reconnection rate was reduced when changes in the inflow conditions impacted the reconnection region and participated in the process. We showed this for a front of cold ions in paper I, and for variations in the magnetic field direction in paper II. In paper I, we looked at both large and small scale processes, and established how these were coupled to each other. On large scales we found that the reconnection rate was reduced by mass-loading, and this reduction was shown to be consistent with a reduction in the aspect ratio of the ion diffusion region, which is a small scale effect. We showed that the temporal inertia of the cold ions was the mediating factor between the large scale reduction in the rate and the small scale reduction of the diffusion region. The temporal inertia contribution was shown to be a transient factor, but the impact it had on the reconnection rate and the structure of the reconnection site persisted. In paper II, we showed that the transient variations in the inflow magnetic field direction had a significant influence on both the large and small scale dynamics of the reconnecting sys-

tem, both directly and indirectly. Variations in the reconnection rate, the flux transport and the structure of the exhaust resulting from the changes in the direction of the inflow magnetic field were identified, and the correlation between them was discussed. We established that the reconnection process does not act as a filter for variations in the inflow region, which means that the conditions in the outflow can be a result of the structure of the inflow instead of processes in the diffusion region. The results of these two papers could aid our understanding of what might make magnetic reconnection stop after it has initiated. Finally, if reconnection is to be influenced by transient variations in its inflow conditions, it must initiate in the first place. The question of what conditions are necessary for magnetic reconnection to occur is not yet fully understood. Our last paper aimed to contribute to understanding why some current sheets reconnect while others do not. In paper III, we found signatures in the electron phase space distribution functions of a current sheet which later reconnected that might be indicative of an imminent reconnection onset. We identified two distinct signatures which should be present simultaneously in thinning current sheets to indicate reconnection onset. If this can be used to identify current sheets that are close to or at reconnection onset, our results may help to expand our pool of observational data of reconnecting current sheets. This could lead to a greater understanding of why some current sheets reconnect while others do not, which would take us one step closer to understanding how and why reconnection occurs at all.

## 6.2 Future prospects

The research conducted as part of this thesis employed fully kinetic, 2.5D PIC simulations. With this, we can simulate the particle and field dynamics in very high detail, but due to the computational cost of having such a fine grid, the simulation region is fairly small. A natural next step to create a fuller picture would be to employ an embedded PIC simulation scheme, where the small scales close to the x-point is modeled using PIC inside a global fluid model. This would allow us to model both the small scale dynamics of the diffusion region and the global fluid behaviour of for example the magnetotail simultaneously. Such embedded PIC simulation frameworks have already proven to be a useful tool in situations where the complete picture can only be understood when processes on different scales are considered together. For example, the MHD-EPIC part of the Space Weather Modeling Framework has an embedded PIC scheme which couples to the large scale models (*Chen et al.*, 2020; *Tóth et al.*, 2005, 2012).

Simulations are a great tool for analyzing and understanding the physics of an event. However, without being contextualized by real observations we cannot know that the

---

conclusions we draw from them are realized in nature. Regarding all the research done in this thesis, it would be beneficial to look for evidence of our predictions and conclusions in real spacecraft data. The MMS mission is specially designed to study the small scale dynamics of reconnection in our magnetosphere, and is therefore well suited to collect the data necessary to compare with our simulations. Additionally, performing a conjunction study with simultaneous observations in both the inflow and outflow of a reconnection event would allow us to study what information is transferred between the regions. This would require additional spacecraft to MMS, since their high resolution data requires them to be in a closed tetrahedron formation. A possibility could for example be to have observations by MMS in conjunction with some other spacecraft observatory such as ESA's Cluster II or NASA's THEMIS observatories in the different regions. Alternatively, a new mission could be designed where multiple spacecraft organized in several tetrahedron formations could fly together to make high resolution observations at multiple scales at once.



# Bibliography

- Akhavan-Tafti, M., J. A. Slavin, J. P. Eastwood, P. A. Cassak, and D. J. Gershman (2019), MMS Multi-Point Analysis of FTE Evolution: Physical Characteristics and Dynamics, *Journal of Geophysical Research: Space Physics*, *124*(7), 5376–5395, doi:10.1029/2018JA026311.
- Akhavan-Tafti, M., M. Palmroth, J. A. Slavin, M. Battarbee, U. Ganse, M. Grandin, G. Le, D. J. Gershman, J. P. Eastwood, and J. E. Stawarz (2020), Comparative Analysis of the Vlasiator Simulations and MMS Observations of Multiple X-Line Reconnection and Flux Transfer Events, *Journal of Geophysical Research: Space Physics*, *125*(7), doi:10.1029/2019JA027410.
- Alfvén, H. (1942), Existence of Electromagnetic-Hydrodynamic Waves, *Nature*, *150*, 405–406, doi:10.1038/150405d0.
- Alm, L., M. André, D. B. Graham, Y. V. Khotyaintsev, A. Vaivads, C. R. Chappell, J. Dargent, S. A. Fuselier, S. Haaland, B. Lavraud, W. Li, P. Tenfjord, S. Toledo-Redondo, and S. K. Vines (2019), MMS Observations of Multiscale Hall Physics in the Magnetotail, *Geophysical Research Letters*, *46*(17-18), 10,230–10,239, doi:10.1029/2019GL084137.
- André, M., and C. M. Cully (2012), Low-energy ions: A previously hidden solar system particle population, *Geophysical Research Letters*, *39*(3), 1–7, doi:10.1029/2011GL050242.
- André, M., K. Li, and A. I. Eriksson (2015), Outflow of low-energy ions and the solar cycle, *Journal of Geophysical Research: Space Physics*, *120*(2), 1072–1085, doi:10.1002/2014JA020714.
- André, M., W. Li, S. Toledo-Redondo, Y. V. Khotyaintsev, A. Vaivads, D. B. Graham, C. Norgren, J. Burch, P. A. Lindqvist, G. Marklund, R. Ergun, R. Torbert, W. Magnes, C. T. Russell, B. Giles, T. E. Moore, M. O. Chandler, C. Pollock, D. T. Young, L. A. Avanov, J. C. Dorelli, D. J. Gershman, W. R. Paterson, B. Lavraud, and Y. Saito (2016), Magnetic reconnection and modification of the Hall physics due to cold ions



- at the magnetopause, *Geophysical Research Letters*, *43*(13), 6705–6712, doi:10.1002/2016GL069665.
- Angelopoulos, V., J. P. McFadden, D. Larson, C. W. Carlson, S. B. Mende, H. Frey, T. Phan, D. G. Sibeck, K.-H. Glassmeier, U. Auster, E. Donovan, I. R. Mann, I. J. Rae, C. T. Russell, A. Runov, X.-z. Zhou, and L. Kepko (2008), Tail Reconnection Triggering Substorm Onset, *Science*, *321*(5891), 931–935, doi:10.1126/science.1160495.
- Angelopoulos, V., A. Artemyev, T. D. Phan, and Y. Miyashita (2020), Near-Earth magnetotail reconnection powers space storms, *Nature Physics*, *16*(3), 317–321, doi:10.1038/s41567-019-0749-4.
- Baumjohann, W., and R. A. Treumann (2012), *Basic Space Plasma Physics - Revised Edition*, Imperial College Press, London.
- Beidler, M. T., and P. A. Cassak (2011), Model for incomplete reconnection in sawtooth crashes, *Physical Review Letters*, *107*(25), 1–5, doi:10.1103/PhysRevLett.107.255002.
- Birdsall, C., and A. B. Langdon (1991), *Plasma physics via computer simulation*, IOP Publishing, Bristol.
- Birn, J., R. Sommer, and K. Schindler (1975), Open and closed magnetospheric tail configurations and their stability, *Astrophysics and Space Science*, *35*, 389–402.
- Birn, J., J. F. Drake, M. A. Shay, B. N. Rogers, R. E. Denton, M. Hesse, M. Kuznetsova, Z. W. Ma, A. Bhattacharjee, A. Otto, and P. L. Pritchett (2001), Geospace Environmental Modeling (GEM) Magnetic Reconnection Challenge, *Journal of Geophysical Research: Space Physics*, *106*(A3), 3715–3719, doi:10.1029/1999ja900449.
- Birn, J., J. E. Borovsky, and M. Hesse (2008), Properties of asymmetric magnetic reconnection, *Physics of Plasmas*, *15*(3), doi:10.1063/1.2888491.
- Brackbill, J., and D. Forslund (1985), Simulation of Low-Frequency, Electromagnetic Phenomena in Plasmas, in *Multiple Time Scales*, edited by J. U. Brackbill and B. Cohen, pp. 271–310, ACADEMIC PRESS, INC., London, doi:10.1016/b978-0-12-123420-1.50014-8.
- Büchner, J., C. Dum, and M. Scholer (2003), *Space Plasma Simulation*, Springer Berlin Heidelberg, Heidelberg, doi:10.1007/3-540-36530-3\_15.
- Burch, J. L., T. E. Moore, R. B. Torbert, and B. L. Giles (2016), Magnetospheric Multiscale Overview and Science Objectives, doi:10.1007/s11214-015-0164-9.
- Cai, H. J., and L. C. Lee (1997), The generalized Ohm’s law in collisionless magnetic reconnection, *Physics of Plasmas*, *4*(3), 509–520, doi:10.1063/1.872178.

- Cassak, P. A., and M. A. Shay (2007), Scaling of asymmetric magnetic reconnection: General theory and collisional simulations, *Physics of Plasmas*, *14*(10), doi:10.1063/1.2795630.
- Cassak, P. A., Y. H. Liu, and M. A. Shay (2017), A review of the 0.1 reconnection rate problem, doi:10.1017/S0022377817000666.
- Chen, Y., G. Tóth, H. Hietala, S. K. Vines, Y. Zou, Y. Nishimura, M. V. D. Silveira, Z. Guo, Y. Lin, and S. Markidis (2020), Magnetohydrodynamic With Embedded Particle-In-Cell Simulation of the Geospace Environment Modeling Dayside Kinetic Processes Challenge Event, *Earth and Space Science*, *7*(11), doi:10.1029/2020EA001331.
- Comisso, L., and F. A. Asenjo (2021), Magnetic reconnection as a mechanism for energy extraction from rotating black holes, *Physical Review D*, *103*(2), 23,014, doi:10.1103/PhysRevD.103.023014.
- Comisso, L., and A. Bhattacharjee (2016), On the value of the reconnection rate, *Journal of Plasma Physics*, *82*(6), 1–9, doi:10.1017/S002237781600101X.
- Courant, R., K. Friedrichs, and H. Lewy (1967), On the Partial Difference Equations of Mathematical Physics, *IBM Journal of Research and Development*, *11*(2), 215–234, doi:10.1147/rd.112.0215.
- Dargent, J., N. Aunai, B. Lavraud, S. Toledo-Redondo, M. A. Shay, P. A. Cassak, and K. Malakit (2017), Kinetic simulation of asymmetric magnetic reconnection with cold ions, *Journal of Geophysical Research: Space Physics*, *122*(5), 5290–5306, doi:10.1002/2016JA023831.
- Dargent, J., N. Aunai, B. Lavraud, S. Toledo-Redondo, and F. Califano (2019), Signatures of Cold Ions in a Kinetic Simulation of the Reconnecting Magnetopause, *Journal of Geophysical Research: Space Physics*, *124*(4), 2018JA026,343, doi:10.1029/2018JA026343.
- Dargent, J., N. Aunai, B. Lavraud, S. Toledo-Redondo, and F. Califano (2020), Simulation of Plasmaspheric Plume Impact on Dayside Magnetic Reconnection, *Geophysical Research Letters*, *47*(4), doi:10.1029/2019GL086546.
- Dawson, J. M. (1983), Particle simulation of plasmas, *Reviews of Modern Physics*, *55*(2), 403–447, doi:10.1103/RevModPhys.55.403.
- de Boor, C. (1978), *A Practical Guide to Splines*, vol. 27, Springer Verlag, New York.
- Dessler, A. J. (1968), Magnetic merging in the magnetospheric tail, *Journal of Geophysical Research*, *73*(1), 209–214, doi:10.1029/ja073i001p00209.

- Dessler, A. J. (1971), Vacuum merging: A possible source of the magnetospheric cross-tail electric field, *Journal of Geophysical Research*, *76*(13), 3174–3176, doi:10.1029/ja076i013p03174.
- Divin, A., Y. V. Khotyaintsev, A. Vaivads, M. André, S. Toledo-Redondo, S. Markidis, and G. Lapenta (2016), Three-scale structure of diffusion region in the presence of cold ions, *Journal of Geophysical Research: Space Physics*, *121*(12), 12,001–12,013, doi:10.1002/2016JA023606.
- Dungey, J. W. (1961), Interplanetary magnetic field and the auroral zones, *Physical Review Letters*, *6*(2), 47–48, doi:10.1103/PhysRevLett.6.47.
- Dupree, T. H. (1963), Kinetic theory of plasma and the electromagnetic field, *Physics of Fluids*, *6*(12), 1714–1729, doi:10.1063/1.1711014.
- Eastwood, J. P., T. D. Phan, M. Øieroset, and M. A. Shay (2010), Average properties of the magnetic reconnection ion diffusion region in the Earth’s magnetotail: The 2001–2005 Cluster observations and comparison with simulations, *Journal of Geophysical Research: Space Physics*, *115*(8), 1–13, doi:10.1029/2009JA014962.
- Eastwood, J. P., T. D. Phan, M. Øieroset, M. A. Shay, K. Malakit, M. Swisdak, J. F. Drake, and A. Masters (2013), Influence of asymmetries and guide fields on the magnetic reconnection diffusion region in collisionless space plasmas, *Plasma Physics and Controlled Fusion*, *55*(12), doi:10.1088/0741-3335/55/12/124001.
- Eastwood, J. W. (1986), Particle simulation methods in plasma physics, *Computer Physics Communications*, *43*(1), 89–106, doi:10.1016/0010-4655(86)90055-X.
- Ergun, R. E., K. A. Goodrich, F. D. Wilder, N. Ahmadi, J. C. Holmes, S. Eriksson, J. E. Stawarz, R. Nakamura, K. J. Genestreti, M. Hesse, J. L. Burch, R. B. Torbert, T. D. Phan, S. J. Schwartz, J. P. Eastwood, R. J. Strangeway, O. Le Contel, C. T. Russell, M. R. Argall, P. A. Lindqvist, L. J. Chen, P. A. Cassak, B. L. Giles, J. C. Dorelli, D. Gershman, T. W. Leonard, B. Lavraud, A. Retino, W. Matthaeus, and A. Vaivads (2018), Magnetic Reconnection, Turbulence, and Particle Acceleration: Observations in the Earth’s Magnetotail, *Geophysical Research Letters*, *45*(8), 3338–3347, doi:10.1002/2018GL076993.
- Forslund, D. W. (1985), Fundamentals of plasma simulation, *Space Science Reviews*, *42*(1-2), 3–16, doi:10.1007/BF00218219.
- Fuselier, S. A., and W. S. Lewis (2011), Properties of near-earth magnetic reconnection from in-situ observations, *Space Science Reviews*, *160*(1-4), 95–121, doi:10.1007/s11214-011-9820-x.

- Fuselier, S. A., S. M. Petrinec, and K. J. Trattner (2010), Antiparallel magnetic reconnection rates at the Earth's magnetopause, *Journal of Geophysical Research: Space Physics*, *115*(10), 1–11, doi:10.1029/2010JA015302.
- Fuselier, S. A., K. J. Trattner, and S. M. Petrinec (2011), Antiparallel and component reconnection at the dayside magnetopause, *Journal of Geophysical Research: Space Physics*, *116*(10), 1–14, doi:10.1029/2011JA016888.
- Fuselier, S. A., J. L. Burch, J. Mukherjee, K. J. Genestreti, S. K. Vines, R. Gomez, J. Goldstein, K. J. Trattner, S. M. Petrinec, B. Lavraud, and R. J. Strangeway (2017), Magnetospheric ion influence at the dayside magnetopause, *Journal of Geophysical Research: Space Physics*, *122*(8), 8617–8631, doi:10.1002/2017JA024515.
- Fuselier, S. A., K. J. Trattner, S. M. Petrinec, M. H. Denton, S. Toledo-Redondo, M. André, N. Aunai, C. R. Chappell, A. Glocer, S. E. Haaland, M. Hesse, L. M. Kistler, B. Lavraud, W. Li, T. E. Moore, D. Graham, L. Alm, P. Tenfjord, J. Dargent, S. K. Vines, K. Nykyri, J. L. Burch, and R. J. Strangeway (2019), Mass Loading the Earth's Dayside Magnetopause Boundary Layer and Its Effect on Magnetic Reconnection, *Geophysical Research Letters*, *46*(12), 6204–6213, doi:10.1029/2019GL082384.
- Giovanelli, R. (1947), Magnetic and Electric Phenomena in the Sun's Atmosphere Associated with Sunspots, *Monthly Notices of the Royal Astronomical Society*, *107*(4), 338–355.
- Goldman, M. V., G. Lapenta, D. L. Newman, S. Markidis, and H. Che (2011), Jet deflection by very weak guide fields during magnetic reconnection, *Physical Review Letters*, *107*(13), 2–5, doi:10.1103/PhysRevLett.107.135001.
- Gonzalez, W. D., E. N. Parker, F. S. Mozer, V. M. Vasyliūnas, P. L. Pritchett, H. Karimabadi, P. A. Cassak, J. D. Scudder, M. Yamada, R. M. Kulsrud, and D. Koga (2016), *Fundamental Concepts Associated with Magnetic Reconnection*, 1–32 pp., doi:10.1007/978-3-319-26432-5\_1.
- Harris, E. G. (1962), On a plasma sheath separating regions of oppositely directed magnetic field, *Il Nuovo Cimento Series 10*, *23*(1), 115–121, doi:10.1007/BF02733547.
- Hesse, M., and K. Schindler (1988), A theoretical foundation of general magnetic reconnection, *Journal of Geophysical Research*, *93*(A6), 5559, doi:10.1029/ja093ia06p05559.
- Hesse, M., and K. Schindler (2001), The onset of magnetic reconnection in the magnetotail, *Earth, Planets and Space*, *53*(6), 645–653, doi:10.1186/BF03353284.
- Hesse, M., and D. Winske (1993), Hybrid Simulations of Collisionless Ion Tearing, *Geophysical Research Letters*, *20*(12), 1207–1210, doi:10.1029/93GL01250.

- Hesse, M., K. Schindler, J. Birn, and M. Kuznetsova (1999), The diffusion region in collisionless magnetic reconnection, *Physics of Plasmas*, *6*(5), 1781–1795, doi:10.1063/1.873436.
- Hesse, M., M. Kuznetsova, and J. Birn (2001a), Particle-in-cell simulations of three-dimensional collisionless magnetic reconnection, *Journal of Geophysical Research*, *106*.
- Hesse, M., J. Birn, and M. Kuznetsova (2001b), Collisionless magnetic reconnection: Electron processes and transport modeling, *Journal of Geophysical Research: Space Physics*, *106*, 3721–3735.
- Hesse, M., M. Kuznetsova, and J. Birn (2004), The role of electron heat flux in guide-field magnetic reconnection, *Physics of Plasmas*, *11*(12), 5387–5397, doi:10.1063/1.1795991.
- Hesse, M., T. Neukirch, K. Schindler, M. Kuznetsova, and S. Zenitani (2011), The diffusion region in collisionless magnetic reconnection, *Space Science Reviews*, *160*(1–4), 3–23, doi:10.1007/s11214-010-9740-1.
- Hesse, M., N. Aunai, D. Sibeck, and J. Birn (2014), On the electron diffusion region in planar, asymmetric, systems, *Geophysical Research Letters*, *41*(24), 8673–8680, doi:10.1002/2014GL061586.
- Hesse, M., Y. H. Liu, L. J. Chen, N. Bessho, S. Wang, J. L. Burch, T. Moretto, C. Norgren, K. J. Genestreti, T. D. Phan, and P. Tenfjord (2018), The physical foundation of the reconnection electric field, *Physics of Plasmas*, *25*, doi:10.1063/1.5021461.
- Hesse, M., C. Norgren, P. Tenfjord, J. L. Burch, Y. H. Liu, N. Bessho, L. J. Chen, S. Wang, H. Kolstø, S. F. Spinnangr, R. E. Ergun, T. Moretto, and N. K. Kwagala (2021), A New Look at the Electron Diffusion Region in Asymmetric Magnetic Reconnection, *Journal of Geophysical Research: Space Physics*, *126*(2), 1–16, doi:10.1029/2020JA028456.
- Huba, J. D. (2005), Hall magnetic reconnection: Guide field dependence, *Physics of Plasmas*, *12*(1), 1–6, doi:10.1063/1.1834592.
- Kolstø, H., M. Hesse, C. Norgren, P. Tenfjord, S. F. Spinnangr, N. K. Kwagala (2020a), Collisionless Magnetic Reconnection in an Asymmetric Oxygen Density Configuration, *Geophysical Research Letters*, *47*(1), doi:10.1029/2019GL085359.
- Kolstø, H., M. Hesse, C. Norgren, P. Tenfjord, S. F. Spinnangr, N. K. Kwagala (2020b), On the Impact of a Streaming Oxygen Population on Collisionless Magnetic Reconnection, *Geophysical Research Letters*, *47*(22), doi:10.1029/2020GL089462.

- Kulsrud, R. M. (2001), Magnetic reconnection: Sweet-Parker versus Petschek, *Earth, Planets and Space*, *53*(6), 417–422, doi:10.1186/BF03353251.
- Kuznetsova, M. M., M. Hesse, and D. Winske (1998), Kinetic quasi-viscous and bulk flow inertia effects in collisionless magnetotail reconnection, *Journal of Geophysical Research: Space Physics*, *103*(A1), 199–213, doi:10.1029/97ja02699.
- Langdon, A. B. (1992), On enforcing Gauss' law in electromagnetic particle-in-cell codes, *Computer Physics Communications*, *70*(3), 447–450, doi:10.1016/0010-4655(92)90105-8.
- Lapenta, G. (2015), Kinetic Plasma Simulation: Particle In Cell Method, in *XII Carolus Magnus Summer School on Plasma and Fusion Energy Physics*, August, pp. 76–85, doi:10.13140/RG.2.1.3319.2801.
- Lapenta, G., J. U. Brackbill, and P. Ricci (2006), Kinetic approach to microscopic-macroscopic coupling in space and laboratory plasmas, *Physics of Plasmas*, *13*(5), doi:10.1063/1.2173623.
- Liu, Y. H., and M. Hesse (2016), Suppression of collisionless magnetic reconnection in asymmetric current sheets, *Physics of Plasmas*, *23*(6), doi:10.1063/1.4954818.
- Liu, Y. H., J. Birn, W. Daughton, M. Hesse, and K. Schindler (2014), Onset of reconnection in the near magnetotail: PIC simulations, *Journal of Geophysical Research: Space Physics*, *119*(12), 9773–9789, doi:10.1002/2014JA020492.
- Liu, Y. H., M. Hesse, F. Guo, W. Daughton, H. Li, P. A. Cassak, and M. A. Shay (2017), Why does Steady-State Magnetic Reconnection have a Maximum Local Rate of Order 0.1?, *Physical Review Letters*, *118*(8), 1–6, doi:10.1103/PhysRevLett.118.085101.
- Lyutikov, M. (2003), Explosive reconnection in magnetars, *Monthly Notices of the Royal Astronomical Society*, *346*(2), 540–554, doi:10.1046/j.1365-2966.2003.07110.x.
- M. Øieroset, T. D. Phan, M. Fujimoto, R. P. Lin, and R. P. Lepping (2001), In situ detection of reconnection in the Earth's magnetotail, *Nature*, *412*(July), 414.
- Maheshwari, K., T. D. Phan, M. Øieroset, N. Fargette, B. Lavraud, J. L. Burch, R. J. Strangeway, D. J. Gershman, and B. L. Giles (2022), Investigation of the Diamagnetic Drift Condition for the Suppression of Magnetic Reconnection in 3D Interlinked Reconnection Events with Magnetic Flux Pileup, *The Astrophysical Journal*, *940*(2), doi:10.3847/1538-4357/ac9405.
- Marder, B. (1987), A method for incorporating Gauss' law into electromagnetic PIC codes, *Journal of Computational Physics*, *68*(1), 48–55, doi:10.1016/0021-9991(87)90043-X.

- Markidis, S., G. Lapenta, and Rizwan-uddin (2010), Multi-scale simulations of plasma with iPIC3D, *Mathematics and Computers in Simulation*, *80*(7), 1509–1519, doi:10.1016/j.matcom.2009.08.038.
- Masuda, S., T. Kosugi, H. Hara, S. Tsuneta, and Y. Ogawara (1994), A loop-top hard X-ray source in a compact solar flare as evidence for magnetic reconnection, *Nature*, *371*(6497), 495–497, doi:10.1038/371495a0.
- Mozer, F. S., and A. Retinò (2007), Quantitative estimates of magnetic field reconnection properties from electric and magnetic field measurements, *Journal of Geophysical Research: Space Physics*, *112*(10), 1–11, doi:10.1029/2007JA012406.
- Mozer, F. S., P. L. Pritchett, J. Bonnell, D. Sundkvist, and M. T. Chang (2008), Observations and simulations of asymmetric magnetic field reconnection, *Journal of Geophysical Research: Space Physics*, *113*, doi:10.1029/2008ja013535.
- Computer History Museum (n.d.), Timeline of Computer History, Retrieved 09 Feb 2023 from <https://www.computerhistory.org/timeline/computers/>.
- Parker, E. N. (1957), Sweet’s mechanism for merging magnetic fields in conducting fluids, *Journal of Geophysical Research*, *62*(4), 509–520, doi:10.1029/jz062i004p00509.
- Paschmann, G., B. U. Sonnerup, I. Papamastorakis, N. Sckopke, G. Haerendel, S. J. Bame, J. R. Asbridge, J. T. Gosling, C. T. Russell, and R. C. Elphic (1979), Plasma acceleration at the Earth’s magnetopause: Evidence for reconnection, *Nature*, *282*(5736), 243–246, doi:10.1038/282243a0.
- Petschek, H. (1964), Magnetic Field Annihilation, *The Physics of Solar Flares*, *50*, 425–439.
- Piddington, J. H. (1960), Magnetic Field Annihilation, *Geomagnetic Storm Theory*, *65*, 93–106, doi:10.1029/jz065i001p00093.
- Poh, G., J. A. Slavin, S. Lu, G. Le, D. S. Ozturk, W. J. Sun, S. Zou, J. P. Eastwood, R. Nakamura, W. Baumjohann, C. T. Russell, D. J. Gershman, B. L. Giles, C. J. Pollock, T. E. Moore, R. B. Torbert, and J. L. Burch (2019), Dissipation of Earthward Propagating Flux Rope Through Re-reconnection with Geomagnetic Field: An MMS Case Study, *Journal of Geophysical Research: Space Physics*, *124*(9), 7477–7493, doi:10.1029/2018JA026451.
- Pollock, C., T. Moore, A. Jacques, J. Burch, U. Gliese, Y. Saito, T. Omoto, L. Avanov, A. Barrie, V. Coffey, J. Dorelli, D. Gershman, B. Giles, T. Rosnack, C. Salo, S. Yokota, M. Adrian, C. Aoustin, C. Auletta, S. Aung, V. Bigio, N. Cao, M. Chandler, D. Chornay, K. Christian, G. Clark, G. Collinson, T. Corris, A. De Los Santos, R. Devlin,

- T. Diaz, T. Dickerson, C. Dickson, A. Diekmann, F. Diggs, C. Duncan, A. Figueroa-Vinas, C. Firman, M. Freeman, N. Galassi, K. Garcia, G. Goodhart, D. Guererro, J. Hageman, J. Hanley, E. Hemminger, M. Holland, M. Hutchins, T. James, W. Jones, S. Kreisler, J. Kujawski, V. Lavu, J. Lobell, E. LeCompte, A. Lukemire, E. MacDonald, A. Mariano, T. Mukai, K. Narayanan, Q. Nguyen, M. Onizuka, W. Paterson, S. Persyn, B. Piepgrass, F. Cheney, A. Rager, T. Raghuram, A. Ramil, L. Reichen-thal, H. Rodriguez, J. Rouzaud, A. Rucker, Y. Saito, M. Samara, J. A. Sauvaud, D. Schuster, M. Shappirio, K. Shelton, D. Sher, D. Smith, K. Smith, S. Smith, D. Steinfeld, R. Szymkiewicz, K. Tanimoto, J. Taylor, C. Tucker, K. Tull, A. Uhl, J. Vloet, P. Walpole, S. Weidner, D. White, G. Winkert, P. S. Yeh, and M. Zeuch (2016), Fast Plasma Investigation for Magnetospheric Multiscale, *Space Science Reviews*, 199(1-4), 331–406, doi:10.1007/s11214-016-0245-4.
- Pritchett, P. L. (2001), Geospace Environment Modeling magnetic reconnection challenge: Simulations with a full particle electromagnetic code, *Journal of Geophysical Research: Space Physics*, 106(A3), 3783–3798, doi:10.1029/1999ja001006.
- Pritchett, P. L. (2003), Particle-in-Cell Simulation of Plasmas— A Tutorial, in *Space Plasma Simulation*, edited by J. Büchner, C. Dum, and M. Scholer, pp. 1–24, Springer Berlin Heidelberg, Berlin, Heidelberg, doi:10.1007/3-540-36530-3\_1.
- Pritchett, P. L. (2005a), Onset and saturation of guide-field magnetic reconnection, *Physics of Plasmas*, 12(6), 1–11, doi:10.1063/1.1914309.
- Pritchett, P. L. (2005b), Externally driven magnetic reconnection in the presence of a normal magnetic field, *Journal of Geophysical Research: Space Physics*, 110(A5), doi:10.1029/2004JA010948.
- Pritchett, P. L. (2008), Collisionless magnetic reconnection in an asymmetric current sheet, *Journal of Geophysical Research: Space Physics*, 113, 1–14, doi:10.1029/2007JA012930.
- Pritchett, P. L. (2010), Onset of magnetic reconnection in the presence of a normal magnetic field: Realistic ion to electron mass ratio, *Journal of Geophysical Research: Space Physics*, 115(10), 1–9, doi:10.1029/2010JA015371.
- Pritchett, P. L., and F. V. Coroniti (2004), Three-dimensional collisionless magnetic reconnection in the presence of a guide field, *Journal of Geophysical Research: Space Physics*, 109(A1), doi:10.1029/2003JA009999.
- Pritchett, P. L., and F. S. Mozer (2009), Asymmetric magnetic reconnection in the presence of a guide field, *Journal of Geophysical Research: Space Physics*, 114(11), 1–14, doi:10.1029/2009JA014343.



- Ricci, P., J. U. Brackbill, W. Daughton, and G. Lapenta (2004), Collisionless magnetic reconnection in the presence of a guide field, *Physics of Plasmas*, 11(8), 4102–4114, doi:10.1063/1.1768552.
- Ripperda, B., M. Liska, K. Chatterjee, G. Musoke, A. A. Philippov, S. B. Markoff, A. Tchekhovskoy, and Z. Younsi (2022), Black Hole Flares: Ejection of Accreted Magnetic Flux through 3D Plasmoid-mediated Reconnection, *The Astrophysical Journal Letters*, 924(2), L32, doi:10.3847/2041-8213/ac46a1.
- Shalaby, M., A. E. Broderick, P. Chang, C. Pfrommer, A. Lamberts, and E. Puchwein (2017), SHARP: A Spatially Higher-order, Relativistic Particle-in-cell Code, *The Astrophysical Journal*, 841(1), 52, doi:10.3847/1538-4357/aa6d13.
- Shay, M. A., J. F. Drake, R. E. Denton, and D. Biskamp (1998), Structure of the dissipation region during collisionless magnetic reconnection, *Journal of Geophysical Research: Space Physics*, 103(A5), 9165–9176, doi:10.1029/97ja03528.
- Shay, M. A., J. F. Drake, B. N. Rogers, and R. E. Denton (1999), The scaling of collisionless, magnetic reconnection for large systems, *Geophysical Research Letters*, 26(14), 2163–2166, doi:10.1029/1999GL900481.
- Shibata, K., and T. Magara (2011), Solar flares: Magnetohydrodynamic processes, *Living Reviews in Solar Physics*, 8, doi:10.12942/lrsp-2011-6.
- Sigma2/NRIS (2023), Betzy, Retrieved 09 Feb 2023 from [https://documentation.sigma2.no/hpc\\_machines/betzy.html](https://documentation.sigma2.no/hpc_machines/betzy.html).
- Sironi, L., M. Petropoulou, and D. Giannios (2015), Relativistic jets shine through shocks or magnetic reconnection?, *Monthly Notices of the Royal Astronomical Society*, 450(1), 183–191, doi:10.1093/mnras/stv641.
- Spinnangr, S. F., P. Tenfjord, M. Hesse, C. Norgren, H. M. Kolstø, N. K. Kwagala, T. M. Jørgensen, and J. Pérez-Coll Jiménez (2021a), Asymmetrically Varying Guide Field During Magnetic Reconnection: Particle-In-Cell Simulations, *Journal of Geophysical Research: Space Physics*, 127(1), doi:10.1029/2021JA029955.
- Spinnangr, S. F., M. Hesse, P. Tenfjord, C. Norgren, H. M. Kolstø, N. K. Kwagala, and T. M. Jørgensen (2021b), The Micro-Macro Coupling of Mass-Loading in Symmetric Magnetic Reconnection With Cold Ions, *Geophysical Research Letters*, 48(13), 1–9, doi:10.1029/2020GL090690.
- Spinnangr, S. F., M. Hesse, P. Tenfjord, C. Norgren, H. M. Kolstø, N. K. Kwagala, T. M. Jørgensen, and T. Phan (2022), Electron Behavior Around the Onset of Magnetic Reconnection, *Geophysical Research Letters*, 49(23), doi:10.1029/2022GL102209.

- Su, Y. J., J. E. Borovsky, M. F. Thomsen, R. C. Elphic, and D. J. McComas (2000), Plasmaspheric material at the reconnecting magnetopause, *Journal of Geophysical Research: Space Physics*, *105*(A4), 7591–7600, doi:10.1029/1999ja000266.
- Sweet, P. A. (1958), The Neutral Point Theory of Solar Flares, *Symposium - International Astronomical Union*, *6*, 123–134, doi:10.1017/S0074180900237704.
- Swisdak, M., B. N. Rogers, J. F. Drake, and M. A. Shay (2003), Diamagnetic suppression of component magnetic reconnection at the magnetopause, *Journal of Geophysical Research: Space Physics*, *108*(A5), 1–10, doi:10.1029/2002JA009726.
- Swisdak, M., J. F. Drake, M. A. Shay, and J. G. McIlhargey (2005), Transition from antiparallel to component magnetic reconnection, *Journal of Geophysical Research: Space Physics*, *110*(A5), 1–11, doi:10.1029/2004JA010748.
- Tenfjord, P., M. Hesse, and C. Norgren (2018), The Formation of an Oxygen Wave by Magnetic Reconnection, *Journal of Geophysical Research: Space Physics*, *123*(11), 9370–9380, doi:10.1029/2018JA026026.
- Tenfjord, P., M. Hesse, C. Norgren, S. F. Spinnangr, and H. Kolstø (2019), The Impact of Oxygen on the Reconnection Rate, *Geophysical Research Letters*, *46*(12), 6195–6203, doi:10.1029/2019GL082175.
- Tenfjord, P., M. Hesse, C. Norgren, S. F. Spinnangr, H. Kolstø, and N. Kwagala (2020), Interaction of Cold Streaming Protons with the Reconnection Process, *Journal of Geophysical Research: Space Physics*, *125*(6), doi:10.1029/2019JA027619.
- Toledo-Redondo, S., A. Vaivads, M. André, and Y. V. Khotyaintsev (2015), Modification of the Hall physics in magnetic reconnection due to cold ions at the Earth’s magnetopause, *Geophysical Research Letters*, *42*(15), 6146–6154, doi:10.1002/2015GL065129.
- Toledo-Redondo, S., M. André, Y. V. Khotyaintsev, A. Vaivads, A. Walsh, W. Li, D. B. Graham, B. Lavraud, A. Masson, N. Aunai, A. Divin, J. Dargent, S. Fuselier, D. J. Gershman, J. Dorelli, B. Giles, L. Avanov, C. Pollock, Y. Saito, T. E. Moore, V. Coffey, M. O. Chandler, P. A. Lindqvist, R. Torbert, and C. T. Russell (2016), Cold ion demagnetization near the X-line of magnetic reconnection, *Geophysical Research Letters*, *43*(13), 6759–6767, doi:10.1002/2016GL069877.
- Toledo-Redondo, S., M. André, N. Aunai, C. R. Chappell, J. Dargent, S. A. Fuselier, A. Glocer, D. B. Graham, S. Haaland, M. Hesse, L. M. Kistler, B. Lavraud, W. Li, T. E. Moore, P. Tenfjord, and S. K. Vines (2021), Impacts of Ionospheric Ions on Magnetic Reconnection and Earth’s Magnetosphere Dynamics, *Reviews of Geophysics*, *59*(3), doi:10.1029/2020rg000707.

- Tóth, G., I. V. Sokolov, T. I. Gombosi, D. R. Chesney, C. R. Clauer, D. L. De Zeeuw, K. C. Hansen, K. J. Kane, W. B. Manchester, R. C. Oehmke, K. G. Powell, A. J. Ridley, I. I. Roussev, Q. F. Stout, O. Volberg, R. A. Wolf, S. Sazykin, A. Chan, B. Yu, and J. Kóta (2005), Space weather modeling framework: A new tool for the space science community, *Journal of Geophysical Research: Space Physics*, 110(A12), 1–21, doi:10.1029/2005JA011126.
- Tóth, G., B. van der Holst, I. V. Sokolov, D. L. De Zeeuw, T. I. Gombosi, F. Fang, W. B. Manchester, X. Meng, D. Najib, K. G. Powell, Q. F. Stout, A. Glocer, Y. J. Ma, and M. Merav (2012), Adaptive numerical algorithms in space weather modeling, *Journal of Computational Physics*, 231(3), 870–903, doi:10.1016/j.jcp.2011.02.006.
- Trattner, K. J., J. S. Mulcock, S. M. Petrinec, and S. A. Fuselier (2007), Probing the boundary between antiparallel and component reconnection during southward interplanetary magnetic field conditions, *Journal of Geophysical Research: Space Physics*, 112(8), 1–16, doi:10.1029/2007JA012270.
- Trattner, K. J., J. L. Burch, R. Ergun, S. Eriksson, S. A. Fuselier, B. L. Giles, R. G. Gomez, E. W. Grimes, W. S. Lewis, B. Mauk, S. M. Petrinec, C. T. Russell, R. J. Strangeway, L. Trenchi, and F. D. Wilder (2017), The MMS Dayside Magnetic Reconnection Locations During Phase 1 and Their Relation to the Predictions of the Maximum Magnetic Shear Model, *Journal of Geophysical Research: Space Physics*, 122(12), 11,991–12,005, doi:10.1002/2017JA024488.
- Treumann, R. A., and W. Baumjohann (1997), *Advanced Space Plasma Physics*, Imperial College Press, London, doi:10.1142/p020.
- University of Michigan Climate and Space Sciences and Engineering (2023), Space Weather Modeling Framework (SWMF), Retrieved 10 Feb 2023 from <https://clasp.engin.umich.edu/research/theory-computational-methods/space-weather-modeling-framework/>.
- Vasyliunas, V. M. (1975), Theoretical models of magnetic field line merging, *Reviews of Geophysics*, 13(1), 303–336, doi:10.1029/RG013i001p00303.
- Vasyliūnas, V. M. (2011), Physics of magnetospheric variability, *Space Science Reviews*, 158(1), 91–118, doi:10.1007/s11214-010-9696-1.
- Walsh, B. M., D. G. Sibeck, Y. Nishimura, and V. Angelopoulos (2013), Statistical analysis of the plasmaspheric plume at the magnetopause, *Journal of Geophysical Research: Space Physics*, 118(8), 4844–4851, doi:10.1002/jgra.50458.

- Walsh, B. M., T. D. Phan, D. G. Sibeck, and V. M. Souza (2014a), The plasmaspheric plume and magnetopause reconnection, *Geophysical Research Letters*, *41*(2), 223–228, doi:10.1002/2013GL058802.
- Walsh, B. M., J. C. Foster, P. J. Erickson, and D. G. Sibeck (2014b), Simultaneous ground- And space-based observations of the plasmaspheric plume and reconnection, *Science*, *343*(6175), 1122–1125, doi:10.1126/science.1247212.
- Wang, S., L. M. Kistler, C. G. Mouikis, and S. M. Petrinec (2015), Dependence of the dayside magnetopause reconnection rate on local conditions, *Journal of Geophysical Research*, *120*, 6386–6408, doi:10.1002/2015JA021524.
- Weiss, L., P. H. Reiff, J. Moses, R. A. Heelis, and B. Moore (1992), Energy Dissipation in Substorms, *ESA, Substorms 1*, pp. 309–317.
- Yamada, M., R. Kulsrud, and H. Ji (2010), Magnetic reconnection, *Reviews of Modern Physics*, *82*(1), 603–664, doi:10.1103/RevModPhys.82.603.
- Zhou, M., J. Berchem, R. J. Walker, M. El-Alaoui, X. Deng, E. Cazzola, G. Lapenta, M. L. Goldstein, W. R. Paterson, Y. Pang, R. E. Ergun, B. Lavraud, H. Liang, C. T. Russell, R. J. Strangeway, C. Zhao, B. L. Giles, C. J. Pollock, P. A. Lindqvist, G. Marklund, F. D. Wilder, Y. V. Khotyaintsev, R. B. Torbert, and J. L. Burch (2017), Coalescence of Macroscopic Flux Ropes at the Subsolar Magnetopause: Magnetospheric Multiscale Observations, *Physical Review Letters*, *119*(5), 1–6, doi: 10.1103/PhysRevLett.119.055101.
- Zweibel, E. G., and M. Yamada (2009), Magnetic reconnection in astrophysical and laboratory plasmas, *Annual Review of Astronomy and Astrophysics*, *47*, 291–332, doi: 10.1146/annurev-astro-082708-101726.



# Chapter 7

## Scientific results



# Paper I

## **The Micro-Macro Coupling of Mass-Loading in Symmetric Magnetic Reconnection with Cold Ions**

S.F. Spinnangr, M. Hesse, P. Tenfjord, C. Norgren, H.M. Kolstø, N. Kwagala, T.M. Jørgensen

*Geophysical Research Letters*, Vol. 48, Issue 13 doi:10.1029/2020GL090690, 2021





# Geophysical Research Letters



## RESEARCH LETTER

10.1029/2020GL090690

### Key Points:

- Cold ions in the inflow region affect reconnection on both micro- and macro-scales
- The micro-macro coupling of mass-loading is mediated by the cold ion inertia
- Cold and warm ions are counter streaming close to the ion diffusion region boundary

### Correspondence to:








S. F. Spinnangr,  
[susanne.spinnangr@uib.no](mailto:susanne.spinnangr@uib.no)

### Citation:

Spinnangr, S. F., Hesse, M., Tenfjord, P., Norgren, C., Kolsto, H. M., Kwagala, N. K., & Jørgensen, T. M. (2021). The micro-macro coupling of mass-loading in symmetric magnetic reconnection with cold ions. *Geophysical Research Letters*, 48, e2020GL090690. <https://doi.org/10.1029/2020GL090690>

Received 4 SEP 2020  
 Accepted 14 JUN 2021

## The Micro-Macro Coupling of Mass-Loading in Symmetric Magnetic Reconnection With Cold Ions

Susanne F. Spinnangr<sup>1</sup> , Michael Hesse<sup>2</sup> , Paul Tenfjord<sup>1</sup> , Cecilia Norgren<sup>1</sup> , Håkon M. Kolstø<sup>1</sup> , Norah K. Kwagala<sup>1</sup> , and Therese M. Jørgensen<sup>2</sup> 

<sup>1</sup>Space Plasma Physics Group, University of Bergen, Bergen, Norway, <sup>2</sup>NASA Ames Research Center, Mountain View, CA, USA

**Abstract** We investigate how magnetic reconnection is influenced by an inflow of a dense cold ion population. We compare two 2.5D Particle-In-Cell simulations, one containing the cold population and one without. We find that the cold population influences the reconnection process on both global and kinetic scales, and that the dominant contribution can be explained through mass-loading. We provide an analysis of how these multiscale changes are related through kinetic processes in the ion diffusion region, the so-called micro-macro coupling of mass-loading. The inertia of the cold ion population is found to be the significant link that connects the changes on different scales. The cold and warm populations exhibit counter streaming behavior when and after the ion diffusion region reorganizes itself in response to the arrival of the cold population. This signature of the cold population should be observable by spacecraft observatories such as MMS.

**Plain Language Summary** We investigate how magnetic reconnection is influenced by a dense inflow of cold ions. We find that the cold ions influence the reconnection process on both large and small scales, and that these are connected through the cold ion inertia. We also see cold and warm ions moving in opposite directions close to the reconnection site, which should be observable by spacecraft observatories.

## 1. Introduction

Magnetic reconnection is a process where energy stored in magnetic fields gets converted into kinetic and thermal energy in the plasma, caused by a macroscopic change in the magnetic topology. It occurs in plasma environments in space, such as the Sun and the magnetosphere, as well as in plasma laboratories and fusion reactors on Earth (Yamada et al., 2010). In a plasma, the magnetic field is closely coupled to the dynamics of the plasma particles. How the magnetic reconnection process evolves is therefore highly influenced by the constituents of the plasma in the inflow regions. Spacecraft observations in the magnetosphere show, that in addition to the warm plasma populations that form current sheets in magnetic field reversal regions, populations of cold ions of ionospheric origin are commonly present, and might even constitute the dominant particle species in the system (André & Cully, 2012; André, Li, & Eriksson, 2015; Fuselier, Burch, Mukherjee, et al., 2017; Walsh et al., 2014). Usually, the thermal energies of the warm plasma populations are in the range of a few hundred eV to several keV, while the cold populations typically have energies of a few eV (André, Li, Toledo-Redondo, et al., 2016), although cold ions of larger energy ranges as well as of different densities and origins have been observed in various regions of the magnetosphere (Fuselier, Burch, Cassak, et al., 2016; Fuselier, Burch, Mukherjee, et al., 2017). Multiple previous studies and observations have shown that the presence of additional plasma populations has an impact on characteristic temporal and spatial scales associated with the diffusion region (Alm et al., 2019; André, Li, Toledo-Redondo, et al., 2016; Dargent, Aunai, Lavraud, Toledo-Redondo, & Califano, 2019; Dargent, Aunai, Lavraud, Toledo-Redondo, Shay, et al., 2017; Divin et al., 2016; Toledo-Redondo, André, et al., 2016; Toledo-Redondo, Vaivads, et al., 2015). These scales include the Larmor radius,  $r_{Ls} = \frac{m_s v_{Ts}}{q_s B}$ ,

where  $v_{Ts}$  is the perpendicular velocity of the particle. As a gyrating particle with smaller Larmor radius will remain frozen in for a longer time when approaching the X-point, multiple diffusion regions exist for the different particle populations. Such multiscale diffusion regions (more than two layers) have become a common feature in both Particle-In-Cell (PIC) simulations and observations (e.g., Alm et al. 2019; André, Li, Toledo-Redondo,

© 2021. The Authors.

This is an open access article under the terms of the [Creative Commons Attribution License](https://creativecommons.org/licenses/by/4.0/), which permits use, distribution and reproduction in any medium, provided the original work is properly cited.

et al., 2016; Dargent, Aunai, Lavraud, Toledo-Redondo, & Califano, 2020; Divin et al. 2016; Toledo-Redondo, André, et al., 2016; Toledo-Redondo, Vaivads, et al., 2015). One of the questions that remain unresolved regarding magnetic reconnection is how it stops. Since multiple plasma species have been shown to influence important features of the reconnection process, such as the reconnection rate and the Hall physics (Alm et al., 2019; André, Li, Toledo-Redondo, et al., 2016; Tenfjord, Hesse, & Norgren, 2018), understanding how reconnection responds to different inflow conditions will aid in answering this question. In this study we investigate how mass-loading the inflow regions with a large cold ion population modifies the evolution of the magnetic reconnection process. On macro-scales we expect to see a reduction in the reconnection rate, which will slow the reconnection process down. However, how this couples to the micro-scale dynamics in the diffusion region is not understood. We show that the inertia of the newly arriving cold ions play a vital role in mediating the changes on different scales. Signatures of this interaction that can be observable with spacecraft observatories such as the Magnetospheric Multiscale Mission (MMS) are briefly discussed.

We describe the simulations used for this study in Section 2. In Section 3, we describe the macro-scale effects of cold ion mass-loading on the reconnection rate. In Sections 4 and 5, we take a closer look at how this is related to the micro-scale dynamics of the ion diffusion region, and in Section 6 we summarize and discuss implications of our results.

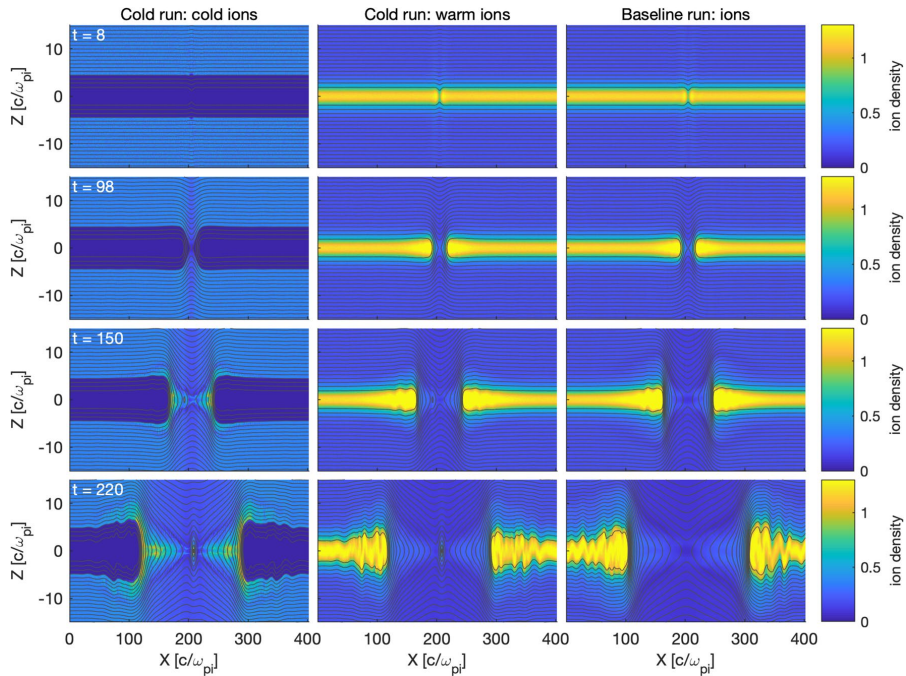
## 2. Simulation Setup

In this study we compare two 2.5D PIC simulations, both corresponding to a symmetric tail reconnection event with no guide field. Our code is a parallelized evolution of the one described in (Hesse, Schindler, et al., 1999). The first simulation contains only warm plasma, which we call the baseline run. Similar setups have previously been used to model a variety of different reconnection problems (e.g., Hesse, Birn, & Kuznetsova, 2001; Tenfjord, Hesse, & Norgren, 2018; Tenfjord, Hesse, Norgren, Spinnangr, & Kolstø, 2019). In another simulation we call the cold run, we add a population of cold ions to the baseline setup,  $4.5d_i$  outside of the current sheet. Lengths are normalized to the ion inertial length,  $d_i = \frac{c}{\omega_{pi}}$ , where  $\omega_{pi} \left( = \sqrt{\frac{4\pi n_0 e^2}{m_i}} \right)$ ,  $m_i$  = ion mass,  $e$  = elementary charge) is the ion plasma frequency and  $c$  is the speed of light. Densities are normalized to the Harris current sheet density,  $n_0$ , and velocities are normalized to the ion Alfvén velocity. Our initial magnetic field and current sheet configurations are 2-D Harris type configurations, with magnetic field  $B_x = B_0 \tanh\left(\frac{z}{\lambda}\right)$ , where  $\lambda = 2d_i$  is the halfwidth of the current layer, and with an additional localized perturbation creating an X-point. Additionally, a uniform density distribution of 0.2 of warm ions is added to the whole simulation domain. Time is normalized to the inverse ion cyclotron frequency,  $\Omega_i^{-1} = \frac{m_i}{eB_0}$ , and we employ a time step of  $\omega_{pe}\delta t = 0.5 \left( \omega_{pe} = \omega_{pi} \sqrt{\frac{m_i}{m_e}} \right)$ . A total of  $9.6 \times 10^9$  macroparticles are used, with mass ratio  $\frac{m_i}{m_e} = 25$ . For the upper and lower boundary conditions we employ specular reflection, while the left and right boundary conditions are periodic at  $x = x_{\min}$  and  $x = x_{\max}$ . The out-of-plane electric field is set to zero in order to ensure flux conservation in the simulation domain. The size of the simulation domain is  $410 \times 50 d_i$ , divided into a grid of  $6,400 \times 1,600$  cells. In the cold run, a uniform density distribution of 0.4 of cold ions is added to the inflow at  $|z| \geq 4.5$ . The initial temperature of the cold populations is set to zero. In Figure 1 we show an overview of the evolution of the two runs. The cold ions arrive at the reconnection site at time = 98, which corresponds to the time of peak reconnection rate in the cold run.

## 3. The Reconnection Rate

The reconnection rate is a measure of the speed at which the magnetic flux changes on large-scale, defined as

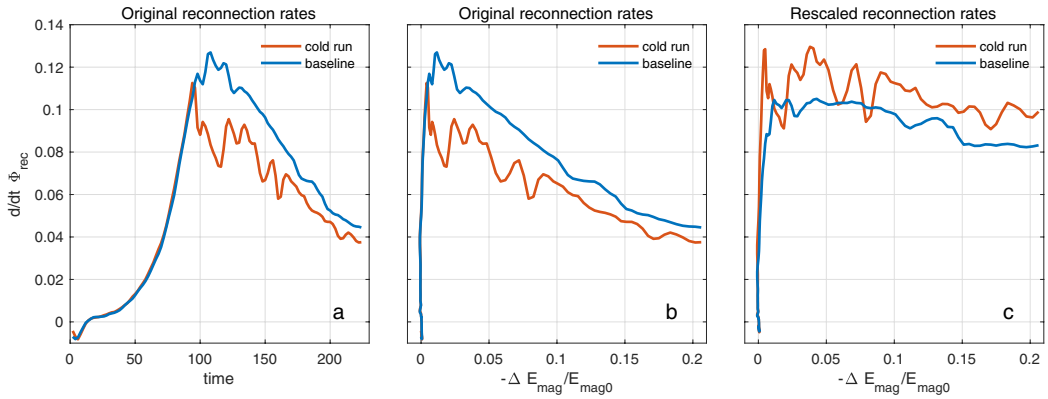
$$\frac{d}{dt} \Phi_{rec} = \frac{d}{dt} \int \vec{B} \cdot \vec{n} dA = \frac{d}{dt} \int B_z dx \quad (1)$$



**Figure 1.** Time evolution of the ion density and the in-plane magnetic field contours in the two runs. (Left) Cold and (middle) warm ion density in the cold run. (Right) Total ion density in the baseline run. By comparing the x-position of the dipolarization front in the middle and right columns we see that the cold run is reconnecting slightly slower than the baseline run.

where  $\Phi_{\text{rec}}$  is the reconnected flux,  $\vec{B}$  is the magnetic field, and  $\vec{n}$  is the normal vector of the reference surface.

Figure 2 shows the reconnection rate of both the cold and baseline run, plotted as a function of time and the fractional reduction of magnetic energy density in the system. As expected, since the cold run is mass-loaded, it shows a significantly reduced rate compared to the baseline when the cold ions become involved at time = 98. The presence of cold ions in the inflow region makes the flux tubes more inert and slows down the reconnection process. When comparing the two runs it is therefore more appropriate to compare them when they are at the same stage of the evolution, meaning when they have converted the same amount of magnetic energy, rather than at the same point in time. This is plotted Figure 2b. Figure 2c shows the reconnection rates rescaled for the effect of mass-loading. The reconnection electric field is expected to scale with the factor  $B_x V_A$  (Cassak et al., 2017; Comisso & Bhattacharjee, 2016; Liu et al., 2017), with both  $B_x$  and  $V_A$  measured in the inflow region in close vicinity to the diffusion region. When we mass-load the inflow region we effectively reduce the Alfvén velocity. By dividing the reconnection rate by this scaling factor, we should therefore remove the effect of mass-loading on the rate. The values for the magnetic field and density needed to calculate this scaling factor are averaged over  $|z| = 4 d_i \pm 1 d_i$  above and below the X-point. We find the average again of the two values calculated above and below the current sheet. These double-averaged values become the final values used in the scaling factor. Averaging in this way reduces the effect of grid size fluctuations in the ion density. Both the baseline and the cold run have been rescaled in the same way to account for the changes in magnetic flux and density inflow as the reconnection process evolves. Figure 2c shows that the reconnection rates of the two runs are comparable after rescaling. The cold run ends up with a slightly higher rate than the baseline run because the mass-loading scaling assumes the cold ions are distributed homogeneously in the system. Since we only insert them outside  $|z| \geq 4.5 d_i$ , the initial current sheet



**Figure 2.** (a) Original reconnection rate of both runs as a function of time and (b) the fractional change in magnetic energy density. (c) Both reconnection rates after they have been rescaled to account for mass-loading.

is less inert than the scaling assumes, which results in a slightly higher rate. Nevertheless, we can conclude that the decrease in the reconnection rate in the cold run is dominated by the mass-loading effect. This is consistent with similar studies, such as (Dargent, Aunai, Lavraud, Toledo-Redondo, & Califano, 2020; Divin et al., 2016; Tenfjord, Hesse, Norgren, Spinnangr, Kolstø, & Kwagala, 2020). Based on a Sweet-Parker analysis of magnetic reconnection, we can set the outflow velocity of the plasma particles to the Alfvén velocity,

$$v_{out}^2 = v_A^2 = \frac{B^2}{\mu_0 \rho} \quad (2)$$

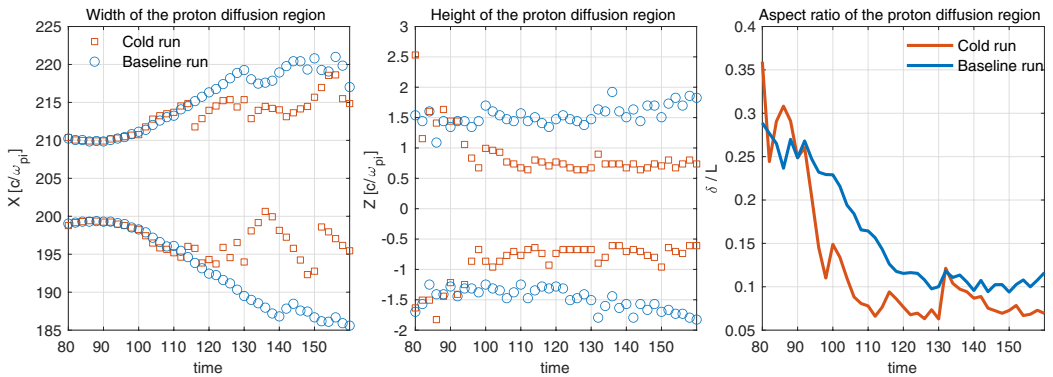
where  $\rho$  is the incoming mass density on both sides of the diffusion region, and  $B$  is the magnetic field at the same location (Vasyliunas, 1975). From mass conservation it follows that the mass flow into the diffusion region must equal the outflow. Defining the height and width of the diffusion region as  $\delta$  and  $L$  respectively, and assuming incompressible flow ( $\nabla \cdot \mathbf{v} = 0$ ), steady-state mass conservation reveals the following well established relation between the aspect ratio of the diffusion region and the flow velocities

$$\frac{\delta}{L} \sim \frac{v_{in}}{v_{out}} = \frac{v_{in}}{v_A} \quad (3)$$

The velocity ratio in this equation is another common expression for the reconnection rate (Vasyliunas, 1975). Hence, when the reconnection rate is reduced by mass-loading, the aspect ratio of the diffusion region must experience a similar reduction if the mass flow is incompressible. The reconnection rate is often referred to as a macro-scale feature of the reconnection process, since it is a large-scale effect. The aspect ratio of the diffusion region is on kinetic scales, and its reduction is therefore a micro-scale effect. How these micro- and macro-scale effects are coupled is a long-standing question in magnetic reconnection which we will try to shed some light on in the following sections where we take a closer look at the ion diffusion region.

#### 4. Scale Change of the Ion Diffusion Region

When the reconnection process evolves, the cold ion population will be energized and both the cold and the warm ions will participate. Earlier studies have shown that multiple plasma species partition the diffusion region, where the cold ion diffusion region lies between that of the warm ions and the electrons (Alm et al., 2019; André, Li, Toledo-Redondo, et al., 2016; Dargent, Aunai, Lavraud, Toledo-Redondo, & Califano, 2019; Divin et al., 2016; Toledo-Redondo, André, et al., 2016). However, researching the scaling



**Figure 3.** The height, width and aspect ratio of the total ion diffusion region for both runs. The baseline run continues expanding in both the inflow and outflow direction through the full time interval. In the cold run, the expansion in the width is reduced, along with a clear reduction in the height as the cold ions reach the reconnection site.

of the reconnection rate with the effect of mass-loading should involve the total ion population. Like in fluid models, the aspect ratio of the ion diffusion region is expected to scale with the reconnection rate also in kinetic plasmas. In this analysis, we therefore choose to treat the combination of the two ion species to find effective ion diffusion region dimensions as that region transitions from being fully dominated by the warm ion species to being influenced by the cold species. We only care about the dynamics of this combined ion aspect ratio, not its actual size, and we therefore use simple methods that give an estimate of the dimensions. In the inflow direction, we have defined the limit where the non-ideal terms in Ohm's law for the reconnection electric (Equation 6) field become dominant as a proxy for the diffusion region height. We identify the point above and below the X-point where  $v_e B_x = 0.5E_y$ , which defines the limit where  $E_y$  goes from being dominated by the frozen in  $v \times B$  drift to being mostly diffusive. In the outflow direction the dynamics are more complicated, and we therefore employ a different method. There we have defined the limit where the local thermal ion Larmor radius becomes equal to the distance from the X-point as a proxy for the diffusion region width (Divin et al., 2016). This is similar to comparing the bounce width of the ions with the distance from the X-point.

Figure 3 shows the diffusion region width ( $L$ ), height ( $\delta$ ), and aspect ratio ( $\delta/L$ ), all plotted around the time interval where the cold ions arrive at the reconnection site. There is some noise in the estimation of the diffusion region width in the cold run, caused by a high rate of island production, which can affect the calculation of the local Larmor radius. In order to avoid as much interference from islands as possible, the locations in this figure are therefore selected manually. In this way, we have made sure that the chosen locations are as close to the real boundary of the diffusion region width as possible, and not just an artificial boundary caused by an island moving through the diffusion region. However, the noise is still significant enough that we only look at the overall behavior through the full time interval. The baseline behaves as expected, with gradually increasing width of the diffusion region as reconnection proceeds. In Figure 3 we see that when the cold ions start to get involved around time = 96, the diffusion region height experiences a reduction of about 50%. We also see a reduction in the expansion rate of the width at a later time. The net effect of the cold ions on the diffusion region can be seen in the aspect ratio. Figure 3 shows that the aspect ratio is significantly reduced during the time interval when the cold ions arrive before it stabilizes slightly below  $\delta/L = 0.1$ . A similar reduction and stabilization is also present in the baseline run due to the expansion in the outflow direction. However, since the baseline does not experience any reduction in the diffusion region height, the drop is slower and less dramatic. In both runs, the stabilization around  $\delta/L = 0.1$  coincides with the stabilization of the rescaled reconnection rate around the same value (not shown). This value for the reconnection rate has been shown to be common between a variety of different reconnecting systems (Cassak et al., 2017; Comisso & Bhattacharjee, 2016; Liu et al., 2017).

To investigate the changes on micro-scales further, we take a closer look at the reconnection electric field,  $E_y$ , which at the X-line is directly proportional to the reconnection rate. If we assume that the ions are frozen in at the edges of the diffusion region, and that  $E_y$  is the same at both the inflow and outflow edge, we obtain the following relation:

$$v_{in} B_x = v_{out} B_z \quad (4)$$

We use  $\nabla \cdot \mathbf{B} = 0$  and Equation 3 to rewrite this in an explicit form for the electric field:

$$E_y \sim v_A B_z \sim v_A B_x \frac{\delta}{L} \quad (5)$$

This directly relates the reconnection electric field, that is, the reconnection rate, to the the Alfvén velocity and the aspect ratio of the diffusion region, which are both affected by mass-loading. In the following section, we will investigate how micro-scale processes in the ion diffusion region caused by the inflow of dense, cold plasma leads to a reduction in  $E_y$ , and thereby a macro-scale reduction in the reconnection rate.

### 5. Role of Cold Ion Inertia

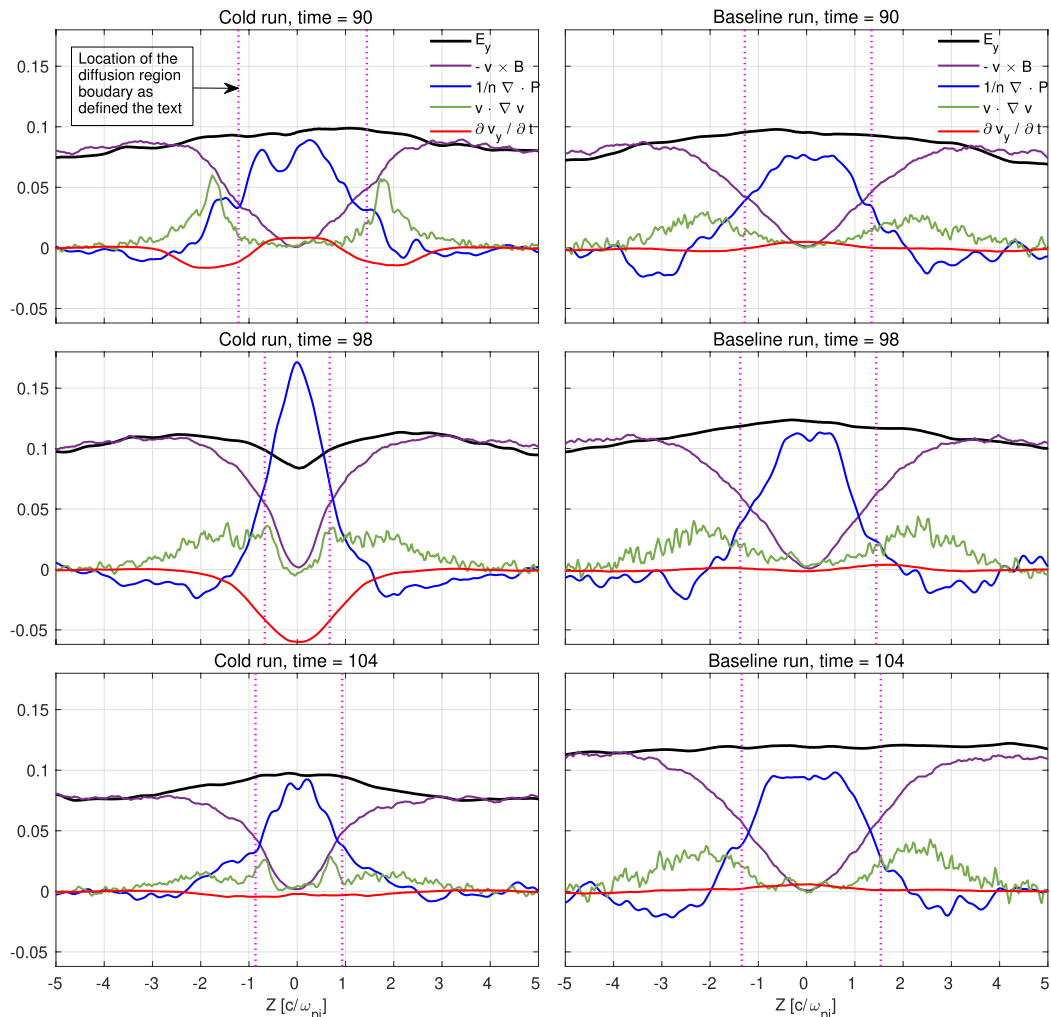
In order to investigate how  $E_y$  is being reduced as the cold ions arrive, we take a closer look at all the contributing terms as a function of  $z$  through the X-point. We express  $E_y$  through the generalized Ohm's law

$$E_y = \left( -\bar{v} \times \bar{B} + \frac{1}{qn} \nabla \cdot \mathbf{P} + \frac{m}{q} \left( \bar{v} \cdot \nabla \bar{v} + \frac{\partial \bar{v}}{\partial t} \right) \right)_y \quad (6)$$

The first term on the right hand side of this equation describes the frozen in motion, the second term describes the contribution from the divergence of the pressure, and the third and fourth term describe the contribution from the convective and temporal inertia respectively. In Figure 4, this is plotted for both the cold and baseline run for different points in time. For time = 90, the cold ions have not yet arrived at the reconnection site. At time = 98, the incoming cold fronts are just meeting at the X-point, while at time = 104 the cold population contributes about one third of the total density at the X-point. By comparing the cold run and the baseline run, we see a significant contribution from the temporal inertia when the cold ions are involved, which is not present in the baseline run. We also see that this contribution disappears at time = 104, and the two runs become more similar. The reconnection electric field is reduced by this inertia contribution during the transition when the cold ions go from not being involved to being fully involved in the reconnection process. During this transition period the reconnection process reorganizes itself on a kinetic level to incorporate the effects of the incoming additional mass density. In order to investigate how this happens, we take a closer look at the dynamics of the cold ions as they enter the diffusion region.

In Figure 5, we have plotted the density and the  $y$ -component of the velocity in the cold run for the total, warm and cold ion population as a function of  $z$  through the X-point. We show this for the same, and two additional intermediate, points in time as we investigated in Figure 4. During the same time interval where the negative inertia contribution to the reconnection electric field is significant, Figure 5 shows that the cold ions have a negative  $v_y$ , while the warm ions have a positive  $v_y$ . Comparing the changes in these velocities we see that the reduction of the total ion velocity causing the negative inertia contribution to  $E_y$  is due to the cold ions. When the cold ions approach the X-point, the system has already been reconnecting with the warm plasma for some time, and the Hall electric field has been established. The cold ions move toward the X-point like two density fronts and they are accelerated by the Hall-field. They are then turned by  $B_x$  and gain a negative  $v_y$ , which has a significant effect on the total ion  $v_y$  in the diffusion region.

Later, when a large enough fraction of the cold population has had the time to demagnetize and participate in the bouncing motion between the opposite  $B_x$  regions, they have established a large enough pressure gradient in the  $z$ -direction to exhibit diamagnetic drift. This drift is in the positive  $v_y$  direction, and does eventually become dominant. In



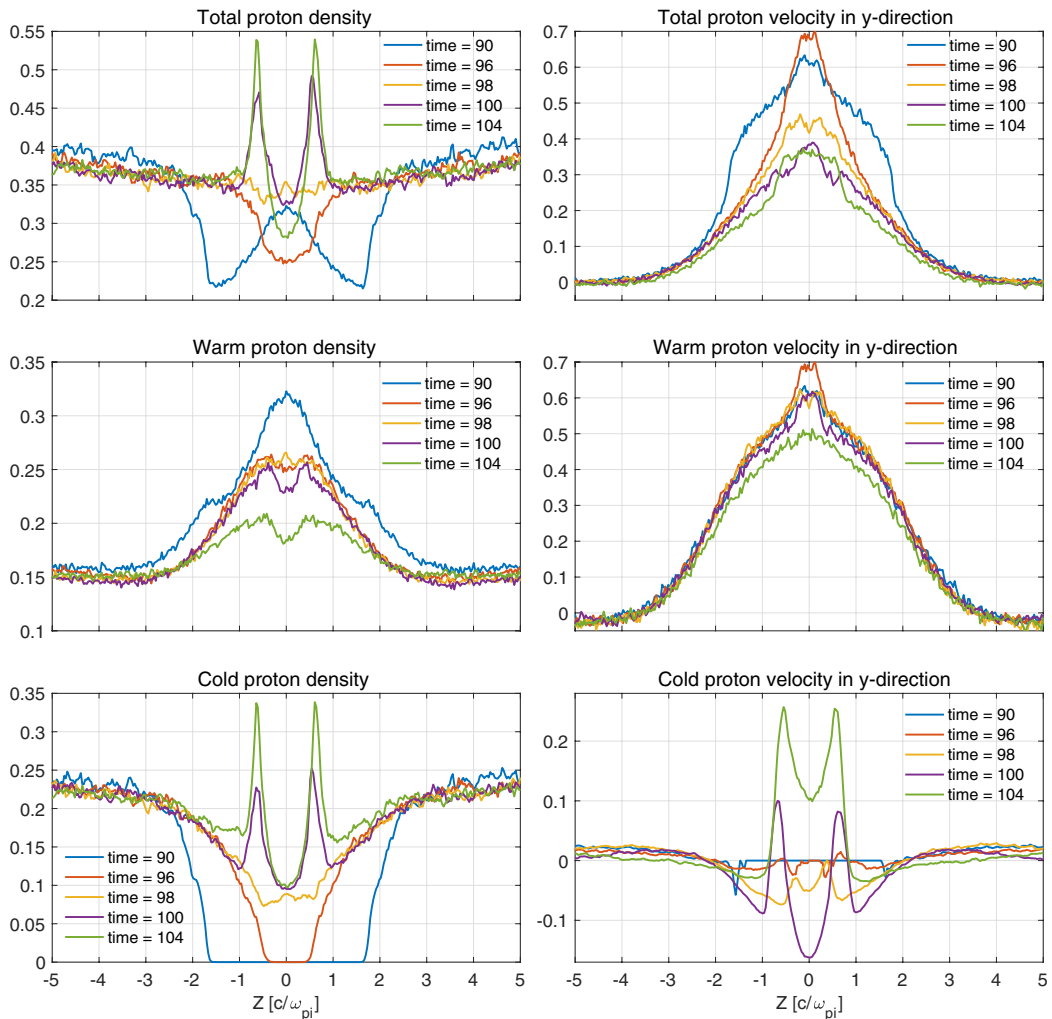
**Figure 4.** The contributing terms to the reconnection electric field as described in Equation 6 ( $q = m = 1$ ), as a function of  $z$  through the X-point before, during and after the cold ions arrive at the reconnection site. The temporal inertia (red) has a significant contribution in the cold run, but a negligible contribution in the baseline run.

sum, the interaction of these oppositely directed process causes a negative  $y$ -directed inertia only in the transition before a large enough density of the cold ions have had enough time to exhibit diamagnetic drift.

## 6. Discussion and Summary

In this work we have investigated the effect of mass-loading by a cold ion population on the evolution of magnetic reconnection. We have looked at both macro- and micro-scale processes, and tried to establish how these are coupled to each other. On macro-scales we have found that mass-loading reduces the reconnection rate significantly, and that this is the dominating contribution to slowing down the reconnection process in





**Figure 5.** Density and  $y$ -directed velocity of the ion populations in the cold run as a function of  $z$  through the X-point at different times. The top row shows the total ion population, the middle row shows the warm ions and the bottom row shows the cold ions. The narrow peaks of positive velocity in the cold population results from the turning at the outer edge of their bounce motion.

this setup. We then found this reduction in the reconnection rate to be consistent with a reduction in the aspect ratio of the ion diffusion region, which is a micro-scale effect of mass-loading. Since the reconnection rate can be given as the reconnection electric field we investigated how these processes are coupled by decomposing this field to its contributing terms. We found that the cold ions carry a significant negative temporal inertia during the transition when they go from not being involved to being fully involved in the reconnection process. This transition phenomenon is only significant until the cold ions have established a sufficiently large positive diamagnetic drift to overpower the negative contribution. Through the full transition period, some cold ions will travel in the negative  $y$ -direction, opposite to both the warm ions and the cold ions that have established a diamagnetic drift. The negative temporal inertia evolves over several ion gyroperiods. This

is within the resolution of MMS (Burch et al., 2016), and both the temporary negative inertia and the counter streaming ions in the  $y$ -direction could therefore be observable as possible signatures of cold ion mass-loading in observations.

### Data Availability Statement

Data for this paper is available at (Spinnangr, 2021).

### Acknowledgments

The authors thank S. Toledo-Redondo for useful discussions. This study was supported by the Research Council of Norway under contract 300865, by NOTUR/NORSTOR under project NN9496K, and by NASA's MMS mission.

### References

- Alm, L., André, M., Graham, D. B., Khotyaintsev, Y. V., Vaivads, A., Chappell, C. R., et al. (2019). MMS observations of multiscale Hall physics in the magnetotail. *Geophysical Research Letters*, *46*(17–18), 10230–10239. <https://doi.org/10.1029/2019GL084137>
- André, M., & Cully, C. M. (2012). Low-energy ions: A previously hidden solar system particle population. *Geophysical Research Letters*, *39*(3). <https://doi.org/10.1029/2011GL050242>
- André, M., Li, K., & Eriksson, A. I. (2015). Outflow of low-energy ions and the solar cycle. *Journal of Geophysical Research: Space Physics*, *120*(2), 1072–1085. <https://doi.org/10.1002/2014JA020714>
- André, M., Li, W., Toledo-Redondo, S., Khotyaintsev, Y. V., Vaivads, A., Graham, D. B., et al. (2016). Magnetic reconnection and modification of the Hall physics due to cold ions at the magnetopause. *Geophysical Research Letters*, *43*(13), 6705–6712. <https://doi.org/10.1002/2016GL069665>
- Burch, J. L., Moore, T. E., Torbert, R. B., & Giles, B. L. (2016). Magnetospheric multiscale overview and science objectives. *Space Science Reviews*, *199*(1–4), 5–21. <https://doi.org/10.1007/s11214-015-0164-9>
- Cassak, P. A., Liu, Y. H., & Shay, M. A. (2017). A review of the 0.1 reconnection rate problem. *Journal of Plasma Physics*, *83*(5). Cambridge University Press. <https://doi.org/10.1017/S0022377817000666>
- Comisso, L., & Bhattacharjee, A. (2016). On the value of the reconnection rate. *Journal of Plasma Physics*, *82*(6), 1–9. <https://doi.org/10.1017/S002237781600101X>
- Dargent, J., Aunai, N., Lavraud, B., Toledo-Redondo, S., & Califano, F. (2019). Signatures of cold ions in a kinetic simulation of the reconnecting magnetopause. *Journal of Geophysical Research: Space Physics*, *124*(4), 2497–2514. <https://doi.org/10.1029/2018JA026343>
- Dargent, J., Aunai, N., Lavraud, B., Toledo-Redondo, S., & Califano, F. (2020). Simulation of plasmaspheric plume impact on dayside magnetic reconnection. *Geophysical Research Letters*, *47*(4). <https://doi.org/10.1029/2019GL086546>
- Dargent, J., Aunai, N., Lavraud, B., Toledo-Redondo, S., Shay, M. A., Cassak, P. A., & Malakit, K. (2017). Kinetic simulation of asymmetric magnetic reconnection with cold ions. *Journal of Geophysical Research: Space Physics*, *122*(5), 5290–5306. <https://doi.org/10.1002/2016JA023831>
- Divin, A., Khotyaintsev, Y. V., Vaivads, A., André, M., Toledo-Redondo, S., Markidis, S., & Lapenta, G. (2016). Three-scale structure of diffusion region in the presence of cold ions. *Journal of Geophysical Research: Space Physics*, *121*(12), 12001–12013. <https://doi.org/10.1002/2016JA023606>
- Fuselier, S. A., Burch, J. L., Cassak, P. A., Goldstein, J., Gomez, R. G., Goodrich, K., et al. (2016). Magnetospheric ion influence on magnetic reconnection at the duskside magnetopause. *Geophysical Research Letters*, *43*(4), 1435–1442. <https://doi.org/10.1002/2015GL067358>
- Fuselier, S. A., Burch, J. L., Mukherjee, J., Genestreti, K. J., Vines, S. K., Gomez, R., et al. (2017). Magnetospheric ion influence at the dayside magnetopause. *Journal of Geophysical Research: Space Physics*, *122*(8), 8617–8631. <https://doi.org/10.1002/2017JA024515>
- Hesse, M., Birn, J., & Kuznetsova, M. (2001). Collisionless magnetic reconnection: Electron processes and transport modeling. *Journal of Geophysical Research: Space Physics*, *106*, 3721–3735. <https://doi.org/10.1029/1999ja001002>
- Hesse, M., Schindler, K., Birn, J., & Kuznetsova, M. (1999). The diffusion region in collisionless magnetic reconnection. *Physics of Plasmas*, *6*(5), 1781–1795. <https://doi.org/10.1063/1.873436>
- Liu, Y. H., Hesse, M., Guo, F., Daughton, W., Li, H., Cassak, P. A., & Shay, M. A. (2017). Why does steady-state magnetic reconnection have a maximum local rate of order 0.1? *Physical Review Letters*, *118*(8), 085101. <https://doi.org/10.1103/PhysRevLett.118.085101>
- Spinnangr, S. F. (2021). Replication data for: The micro-macro coupling of mass-loading symmetric magnetic reconnection with cold ions. DataverseNO. <https://doi.org/10.18710/NWQQBI>
- Tenfjord, P., Hesse, M., & Norgren, C. (2018). The formation of an oxygen wave by magnetic reconnection. *Journal of Geophysical Research: Space Physics*, *123*(11), 9370–9380. <https://doi.org/10.1029/2018JA026026>
- Tenfjord, P., Hesse, M., Norgren, C., Spinnangr, S. F., & Kolsto, H. (2019). The impact of oxygen on the reconnection rate. *Geophysical Research Letters*, *46*(12), 6195–6203. <https://doi.org/10.1029/2019GL082175>
- Tenfjord, P., Hesse, M., Norgren, C., Spinnangr, S. F., Kolsto, H., & Kwagala, N. (2020). Interaction of cold streaming protons with the reconnection process. *Journal of Geophysical Research: Space Physics*, *125*(6), e2019JA027619. <https://doi.org/10.1029/2019JA027619>
- Toledo-Redondo, S., André, M., Khotyaintsev, Y. V., Vaivads, A., Walsh, A., Li, W., et al. (2016). Cold ion demagnetization near the X-line of magnetic reconnection. *Geophysical Research Letters*, *43*(13), 6759–6767. <https://doi.org/10.1002/2016GL069877>
- Toledo-Redondo, S., Vaivads, A., André, M., & Khotyaintsev, Y. V. (2015). Modification of the Hall physics in magnetic reconnection due to cold ions at the Earth's magnetopause. *Geophysical Research Letters*, *42*(15), 6146–6154. <https://doi.org/10.1002/2015GL065129>
- Vasyliunas, V. M. (1975). Theoretical models of magnetic field line merging. *Reviews of Geophysics*, *13*(1), 303–336. <https://doi.org/10.1029/RG013i001p0303>
- Walsh, B. M., Foster, J. C., Erickson, P. J., & Sibeck, D. G. (2014). Simultaneous ground- and space-based observations of the plasmaspheric plume and reconnection. *Science*, *343*(6175), 1122–1125. <https://doi.org/10.1126/science.1247212>
- Yamada, M., Kulsrud, R., & Ji, H. (2010). Magnetic reconnection. *Reviews of Modern Physics*, *82*(1), 603–664. <https://doi.org/10.1103/RevModPhys.82.603>



# Paper II

## **Asymmetrically varying guide field during magnetic reconnection: Particle-In-Cell simulations**

S.F. Spinnangr, P. Tenfjord, M. Hesse, C. Norgren, H.M. Kolstø, N. Kwagala, T.M. Jørgensen, J.P. Jiménez

*Journal of Geophysical Research: Space Physics*, Vol. 127, Issue 1 doi:10.1029/2021JA029955, 2021



# JGR Space Physics

## RESEARCH ARTICLE

10.1029/2021JA029955

### Key Points:

- Spatio-temporal effects in the inflow conditions causes modulations in the reconnection rate and introduces time-dependent effects
- The asymmetrically varying guide field alters the force balance between the current sheet and inflow region
- The outflow regions show nonlaminar exhaust structures induced by the changing inflow

### Correspondence to:

S. F. Spinnangr,  
susanne.spinnangr@uib.no

### Citation:




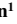


Spinnangr, S. F., Tenfjord, P., Hesse, M., Norgren, C., Kolstø, H. M., Kwagala, N. K., et al. (2022). Asymmetrically varying guide field during magnetic reconnection: Particle-in-cell simulations. *Journal of Geophysical Research: Space Physics*, 127, e2021JA029955. <https://doi.org/10.1029/2021JA029955>

Received 9 SEP 2021  
Accepted 6 DEC 2021

©2021. The Authors.

This is an open access article under the terms of the [Creative Commons Attribution License](https://creativecommons.org/licenses/by/4.0/), which permits use, distribution and reproduction in any medium, provided the original work is properly cited.

## Asymmetrically Varying Guide Field During Magnetic Reconnection: Particle-In-Cell Simulations

Susanne F. Spinnangr<sup>1</sup> , Paul Tenfjord<sup>1</sup> , Michael Hesse<sup>2</sup> , Cecilia Norgren<sup>1</sup> , Håkon M. Kolstø<sup>1</sup> , Norah K. Kwagala<sup>1</sup> , Therese Moretto Jørgensen<sup>2</sup>, and Judit Pérez-Coll Jiménez<sup>1</sup>

<sup>1</sup>Space Plasma Physics Group, University of Bergen, Bergen, Norway, <sup>2</sup>NASA's Ames Research Center, Mountain View, CA, USA

**Abstract** Using fully kinetic particle-in-cell modeling, we investigate how magnetic reconnection responds to a varying guide field in one of the inflow regions. We find that the reconnection rate varies significantly when the orientation of the magnetic field changes between being strictly antiparallel and having a guide field. These variations are fairly consistent with the scaling relation for asymmetric reconnection developed by Cassak and Shay (2007), <https://doi.org/10.1063/1.2795630>. However, the rate is also found to be nonlinearly modulated by changes in the ion inflow velocity. The spatio-temporal change in the inflow velocity arises as the magnetic forces reconfigure to regions of different magnetic field strengths. The variations in the inflow magnetic field configuration allow for different gradients in the magnetic field, leading to asymmetries in the magnetic tension force. By momentum conservation, this facilitates asymmetries in the inflow velocity, which in turn affects the flux transport into the reconnection site. The outflow is found to be less laminar when the inflow varies, and various signatures of the inflow variations are identified in the outflow.

**Plain Language Summary** Magnetic reconnection can be described as magnetic explosions, where energy stored in magnetic fields is converted into heat and movement of particles. It can happen in all environments where magnetic fields and charged particles interact, such as in the Sun, in planetary magnetospheres, and in fusion reactors on Earth. In this article, using numerical simulations, we present new insight into how magnetic reconnection behaves when the magnetic fields vary during the reconnection process.

## 1. Introduction

Magnetic reconnection is a process where stored magnetic energy is converted into kinetic and thermal plasma energy. This energy conversion is caused by a macroscopic change in the magnetic topology. How this process evolves is highly dependent on the conditions of the magnetic fields and plasma in which it occurs. Significant multiscale differences in configuration, evolution, and efficiency of the reconnection process have been shown to depend on both the initial symmetry, shear and magnitudes of the magnetic field, and the temperature, composition, distribution, and dynamics of the plasma (Dargent et al., 2019, 2017; Pritchett & Coroniti, 2004; Swisdak et al., 2003; Tenfjord et al., 2018, 2020; Toledo-Redondo et al., 2021).

Magnetic reconnection can occur in many different locations in our magnetosphere, but the two main types of reconnection are dayside and nightside reconnection. In general, nightside reconnection is more symmetric, while dayside reconnection happens between very different plasma regimes, including strong gradients in particle density, temperature, magnetic field strength, and different magnetic shear. Both dayside and nightside reconnection have been modeled and observed extensively in the last couple of decades, with great strides being made in our observational capabilities since the launch of the magnetospheric multiscale (MMS) mission in 2015 (Burch & Phan, 2016).

In dayside reconnection, the magnetic field of the Earth connects directly with the interplanetary magnetic field (IMF) carried by the solar wind. From theory, large scale modeling, and observations we know that the direction of the IMF relative to the magnetic field of the Earth is crucial in determining how their interaction will occur (Fuselier et al., 2011; Trattner et al., 2017, 2007). In most cases of dayside reconnection, Earth's planetary and the IMF are not strictly antiparallel, meaning that the reconnecting fields are only the components of the total fields that happen to be antiparallel. During such guide field or component magnetic reconnection, the dynamics and global behavior of the reconnection process is modified on all scales compared to the strictly antiparallel

scheme. The addition of a guide field alters the kinetic behavior of the particles in the diffusion region (Goldman et al., 2011; Pritchett & Mozer, 2009) and the global configuration and efficiency of reconnection as a whole (Pritchett, 2005; Pritchett & Coroniti, 2004; Swisdak et al., 2005; Trattner et al., 2017).

Great progress has been made toward understanding symmetric, asymmetric, and guide field magnetic reconnection, both through modeling and observations (e.g., Burch et al., 2016; Cassak & Fuselier, 2016; Chen et al., 2017; Fuselier et al., 2017; Hesse et al., 2016, 2021; Torbert et al., 2018; Wilder et al., 2018). Several simulation studies compare how similar reconnection schemes are modified by changing one or more of the initial conditions (Dargent et al., 2020; Kolstø et al., 2020a, 2020b; Spinnangr et al., 2021; Tenfjord et al., 2019, 2020). As the Sun, the solar wind and the magnetosheath are highly dynamic, it is of great importance to understand how a reconnecting system responds to variations in the inflow conditions, in particular for dayside reconnection. Scenarios such as variations in the IMF, flux rope coalescence (Akhavan-Tafti et al., 2020, 2019; Zhou et al., 2017), and reconnection (Poh et al., 2019) can all give rise to reconnection events where the inflow magnetic shear angle varies. With this in mind, we employ in this study 2.5D fully kinetic particle-in-cell (PIC) simulations to investigate how the transition between different inflow conditions occur, by imposing asymmetric variations in the inflow magnetic field during one simulation of a reconnection event. By effectively turning on and off a guide field in one of the inflow regions by rotating the magnetic field into the out-of-plane direction, we find variations in both large and small scale dynamics of the system.

The reconnection rate shows significant temporal variations associated with the transient field variations. Consequently, the system is prevented from settling to a quasi-steady state through almost the full simulation time. We find that the variations in the reconnection rate cannot be fully explained by common scaling schemes such as the symmetric Sweet-Parker (Cassak et al., 2017; Comisso & Bhattacharjee, 2016; Y. H. Liu et al., 2017) or general Cassak and Shay (2007) scaling. In particular, we find that nonlinear effects become important, as changes in the reconnection rate precede changes in the inflow, leading to overshoots in the rate. As the rate varies, so does the flux transport into and out of the reconnection site. We also identify large scale structures in the exhaust that can act as signatures of varying inflow conditions, which are very different from the otherwise laminar exhaust of normal, antisymmetric reconnection.

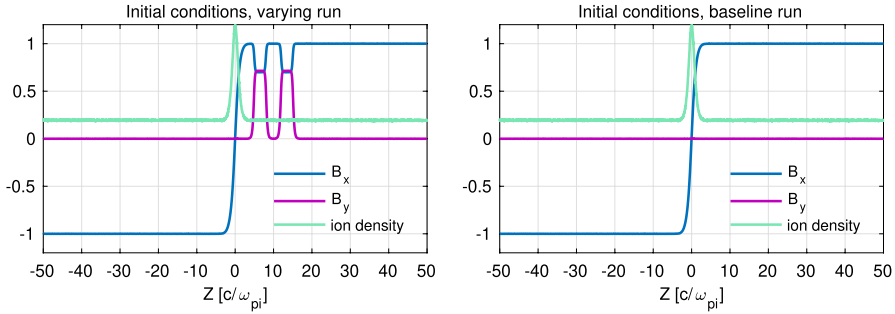
The structure of the article is as follows: In Section 2, we describe the simulation setup we have employed in this study. In Section 3, we investigate how the reconnection rate varies with the variations in the inflow. Section 4 is a closer investigation of the flux transport into the reconnection site, while, in Section 5, we investigate how the exhaust responds to the inflow variations. Section 6 is a summary of our results with some discussion.

## 2. Simulation Setup

We utilize two fully kinetic, 2.5D PIC simulations, both based on the code described by Hesse et al. (1999), initializing a Harris current sheet of half-width  $l = 1 d_i$ . Lengths are normalized to the ion inertial length,  $d_i = \frac{c}{\omega_{pi}}$ , where  $\omega_{pi} = \sqrt{\frac{n_0 e^2}{\epsilon_0 m_i}}$  is the ion plasma frequency with  $n_0$  being the initial Harris current sheet density and  $m_i$  is the ion mass. Time is normalized to the inverse ion cyclotron frequency,  $\Omega_i^{-1} = \frac{m_i}{e B_0}$ , where  $B_0$  is the initial asymptotic magnetic field, and we employ a time step of  $\omega_{pe} \delta t = 0.5$ . Densities are normalized to  $n_0$ , and velocities are normalized to the ion Alfvén velocity,  $v_A = B_0 / \sqrt{\mu_0 m_i n_0}$ . A highly localized perturbation is employed, initializing the magnetic reconnection process. In our coordinate system,  $x$  is the reconnection outflow direction,  $y$  is the initial current direction, and  $z$  is the inflow direction. The boundary conditions are periodic in the  $x$ -direction and specular reflection in the  $z$ -direction. We use a total of  $1 \times 10^9$  macro-particles, and the size of the simulation domain is  $204 d_i \times 102 d_i$  divided into a grid of  $3,200 \times 3,200$  cells. The ions and electrons have a mass ratio of  $\frac{m_i}{m_e} = 25$  and their temperature ratio is  $\frac{T_e}{T_i} = 0.2$ . The ratio of the ion plasma frequency to the electron cyclotron frequency is  $\omega_{pe} / \Omega_e = 2$ .

We refer to the two simulations as the baseline run and the varying run, where the varying run includes an asymmetric, varying magnetic field contribution in the  $y$ -direction with associated current modifications, but is otherwise identical to the baseline. Our initial magnetic field configuration is:

$$B_x = B_0 \tanh(z/l) f(z) \quad (1)$$



**Figure 1.** Cut along  $Z$  through the center of the box showing the initial values of the magnetic fields and the ion density for the varying run (left) and the baseline run (right). The total magnitude of the magnetic field ( $B = \sqrt{B_x^2 + B_y^2}$ ) is the same in both runs.

$$f(z) = 1 + \alpha \sum_{j=1}^4 (-1)^j \left( 1 + \tanh\left(\frac{z - z_j}{\lambda}\right) \right) \quad (2)$$

$$B_y = \sqrt{\tanh^2(z/l) - B_x^2} \quad (3)$$

The function  $f$  modifies the magnetic field direction, effectively turning on and off the guide field. The factor  $z_j$  in  $f(z)$  specifies the locations in the inflow regions where the field direction changes, which we have set as  $[5.7.5, 10.12.5]d_i$ , creating two horizontal bands of positive  $B_y$  in the inflow region above the current sheet. The factors  $\alpha = 0.15$  and  $\lambda = 0.25 d_i$  serve to modify the magnitude and steepness of the variation, respectively. When  $|z - z_j|$  is large,  $f = 1$ , which is the case everywhere for the baseline run where Equations 1 and 3 reduce to the normal Harris configuration. Our magnetic field configuration ensures that the magnitude of the total magnetic field stays constant when the field changes direction. Hence, only the magnetic field components change, while the total magnetic energy density remains the same. Figure 1 shows the initial values of the magnetic field profile and the ion density for both runs. In Figure 2, we give an overview of the time evolution of the  $y$ -directed magnetic field for both runs and the total  $y$ -directed current for the varying run. In the first panel of the middle column, we label different regions of the inflow that will propagate through the simulation. We will continue to use these labels for referencing throughout the text.

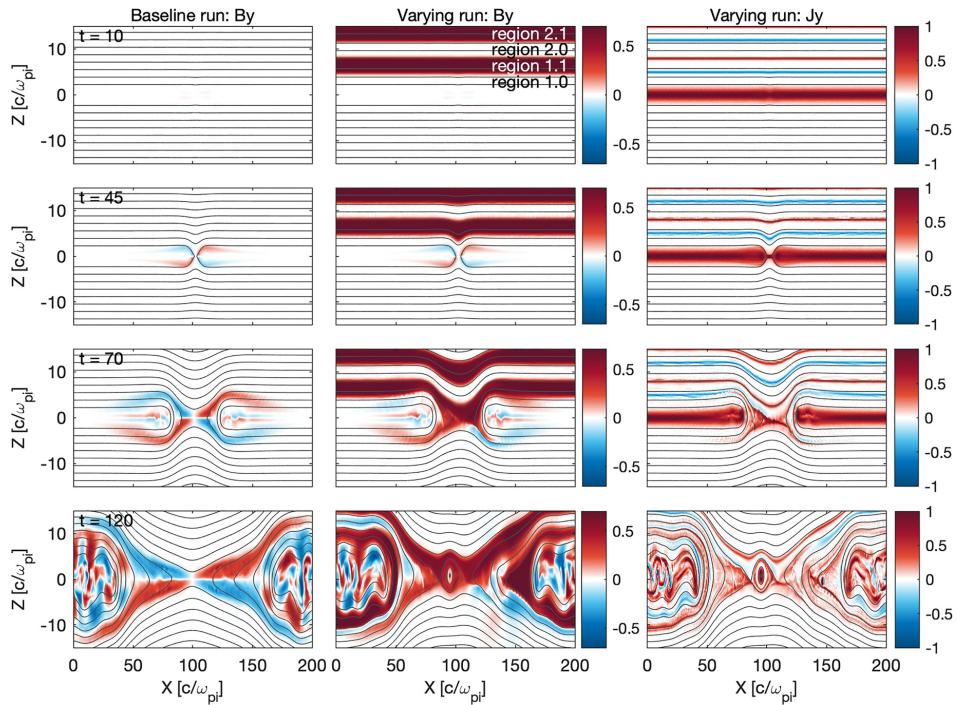
### 3. The Reconnection Rate

The reconnection rate tells us how fast the reconnecting system is able to convert magnetic energy into plasma kinetic and thermal energy, and therefore says something about how effective the reconnection process is. In Figure 3, we show the amount of reconnected flux,  $\Phi$ , and the reconnection rate,  $d\Phi/dt$ , as functions of time. By looking at the reconnected flux, we see that the baseline reconnects more efficiently, and has converted about 12% more magnetic energy in the same amount of time compared to the varying run at the end of the runs. Based on earlier studies, this is about the same reduction we could expect from introducing a uniform guide field in the whole box (Huba, 2005; Ricci et al., 2004; Swisdak et al., 2005).

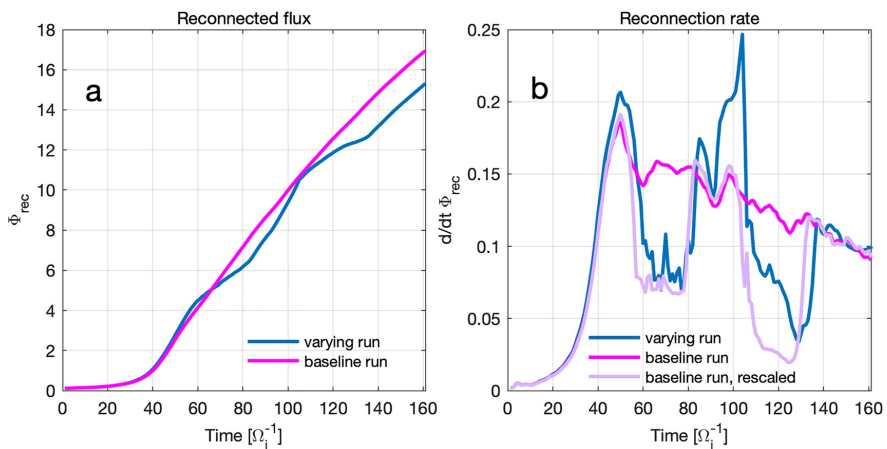
When we compare the reconnection rates, we see that the two runs behave very similarly until they start to deviate significantly around  $t = 40$ . The baseline run exhibits the expected behavior, with a fast increase in the rate followed by a slow and steady decline as the amount of magnetic energy available in the system is being depleted. The varying run on the other hand, shows significant variations in the rate, which coincide with the varying inflow conditions. As a first step in analyzing these variations, we develop a scaling relation based on the reconnection rate scaling for asymmetric reconnection developed by Cassak and Shay (2007). They find a general expression for the reconnection electric field in an asymmetric configuration:

$$E \sim \left( \frac{B_1 B_2}{B_2 + B_1} \right) v_{out} \frac{2\delta}{L} \quad (4)$$





**Figure 2.** Overview of the evolution of the  $y$ -directed magnetic field in the two runs, as well as the  $y$ -directed current in the varying run. The contours show the in-plane magnetic field. We have labeled the regions of different magnetic field configurations in the top inflow region to refer to them more easily in the analysis later. When the decimal is 0, the  $B_y$  is also 0.



where  $B_1$  and  $B_2$  are the asymmetric magnetic field magnitudes in the inflow regions,  $v_{out}$  is the outflow speed, and  $\frac{\delta}{L}$  is the aspect ratio of the diffusion region. They also find a general expression for the outflow speed, which in our runs reduces to:

$$v_{out}^2 \sim \frac{B_1 B_2}{\rho} \quad (5)$$

Here, we use their expressions for a symmetric density distribution. In the baseline run, the density is symmetric, while in the varying run some small asymmetries develop during the course of the run. The  $\rho$  we use in Equation 5 for the varying run is the average  $\rho$  above and below the current sheet. The ratio of the density difference between the two inflow regions to this average density is small compared to the corresponding ratio for the magnetic field,  $(\rho_1 - \rho_2)/\rho \sim 0.25$  while  $(B_1 - B_2)/B \sim 0.8-1.2$ , and we ignore them in this analysis. Equations 4 and 5 can be interpreted as the reconnection electric field and the outflow velocity based on the effective magnetic field in the inflow, respectively.

Dividing Equation 4 for the varying run,  $E_v$ , by that for the baseline run,  $E_b$ , we find a scaling factor for the reconnection electric field:

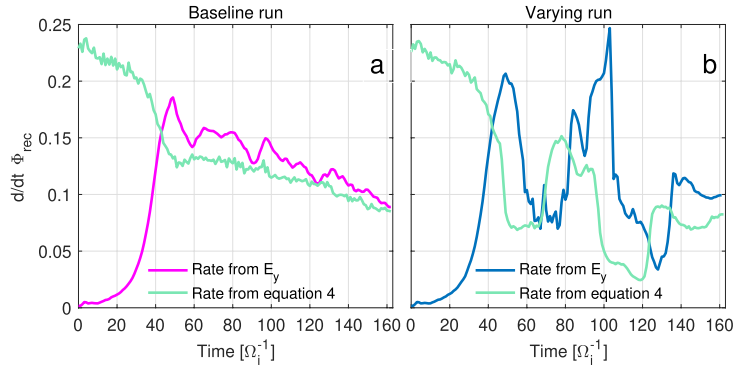
$$\frac{E_v}{E_b} \sim \frac{\frac{B_1 B_2}{B_1 + B_2} \sqrt{\frac{B_1 B_2}{\rho}} \frac{2\delta}{L}}{\frac{B}{\sqrt{\rho}} \frac{\delta}{L}} = \frac{2(B_1 B_2)^{\frac{3}{2}}}{B^2(B_1 + B_2)} \quad (6)$$

The magnetic field below the current sheet in the varying run,  $B_2$ , behaves in the same way as the baseline magnetic field,  $B$ , ( $|B - B_2| \sim 0.2$ ), so we can set  $B_2 = B$  in Equation 6, which then reduces to:

$$\frac{E_v}{E_b} \sim \frac{2(B_1)^{\frac{3}{2}}}{\sqrt{B_2}(B_1 + B_2)} \quad (7)$$

The right hand side of Equation 7 is now a scaling factor, only dependent on the magnetic field strengths, which we can use to compare the reconnection rate in our varying run with what has been reported for constant (or global) asymmetric configurations. In Figure 3b, we have plotted the baseline run rescaled with this factor together with the original rates from the two runs. The slight shift in time between the variations in the guide field rate and the rescaled baseline rate happens because we pick values for  $B_1$  and  $B_2$  1  $d$ , away from the X-point, meaning the scaling factor uses a reduced field strength before it actually arrives at the reconnection site. We see that by rescaling the baseline with the magnetic field variations in the varying run, we capture some of the overall behavior observed in the varying run, but there are still major differences between the rescaled baseline run and the varying run. Most notably, we see that the rescaling does not capture the overshoots in the rate occurring around  $t = 50$  and  $t = 100$  in the varying run. Also, for the second rate reduction between  $t = 110$  and 135, the rescaling predicts a much larger rate reduction than the actual rate observed in the varying run. These differences indicate that there are important dynamics other than just the imposed field variations that dictate the behavior of the reconnecting system.

We can also use Equations 4 and 5 directly to estimate the reconnection rates based on the inflow conditions. In Figure 4, we have plotted the reconnection rates of the two runs, calculated using two different methods. The magenta and blue lines show the rates calculated based on the reconnection electric field for the baseline and the varying run respectively. These are the same rates as in Figure 3b. The turquoise lines in Figure 4 show the rates calculated using Equations 4 and 5 directly, with values for the magnetic field and density taken at  $Z = \pm 3$  above and below the X-point, and assuming  $\frac{\delta}{L} = 0.1$ . Again, we see the large reductions in the rate are captured and to some degree overestimated, while the overshoots are not captured at all. The large difference between the rates before about  $t = 40$  is artificial, as Equation 4 cannot give the correct rate before reconnection is ongoing. The larger delay between the two calculation methods compared to the delay when we do the scaling occurs because we must extract the relevant values further away from the current sheet when we apply Equation 4 directly, in order for expressions to be applicable. Closer to the X-point, the magnetic field strength is reduced, and using these values in Equation 4 therefore significantly underestimates the rates, while in the scaling it only modifies the actual rate, so the magnitude is not significantly affected by where we extract the values. The choice of aspect



**Figure 4.** Comparison of the reconnection rates calculated using the reconnection electric field ( $E_y$ ) and Equation 4. The values of the magnetic field and density needed in Equation 4 were taken at  $Z = 3 d_i$ , which explains the offset in timing of the variations in the varying run.

ratio = 0.1 has been shown to be a reasonable value in many different reconnection configurations (Cassak et al., 2017; Comisso & Bhattacharjee, 2016).

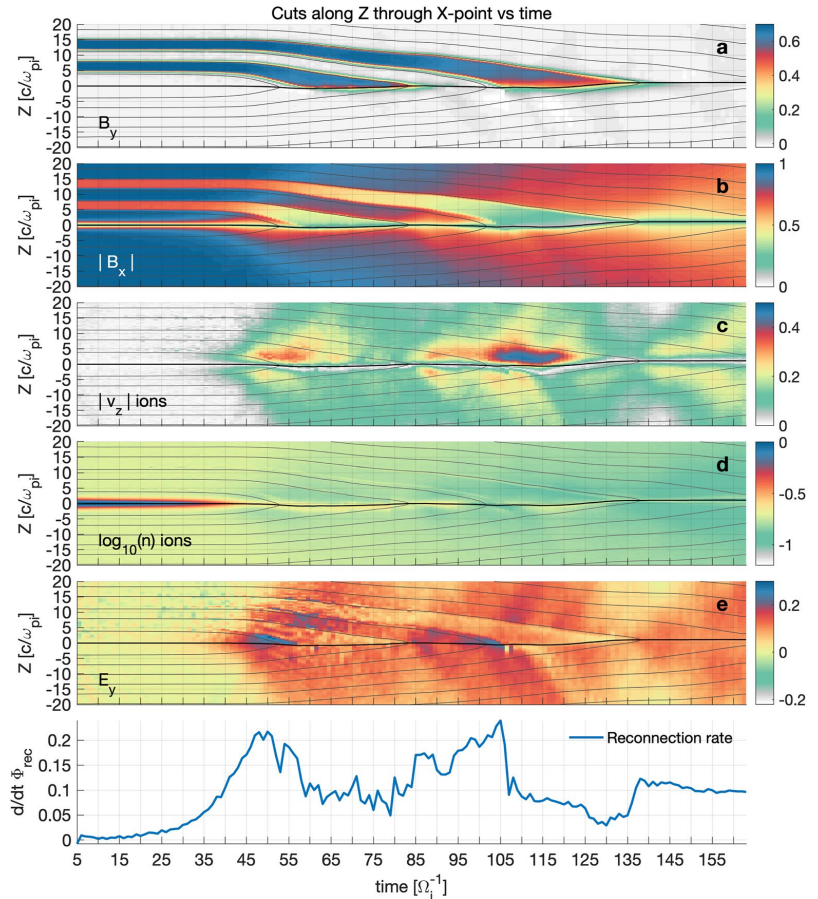
The scaling of the reconnection rate presumes a quasi-steady state, and as we will see in the next section, our system is not quasi-steady until the variations in the inflow have convected downstream of the X-point. Since the reconnection rate is a measure of how efficiently the reconnection process converts magnetic flux, it says something about how efficiently the flux is transported into and out of the reconnection region. This means that the system must somehow adjust the flux transport into the reconnection site in response to the variations in the magnetic field. We will analyze this further in the next section.

#### 4. Flux Transport Analysis

In the previous section, we saw that the reconnection rate is significantly affected by the varying inflow conditions, but not in a manner that is consistent with the magnetic field configurations alone. In this section, we investigate more closely how the reconnecting system readjusts itself to the variations in the inflowing magnetic field. In Figure 5, we show the evolution of  $B_y$ ,  $|B_x|$ , the ion  $|v_x|$  and density  $n$ , and  $E_y$  as a function of time, together with the reconnection rate. To construct these plots, we have taken slices along  $z$  through the X-point for every time step of the simulation, and then plotted these slices consecutively with time on the  $x$ -axis. All the variables in each slice are averaged over a distance  $0.1 d_i$  to both sides of the X-point to reduce noise. The dark gray lines in panels a through e are lines of constant values of the magnetic vector potential,  $\mathbf{A}$ , defined by  $\mathbf{B} = \nabla \times \mathbf{A}$ . We construct these lines by extracting values of  $\mathbf{A}$  for each time step along the same slices as described above. They indicate the motion of given magnetic fields lines in the inflow region. The black line around  $z = 0$ , where the gray lines converge, is the position of the dominant X-point.

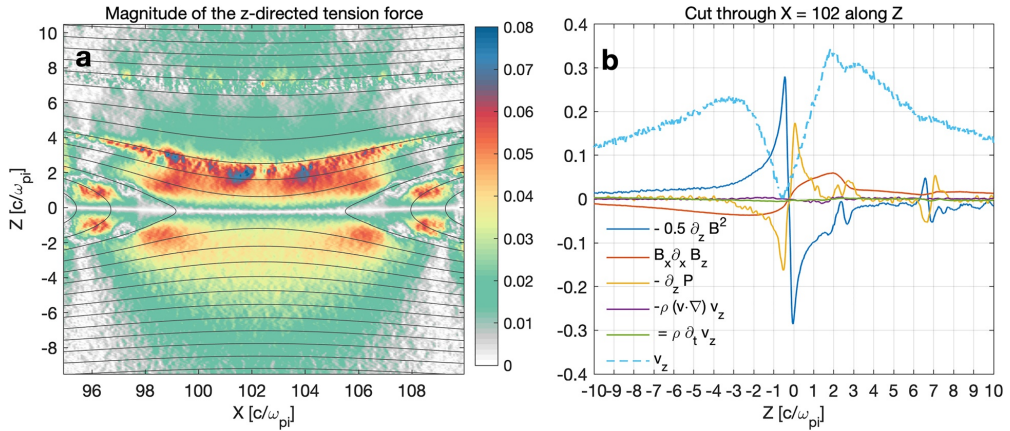
In Figures 5a and 5b, the regions where the direction of the magnetic field is turned toward the  $y$ -direction are seen as bands of enhanced and decreased magnitudes of  $B_y$  and  $B_x$  respectively, that move in toward the reconnection site as time progresses. These bands correspond to the initial bands of magnetic field labeled regions 1.1 and region 2.1 ( $B_y = B_x = 0.7$ ) in Figure 2, while the regions inside and between the two bands correspond to region 1.0 and 2.0 ( $B_y = 0$ ). In Figure 5c, we see that as regions 1.1 and 2.1 move toward the reconnection site (from around  $t = 48$  and  $t = 93$ ), a significant asymmetric increase in the inflow velocity occurs. This is the case for both regions, but it is especially apparent for region 2.1. The change in inflow velocity somewhat precedes the change in the magnetic field, evident from the fact that the velocity asymmetry both builds up and recedes before the equivalent change in the magnetic field arrives at the X-point.

We can explain this behavior and the offset in timing between the changes in the inflow velocity and the magnetic field by force balance arguments. The inflow velocity is to a large degree determined by how quickly the reconnection process convects the plasma out in the exhausts. To maintain pressure balance, the inflowing plasma is



**Figure 5.** Temporal evolution of inflow regions. Panels (a) through (e) shows cuts through the dominating X-point along the  $z$ -direction, each cut plotted as a function of time (see text for detailed description of plot construction). The dark gray lines in panels (a) through (e) are lines of constant values of  $A$ , and the black line along the center shows the position of the X-point. Panel (a) shows  $B_y$ , panel (b) shows the magnitude of  $B_x$ . In both, we see regions 1.1 and 2.1 presented as bands of different field strength moving toward the X-point as time progresses. Panel (c) shows the magnitude of the ion inflow velocity, panel (d) shows the ion density in log scale, panel (e) shows the reconnection electric field, and the last panel shows the reconnection rate.

heated to balance the pressure loss from convection to the outflow. If the convection of pressure out of the central region is not balanced by transport of plasma in the inflow, Alfvén waves are launched to adjust the inflow appropriately and vice versa, that is, the inflow and outflow are not independent of each other. In Figure 5d, we see that the initial current sheet density has already been convected into the exhaust around  $t = 40$ , before the changes in magnetic field start to interact with the reconnection process. The transport of the reconnection magnetic field component,  $B_x$  toward the X-point is governed by the strength of the field and the speed at which it is transported. Since  $B_x$  is lower in regions 1.1 and 2.1, the system must readjust itself to ensure that the flux is convected equally from the top and the bottom inflow.



**Figure 6.** Panel (a) shows a map of the magnitude of the  $z$ -directed tension force around the reconnection site, with contours of the in-plane magnetic field. Notice region 1.1 between about  $Z = 3$  and  $Z = 7$ , where the magnitude of the in-plane magnetic field is smaller, as indicated by the larger spacing between the contour lines. Panel (b) shows a cut along the  $z$ -direction through  $X = 102$  of all the terms in Equation 8. The red line is the tension force, and the cyan dotted line is the inflow velocity. The purple and green lines are the inertia contributions, which we see are negligible. Both panels are for  $t = 50$ , corresponding to the time of the first peak reconnection rate.

The changes in the inflow velocity when region 1.1 approaches the reconnection site can be understood by looking at the balance between the magnetic forces and the thermal pressure force. These forces can be expressed through the total momentum equation as:

$$\begin{aligned} \rho \left( \frac{\partial v_z}{\partial t} + v_z \frac{\partial v_z}{\partial z} \right) \sim 0 &= \left( \vec{J} \times \vec{B} - \nabla P \right)_z \\ &= -\frac{\partial}{\partial z} \left( \frac{1}{2} B^2 + P \right) + B_x \frac{\partial B_z}{\partial x} \end{aligned} \quad (8)$$

where  $\rho$  is the ion mass density,  $v$  is the ion velocity,  $B$  is the magnetic field and  $P$  is the plasma pressure. As we will show later, the inertia terms are small and can be neglected in the following analysis. The first and second terms of the second line represents the magnetic and thermal pressures, respectively. The last term represents the magnetic tension, which becomes important as the field lines expands toward the diffusion region. Since the tension force is proportional to  $B_x$ , the reduction of  $B_x$  inside regions 1.1 and 2.1 leads to a top-bottom asymmetry in the magnetic tension force. To intuitively understand the overshoot (and undershoot) of the reconnection rate described in the previous section, as well as the motion of the X-point which we discuss later in this section, we consider the variation in this tension term, both in its total magnitude and in the distribution between the two factors.

The initial conditions are a Harris sheet configuration with varying guide field, where the thermal and magnetic pressure are in balance. Once reconnection starts, and magnetic flux is convected toward the X-point, the field starts to deform, generating a gradient in  $B_z$  along the  $x$ -direction as it expands, giving rise to a tension force. Before region 1.1 gets involved in the reconnection process, that is, until approximately  $t = 45$ , the tension on the two sides is approximately symmetric.

When region 1.1 approaches the diffusion region, the symmetry of the tension force above and below the current sheet breaks down. To understand how the system reconfigures to accommodate the spatially asymmetric tension we look at the momentum equation along a cut through  $X = 102$  along the  $z$ -direction. Figure 6a shows a map of the magnitude of the  $z$ -directed tension force, and Figure 6b shows the components of Equation 8, both at  $t = 50$ . The dark gray lines in the map are contour lines of the in-plane magnetic field. We can see the location of region 1.1 in the inflow where the spacing between the contour lines is larger, approximately between  $z = 3 d_i$  and  $z = 7 d_i$ . There is a clear asymmetry in the tension force above and below the current sheet. The tension force is reduced in region 1.1 ( $z \sim 3 d_i$ ) compared to the corresponding distance from the X-point in the bottom inflow region

( $z = -3$ ). However, closer to the reconnection site,  $0.5 < |z| < 3$ , the tension is stronger in the top inflow. This is also seen in Figure 6b (red line) where the tension is stronger for the top side close to the reconnection site, but is clearly reduced in region 1.1 ( $z > 2.5 d_i$ ).

The reduced tension in region 1.1 allows the region to expand, which exerts a larger pressure force on the inner region (1.0). Region 1.0 is thus compressed, leading to a higher magnetic pressure and tension force in this region. The effect of this is an increase in  $v_z$  in the top inflow, as seen in Figure 6b (dotted line). As a consequence of the enhanced  $v_z$ , the flux tubes ahead of the region of reduced tension are deformed further, as they experience a higher local transport toward the reconnection site. During this equilibration process, the current sheet is moved slightly downwards, as can be seen in the black line in Figure 5.

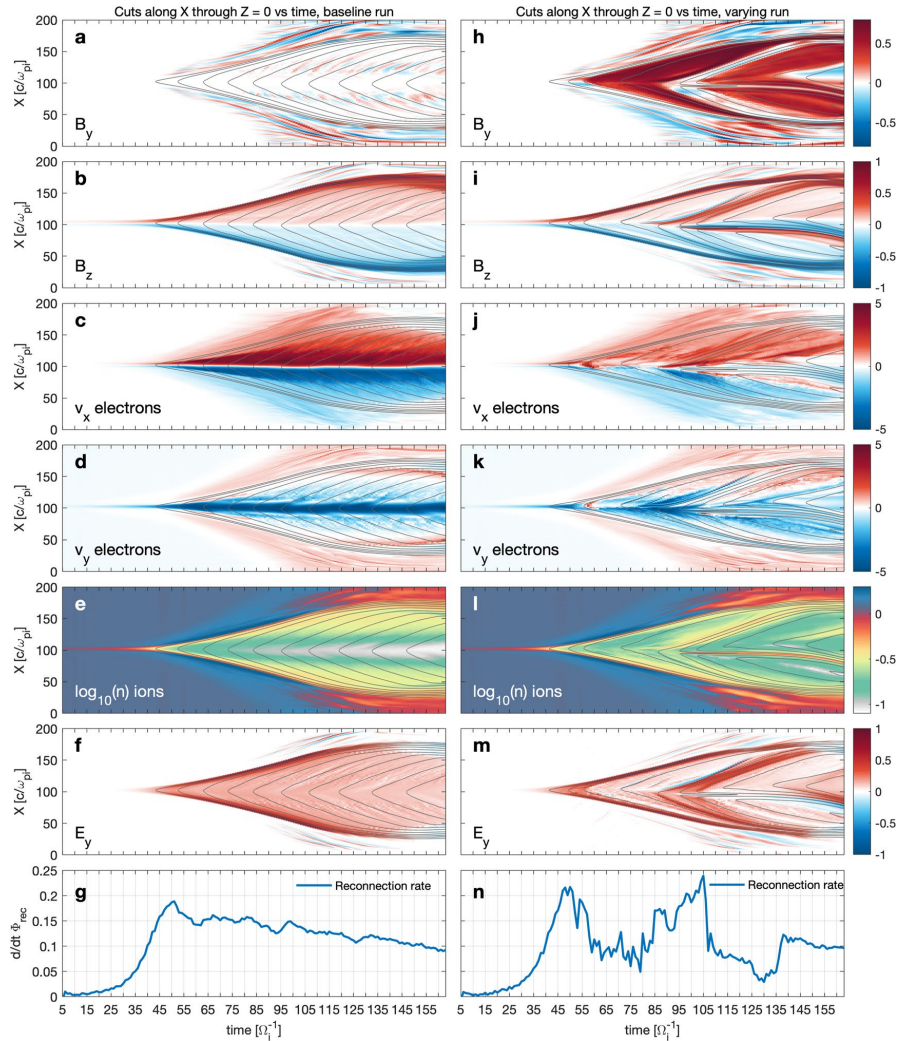
The thermal and magnetic pressure forces also respond to the dynamics induced by the tension force, seen in Figure 6b between  $z = 2$  and  $z = 3 d_i$ . The expansion of the regions of lower tension force is also what facilitates the nonlinearity of the reconnection rate variations we observed in the previous section. Since the field deformation is not confined to the regions 1.1 and 2.1 of sheared magnetic field (finite  $B_y$ ), the increased inflow velocity and its effect on the flux transport can reach the X-point before regions 1.1 and 2.1. This leads to the overshoots in the rate around  $t = 50$  and  $t = 105$  and explains why the rate does not drop as low as the scaling with the magnetic field magnitudes predicted for  $t = 60$ –80 and  $t = 110$ –130, the so called undershoots.

The detailed analysis of the flux transport in this section was motivated by the dynamics of the reconnection rate we presented in the previous section. It was clear that the rate variations could not be explained by the magnitude of the reconnecting field component alone (Equation 7). In Figure 5e, we see variations in the strength of  $E_y$  that are associated with the variations in the inflow velocity and the  $B_x$  component. At the times of the overshoots in the reconnection rate ( $t = 50$  and  $t = 105$ ), we see clear, continuous enhancements in the strength of  $E_y$  a few  $d_i$  away from the X-point in the top inflow. As regions 1.1 and 2.1 reach the X-point, the reduction of the  $B_x$  component is large enough that the  $E_y$  and the reconnection rate are reduced, but by the same argument, the increased  $v_z$  makes this reduction less than it would have been if the inflow velocity remained the same.

We have seen in this analysis of the inflow that asymmetries in the magnetic tension force facilitate an increased inflow velocity from the top inflow region. By the same arguments, we can describe how the X-point moves back up to its original equilibrium position when reconnecting region 2.0 and after reconnecting region 2.1. We see this happening in Figure 5 between  $t = 60$  and  $t = 80$ , and  $t = 115$  and  $t = 130$ . The system finally settles in a quasi-steady state as region 2.1 is convected into the outflow and the inflow becomes symmetric once again, from about  $t = 140$  and onwards. This simulation also emphasizes that a quasi-steady-state is not achieved immediately, and signatures of the reconfiguration are present during a significant portion of the simulation time. The different regions of magnetic shear in the inflow region are convected into the reconnection site with a velocity defined by the flux transport, which we have seen varies. Nevertheless, the transition between the two shear configurations happen over about 3–4 ion cyclotron times, and each configuration phase at the x-point lasts for about 10–30 ion cyclotron times, as can be seen in Figure 5. If we assume a magnetic field strength of 20 nT, which is typical for the dayside magnetosheath (Toledo-Redondo et al., 2021), one ion cyclotron time corresponds to 3 s. The turning of the magnetic field in this simulation therefore occurs in about 10 s, and the duration of each configuration phase at the reconnection site is in the order of one minute. In the next section, we will see that the modulations to the reconnection rate caused by non-steady inflow conditions are also manifested in the outflow magnetic and electric fields.

## 5. Exhaust Structure

As discussed in the previous section, the behavior of the inflow and the outflow are interconnected, and it is therefore natural to assume that the variations in the inflow will affect the outflow. In Figure 7, we have plotted variables in the outflow using the same approach as in Figure 5. Here, the slices are taken along the x-direction through  $z = 0$  instead of following the X-point along the z-direction. As we saw in the previous section, the X-point does move up and down during the reconnection process. We still chose to cut through  $z = 0$  as the effect of this vertical movement is more local in and around the diffusion region, while in this analysis we will investigate general features further out in the outflow that are unaffected by this dynamic. From the top to bottom in Figure 7, we show  $B_y$  and  $B_z$ , the electron outflow velocities  $v_x$  and  $v_y$ , the ion density and the reconnection electric



**Figure 7.** Cuts through  $z = 0$  along the  $x$ -direction, plotted as a function of time (see text for detailed description of plot construction). Panels (a) through (g) are the baseline run, panels (h) through (n) are the varying run. The dark gray lines in panels showing a color map are lines of constant values of the magnetic field vector potential,  $A$ . Panels (a and h), and (b and i) show the  $y$  and  $z$ -directed magnetic field, panels (c and j), and (d and k) show the  $x$  and  $y$ -directed electron velocities, panels (e and l) show the ion density in log scale, panels (f and m) show the reconnection electric field, and panels (g and n) show the reconnection rates.

field,  $E_y$ , ending with the reconnection rate. The panels in the left column show the variables for the baseline run, while the ones in the right column are the varying run.

Looking at the panels in the baseline column, we see that the baseline run evolves smoothly, with a laminar outflow. The magnetic and electric fields are generated and convected symmetrically in both directions along  $x$ , and the initial current sheet is convected away smoothly. The electron velocities show well defined enhancements in both the  $x$ - and  $y$ -direction close to the middle of the  $x$ -axis. The enhancement in the  $v_{x,z}$  corresponds to the embedded electron jet caused by the meandering motions of the electrons (Drake et al., 2008; Shuster et al., 2015;

Tenfjord et al., 2020). Just by a quick glance at the column showing the varying run it is easy to see that the varying inflow conditions have an impact on the structure of the outflow, making it significantly less laminar. We see clear signatures associated with the varying guide field that appear at the X-point and propagate downstream. With the exception of the initial pile-up of magnetic field  $B_z$ , and corresponding flux, that forms at around  $t = 50$ , these structures are not present at all in the baseline run. In both the magnetic and electric fields, as well as in the ion density, we see well defined regions where the  $B_y$  component is being convected. We saw in the previous section that regions 1.1 and 2.1 become broader in time as they approach the X-point in the inflow when the flux transport is slower. We see the same broadening of these regions in the outflow in Figure 7h. Where there is no  $B_y$ , we see enhancements in both the  $B_z$  component, the reconnection electric field and the ion density. Although the density was initially uniform and symmetric between the two inflow regions, the variations introduced by the varying inflow magnetic field leads to density variations in the outflow. For both runs, the first region of enhanced  $B_z$  is associated with a density decrease. This density decrease is related to the decrease in the inflow density seen in Figure 5d. In contrast, the following flux pile-up region in the run with varying guide fields, forming at around  $t = 85$ – $105$ , is associated with a density increase.

By considering the timing of their appearance in the outflow and their behavior as collective structures, in addition to their absence in the baseline run, we suggest that these transient structures in the outflow are formed as a consequence of the varying inflow conditions. An important implication of this is that structures originating in the inflow survive the reconnection process and are convected out in the outflow. This means that structured, nonlaminar outflows can be a consequence of the inflow conditions rather than the result of kinetic dynamics in the diffusion region. Such structures in the outflow may therefore be useful to infer the inflow conditions necessary to create them. Observations of large scale variations in the outflow can be a direct consequence of varying inflow conditions. However, the variations in the outflow can also be formed as an indirect consequence of the inflow variations, by the means of reconnection rate changes. The variation in  $B_z$  is one example of this. A higher reconnection rate means more flux transport in the outflow, while a lower rate leads to slower transport of  $B_z$  flux. These variations in formation rate and propagation speed of  $B_z$  lead to the formation of flux pile-up regions where the magnitude of  $B_z$  is enhanced, when fast moving field lines catch up with slower moving field lines (Norgren et al., 2021). In Figure 7, we can see that the flux pile-up regions form during times of increased reconnection rate. Since we have shown that the reconnection rate variations are caused by the variations of the inflow guide field, we also conclude that secondary flux pile-up region in the run with varying guide field is a result of the varying guide field. In extension, we would also expect that similar  $B_z$  variations in the outflow form in systems with a reconnection rate that varies due to other factors in the inflow or the diffusion region.

We also see differences in the electron dynamics between the two runs. Figures 7c and 7d show the electron outflow velocities,  $v_{ex}$  and  $v_{ey}$ , respectively, for the baseline run, while Figures 7j and 7k show the same for the varying run. In the varying run, we have a significantly reduced outflow speed compared to the baseline run. Both  $v_{ex}$  and  $v_{ey}$  in the varying run are also significantly more structured compared to the laminar outflow in the baseline, exhibiting regions of electrons flowing in the opposite direction and with a lot of small scale structures of different velocity magnitudes. Comparing Figures 7c and 7j, we clearly see the embedded electron jets close to the X-point in the baseline run, while they are not distinct in the varying run. The electron jets associated with antiparallel symmetric reconnection with uniform inflow have been observed (Phan et al., 2007) and modeled (Hesse et al., 2008) to be faster than the  $\vec{E} \times \vec{B}$  drift, suggesting that the jetting electrons are demagnetized. When reconnecting regions 1.0 and 2.0, we see an increase of the  $v_{ex}$  close to the X-point, but this feature is destroyed when reconnecting regions 1.1 and 2.1. This is consistent with earlier studies of electron dynamics during guide field reconnection, where it has been shown that a guide field will deflect the  $x$ -directed electrons along the separatrices (Goldman et al., 2011). The regions of increased and decreased  $v_{ex}$  magnitude close to the X-point in Figure 7j are therefore signatures of the system transitioning between the normal electron jet and the deflected electron flow respectively, in response to the variations in the magnetic field direction.

In addition to the various transient structures either directly associated with the convection of the  $B_y$  magnetic field through the outflow and/or the variations in the reconnection rate, we also see a much higher rate of island production in the varying run. One large island forming around time = 95 is clearly visible as it travels toward smaller  $x$  (downwards in Figure 7), but at least four smaller islands form during the simulation. It is possible that the formation of multiple islands is a consequence of the many reconfiguration iterations the system undergoes in response to the imposed variations in the inflow magnetic field. Variations in the reconnection rate, motion of



the reconnection site, and various asymmetries could all conspire to facilitate a higher rate of island production, which also makes the outflow in general more structured. The mere presence of a guide field will also cause the system to generate secondary islands at a higher rate than in a purely antiparallel scheme (Drake et al., 2006). We observe island generation while both regions with and without a guide field are reconnecting, but since these regions are fairly narrow, it is not possible to determine if it is the presence of a guide field alone or a synergy of it and its variations that generates the islands. The presence of secondary islands is also known to affect the reconnection rate (e.g., Cassak et al., 2017), and they are a likely cause of the smaller rate variations we see on top of the large scale behavior caused by the varying inflow conditions.

Typical values for the proton density in the magnetosheath are  $15\text{--}20\text{ cm}^{-3}$  (Toledo-Redondo et al., 2021), making one ion inertial length in our simulations about  $50\text{--}60\text{ km}$ . The larger scale structures we see in the magnetic and electric fields and the ion density vary in width between  $10$  and  $30 d_i$ , meaning they are in the range of  $500\text{--}1800\text{ km}$  wide. The smaller scale structures we see in the electron velocities and the ion density are just a few  $d_i$  wide, corresponding to a few hundreds of km.

## 6. Summary and Discussion

We have investigated how a system undergoing collisionless magnetic reconnection reacts to varying inflow conditions by asymmetrically varying the configuration of the magnetic field in the inflow region. We found that such variations have significant influence on both the larger and smaller scale dynamics of the reconnecting system, as we see correlated variations in the reconnection rate, the flux transport and the structure of the exhaust. To a large extent, the overall behavior of the reconnection rate was found to be dictated by the magnitude of the reconnecting component of the magnetic field, consistent with the general scaling developed by Cassak and Shay (2007). However, significant deviations from the behavior predicted by the scaling were also identified while reconnecting regions 1.1 and 2.1. We found that as the reconnecting components became asymmetric, the ion inflow velocity increased on the side where the reconnecting component was reduced. The increased inflow velocity reduces the effect of the lower magnitude of  $B_x$  on the reconnection rate by increasing the flux transport. This was possible because the magnetic tension force became asymmetric, being reduced in regions 1.1 and 2.1 as they approached the reconnection site, and increased right in front of the transition between regions with and without guide field. These dynamics caused  $z$ -directed convections of the reconnection site. In this study, we designed the simulation with varying guide fields on one side, similar to dayside reconnection with varying IMF. If the magnetic field variations were symmetric above and below the current sheet, the changes in velocity and flux transport would be the similar, but symmetric, and the X-point would not move.

We find the exhaust to be significantly less laminar when the inflow is varying, compared to a simulation with non-varying inflow conditions. Large scale structures of enhanced  $B_z$ ,  $E_y$ , and ion density propagate through the exhaust. These structures form on flux tubes that had no  $B_y$  in the inflow. In the magnetotail, regions of magnetic flux pile up, often referred to as dipolarizing flux bundles (where the dipolarization front is the leading edge), are often associated with a decrease in the density (e.g., J. Liu et al., 2013). This anticorrelation between  $B_z$  and  $n$  was observed for the first flux pile-up regions in both the baseline and varying runs. In contrast, the second flux pile-up region observed in the run with varying guide field was associated with a density increase. This conjugate increase of  $B_z$  and  $n$  is a result of the compression of flux tubes and the associated plasma. We would expect similar plasma compression to be present also at the first pile-up regions. However, in these regions, the decrease in density due to inflow density variations is much larger, and compressional effects are negligible in comparison.

It is clear that the reconnection process does not act as a filter for the variations in the inflow region. The imposed guide field variations are carried through the diffusion region and convected through the exhaust, as seen in Figure 7h. The variations in the magnitude of the  $B_z$  component clearly coincide in time with the variations in the magnitudes of the inflow magnetic field. However, as we saw in Section 3, the reconnection rate shows significant variations in response to the varying inflow magnetic field. These variations in reconnection rate can lead to the formation of such structures of enhanced  $B_z$ , as discussed in Section 5. Although the  $B_z$  structures coincide with the regions of low  $B_y$  in the outflow, we cannot with certainty rule out that this may be a feature of the initial spacing of the  $B_y$  bands in the inflow. Other sources of a varying reconnection rate could lead to similar structures in the outflow  $B_z$ .

The  $x$ -directed electron flows close to the X-point seen in the baseline run are significantly reduced in the varying run while reconnecting the regions containing  $B_y$ . As discussed in Section 5, the absence of these flows is a result of the variation in the magnetic field direction. The guide field modifies the trajectory of the electron flow to be directed along the separatrices, that is, outside of the  $z$ -range we show in our plots. Additionally, smaller scale structures and variations in the magnitude of the outflow velocity in both directions are seen. The reconnection rate in the varying run is in general slightly lower than in the baseline run, consistent with a reduced outflow of flux, and less of the original current sheet is therefore seen to be convected away from the X-point in the varying run. Additionally, a much higher rate of island production contributes to make the varying run less laminar. Based on this, it is possible to argue that some variations and turbulence measured in the outflow are simply remnants of a fluctuating inflow, rather than a product of some kinetic dynamics in the diffusion region.

In summary, the varying guide field impacts the reconnection process in multiple ways, both directly and indirectly. Direct impacts include variations of the reconnection rate, transmission of the guide field to the exhaust and related modifications of the electron flows. Indirect impacts includes formation of multiple regions of magnetic flux pile-up in the exhaust that are associated with density increases, and nonlinear modifications to the reconnection rate. The close relation between variations in the inflow and the dynamics of the reconnection process we have identified in this simulation study could be further established through observations if we had simultaneous measurements in the reconnection outflow and inflow. This could be accomplished for example, by modifying the configuration of MMS to include an upstream monitor, or through conjunctions of multiple spacecraft observatories.

## Data Availability Statement

Replication data for this study is available at (Spinnangr, 2021).

## Acknowledgments

This study was supported by NOTUR/NORSTOR under project NN9496K. CN and PT received support from the Research Council of Norway under contract 300865.

## References

- Akhavan-Tafti, M., Palmroth, M., Slavin, J. A., Battarbee, M., Ganse, U., Grandin, M., et al. (2020). Comparative analysis of the Vlasior simulation and MMS observations of multiple X-line reconnection and flux transfer events. *Journal of Geophysical Research: Space Physics*, *125*(7), e2019JA027410. <https://doi.org/10.1029/2019JA027410>
- Akhavan-Tafti, M., Slavin, J. A., Eastwood, J. P., Cassak, P. A., & Gershman, D. J. (2019). MMS multi-point analysis of FTE evolution: Physical characteristics and dynamics. *Journal of Geophysical Research: Space Physics*, *124*(7), 5376–5395. <https://doi.org/10.1029/2018JA026311>
- Burch, J. L., & Phan, T. D. (2016). Magnetic reconnection at the dayside magnetopause: Advances with MMS. *Geophysical Research Letters*, *43*(16), 8327–8338. <https://doi.org/10.1002/2016GL069787>
- Burch, J. L., Torbert, R. B., Phan, T. D., Chen, L. J., Moore, T. E., Ergun, R. E., & Chandler, M. (2016). Electron-scale measurements of magnetic reconnection in space. *Science*, *352*(6290), aaf2939. <https://doi.org/10.1126/science.aaf2939>
- Cassak, P. A., & Fuselier, S. A. (2016). *Reconnection at Earth's dayside magnetopause* (pp. 213–276). [https://doi.org/10.1007/978-3-319-26432-5\\_6](https://doi.org/10.1007/978-3-319-26432-5_6)
- Cassak, P. A., Liu, Y. H., & Shay, M. A. (2017). *A review of the 0.1 reconnection rate problem*. (Vol. 83). Cambridge University Press. <https://doi.org/10.1017/S0022377817000666>
- Cassak, P. A., & Shay, M. A. (2007). Scaling of asymmetric magnetic reconnection: General theory and collisional simulations. *Physics of Plasmas*, *14*(10), 102114. <https://doi.org/10.1063/1.2795630>
- Chen, L. J., Hesse, M., Wang, S., Gershman, D., Ergun, R. E., Burch, J., et al. (2017). Electron diffusion region during magnetopause reconnection with an intermediate guide field: Magnetospheric multiscale observations. *Journal of Geophysical Research: Space Physics*, *122*(5), 5235–5246. <https://doi.org/10.1002/2017JA024004>
- Comisso, L., & Bhattacharjee, A. (2016). On the value of the reconnection rate. *Journal of Plasma Physics*, *82*(6), 1–9. <https://doi.org/10.1017/S002237781600101X>
- Dargent, J., Aunai, N., Lavraud, B., Toledo-Redondo, S., & Califano, F. (2019). Signatures of cold ions in a kinetic simulation of the reconnecting magnetopause. *Journal of Geophysical Research: Space Physics*, *124*(4), 2497–2514. <https://doi.org/10.1029/2018JA026343>
- Dargent, J., Aunai, N., Lavraud, B., Toledo-Redondo, S., & Califano, F. (2020). Simulation of plasmaspheric plume impact on dayside magnetic reconnection. *Geophysical Research Letters*, *47*(4), e2019GL086546. <https://doi.org/10.1029/2019GL086546>
- Dargent, J., Aunai, N., Lavraud, B., Toledo-Redondo, S., Shay, M. A., Cassak, P. A., & Malakit, K. (2017). Kinetic simulation of asymmetric magnetic reconnection with cold ions. *Journal of Geophysical Research: Space Physics*, *122*(5), 5290–5306. <https://doi.org/10.1002/2016JA023831>
- Drake, J. F., Shay, M. A., & Swisdak, M. (2008). The Hall fields and fast magnetic reconnection. *Physics of Plasmas*, *15*(4), 042306. <https://doi.org/10.1063/1.2901194>
- Drake, J. F., Swisdak, M., Schoeffler, K. M., Rogers, B. N., & Kobayashi, S. (2006). Formation of secondary islands during magnetic reconnection. *Geophysical Research Letters*, *33*(13). <https://doi.org/10.1029/2006GL025957>
- Fuselier, S. A., Trattner, K. J., & Petrinec, S. M. (2011). Antiparallel and component reconnection at the dayside magnetopause. *Journal of Geophysical Research*, *116*(A10). <https://doi.org/10.1029/2011JA016888>
- Fuselier, S. A., Vines, S. K., Burch, J. L., Petrinec, S. M., Trattner, K. J., Cassak, P. A., et al. (2017). Large scale characteristics of reconnection diffusion regions and associated magnetopause crossings observed by MMS. *Journal of Geophysical Research: Space Physics*, *122*(5), 5466–5486. <https://doi.org/10.1002/2017JA024024>
- Goldman, M. V., Lapenta, G., Newman, D. L., Markidis, S., & Che, H. (2011). Jet deflection by very weak guide fields during magnetic reconnection. *Physical Review Letters*, *107*(13), 135001. <https://doi.org/10.1103/PhysRevLett.107.135001>

- Hesse, M., Liu, Y. H., Chen, L. J., Bessho, N., Kuznetsova, M., Birn, J., & Burch, J. L. (2016). On the electron diffusion region in asymmetric reconnection with a guide magnetic field. *Geophysical Research Letters*, *43*(6), 2359–2364. <https://doi.org/10.1002/2016GL068373>
- Hesse, M., Norgren, C., Tenfjord, P., Burch, J. L., Liu, Y. H., Bessho, N., et al. (2021). A new look at the electron diffusion region in asymmetric magnetic reconnection. *Journal of Geophysical Research: Space Physics*, *126*(2), e2020JA028456. <https://doi.org/10.1029/2020JA028456>
- Hesse, M., Schindler, K., Birn, J., & Kuznetsova, M. (1999). The diffusion region in collisionless magnetic reconnection. *Physics of Plasmas*, *6*(5), 1781–1795. <https://doi.org/10.1063/1.873436>
- Hesse, M., Zenitani, S., & Klimas, A. (2008). The structure of the electron outflow jet in collisionless magnetic reconnection. *Physics of Plasmas*, *15*(11), 112102. <https://doi.org/10.1063/1.3006341>
- Huba, J. D. (2005). Hall magnetic reconnection: Guide field dependence. *Physics of Plasmas*, *12*(1), 012322. <https://doi.org/10.1063/1.1834592>
- Kolstø, H., Hesse, M., Norgren, C., Tenfjord, P., Spinnangr, S. F., & Kwagala, N. (2020a). Collisionless magnetic reconnection in an asymmetric oxygen density configuration. *Geophysical Research Letters*, *47*(1), e2019GL085359. <https://doi.org/10.1029/2019GL085359>
- Kolstø, H., Hesse, M., Norgren, C., Tenfjord, P., Spinnangr, S. F., & Kwagala, N. (2020b). On the impact of a streaming oxygen population on collisionless magnetic reconnection. *Geophysical Research Letters*, *47*(22), e2020GL089462. <https://doi.org/10.1029/2020GL089462>
- Liu, J., Angelopoulos, V., Runov, A., & Zhou, X. Z. (2013). On the current sheets surrounding dipolarizing flux bundles in the magnetotail: The case for wedgetails. *Journal of Geophysical Research: Space Physics*, *118*(5), 2000–2020. <https://doi.org/10.1002/jgra.50092>
- Liu, Y. H., Hesse, M., Guo, F., Daughton, W., Li, H., Cassak, P. A., & Shay, M. A. (2017). Why does steady-state magnetic reconnection have a maximum local rate of order 0.1? *Physical Review Letters*, *118*(8), 085101. <https://doi.org/10.1103/PhysRevLett.118.085101>
- Norgren, C., Tenfjord, P., Hesse, M., Toledo-Redondo, S., Li, W.-Y., Xu, Y., et al. (2021). On the presence and thermalization of cold ions in the exhaust of antiparallel symmetric reconnection. *Frontiers in Astronomy and Space Sciences*, *8*. <https://doi.org/10.3389/fspas.2021.730061>
- Phan, T. D., Drake, J. F., Shay, M. A., Mozer, F. S., & Eastwood, J. P. (2007). Evidence for an elongated (>60 ion skin depths) electron diffusion region during fast magnetic reconnection. *Physical Review Letters*, *99*(25), 255002. <https://doi.org/10.1103/PhysRevLett.99.255002>
- Poh, G., Slavin, J. A., Lu, S., Le, G., Ozturk, D. S., Sun, W. J., et al. (2019). Dissipation of earthward propagating flux rope through reconnection with geomagnetic field: An MMS case study. *Journal of Geophysical Research: Space Physics*, *124*(9), 7477–7493. <https://doi.org/10.1029/2018JA026451>
- Pritchett, P. L. (2005). Onset and saturation of guide-field magnetic reconnection. *Physics of Plasmas*, *12*(6), 062301. <https://doi.org/10.1063/1.1914309>
- Pritchett, P. L., & Coroniti, F. V. (2004). Three-dimensional collisionless magnetic reconnection in the presence of a guide field. *Journal of Geophysical Research*, *109*(A1). <https://doi.org/10.1029/2003JA009999>
- Pritchett, P. L., & Mozer, F. S. (2009). Asymmetric magnetic reconnection in the presence of a guide field. *Journal of Geophysical Research*, *114*(11). <https://doi.org/10.1029/2009JA014343>
- Ricci, P., Brackbill, J. U., Daughton, W., & Lapenta, G. (2004). Collisionless magnetic reconnection in the presence of a guide field. *Physics of Plasmas*, *11*(8), 4102–4114. <https://doi.org/10.1063/1.1768552>
- Shuster, J. R., Chen, L. J., Hesse, M., Argall, M. R., Daughton, W., Torbert, R. B., & Bessho, N. (2015). Spatiotemporal evolution of electron characteristics in the electron diffusion region of magnetic reconnection: Implications for acceleration and heating. *Geophysical Research Letters*, *42*(8), 2586–2593. <https://doi.org/10.1002/2015GL063601>
- Spinnangr, S. F. (2021). *Replication data for: Asymmetrically varying guide field during magnetic reconnection: Particle-In-Cell simulations.* DataverseNO. <https://doi.org/10.18710/WGWLSE>
- Spinnangr, S. F., Hesse, M., Tenfjord, P., Norgren, C., Kolstø, H. M., Kwagala, N. K., & Jørgensen, T. M. (2021). The micro-macro coupling of mass-loading in symmetric magnetic reconnection with cold ions. *Geophysical Research Letters*, *48*(13). <https://doi.org/10.1029/2020GL090690>
- Swisdak, M., Drake, J. F., Shay, M. A., & McIlhargey, J. G. (2005). Transition from antiparallel to component magnetic reconnection. *Journal of Geophysical Research*, *110*(A5). <https://doi.org/10.1029/2004JA010748>
- Swisdak, M., Rogers, B. N., Drake, J. F., & Shay, M. A. (2003). Diamagnetic suppression of component magnetic reconnection at the magnetopause. *Journal of Geophysical Research*, *108*(A5). <https://doi.org/10.1029/2002JA009726>
- Tenfjord, P., Hesse, M., & Norgren, C. (2018). The formation of an oxygen wave by magnetic reconnection. *Journal of Geophysical Research: Space Physics*, *123*(11), 9370–9380. <https://doi.org/10.1029/2018JA026026>
- Tenfjord, P., Hesse, M., Norgren, C., Spinnangr, S. F., & Kolstø, H. (2019). The impact of oxygen on the reconnection rate. *Geophysical Research Letters*, *46*(12), 6195–6203. <https://doi.org/10.1029/2019GL082175>
- Tenfjord, P., Hesse, M., Norgren, C., Spinnangr, S. F., Kolstø, H., & Kwagala, N. (2020). Interaction of cold streaming protons with the reconnection process. *Journal of Geophysical Research: Space Physics*, *125*(6), e2019JA027619. <https://doi.org/10.1029/2019JA027619>
- Toledo-Redondo, S., André, M., Aunai, N., Chappell, C. R., Dargent, J., Fuselier, S. A., et al. (2021). Impacts of ionospheric ions on magnetic reconnection and Earth's magnetosphere dynamics. *Reviews of Geophysics*, *59*(3), e2020RG000707. <https://doi.org/10.1029/2020rg000707>
- Torbert, R. B., Burch, J. L., Phan, T. D., Hesse, M., Argall, M. R., Shuster, J., et al. (2018). Electron-scale dynamics of the diffusion region during symmetric magnetic reconnection in space. *Science*, *362*(6421), 1391–1395. <https://doi.org/10.1126/science.aat2998>
- Trattner, K. J., Burch, J. L., Ergun, R., Eriksson, S., Fuselier, S. A., Giles, B. L., et al. (2017). The MMS dayside magnetic reconnection locations during phase 1 and their relation to the predictions of the maximum magnetic shear model. *Journal of Geophysical Research: Space Physics*, *122*(12), 11991–12005. <https://doi.org/10.1002/2017JA024488>
- Trattner, K. J., Mulcock, J. S., Petrinec, S. M., & Fuselier, S. A. (2007). Probing the boundary between antiparallel and component reconnection during southward interplanetary magnetic field conditions. *Journal of Geophysical Research*, *112*(8), A08210. <https://doi.org/10.1029/2007JA012270>
- Wilder, F. D., Ergun, R. E., Burch, J. L., Ahmadi, N., Eriksson, S., Phan, T. D., et al. (2018). The role of the parallel electric field in electron-scale dissipation at reconnecting currents in the magnetosheath. *Journal of Geophysical Research: Space Physics*, *123*(8), 6533–6547. <https://doi.org/10.1029/2018JA025529>
- Zhou, M., Berchem, J., Walker, R. J., El-Alaoui, M., Deng, X., Cazzola, E., et al. (2017). Coalescence of macroscopic flux ropes at the subsolar magnetopause: Magnetospheric multiscale observations. *Physical Review Letters*, *119*(5), 1–6. <https://doi.org/10.1103/PhysRevLett.119.055101>

# Paper III

## Electron behavior around the onset of magnetic reconnection

S.F. Spinnangr, M. Hesse, P. Tenfjord, C. Norgren, H.M. Kolstø, N. Kwagala, T.M. Jørgensen, T. Phan

*Geophysical Research Letters*, Vol. 49, Issue 23 doi:10.1029/2022GL102209, 2022



# Geophysical Research Letters®

## RESEARCH LETTER

10.1029/2022GL102209

### Key Points:

- Signatures indicating reconnection onset can be identified in the electron distributions
- Onset signatures persist over extended spatial and temporal scales
- The particle distributions immediately preceding onset are characterized by features of non-gyrotropy and acceleration

### Supporting Information:

Supporting Information may be found in the online version of this article.

### Correspondence to:

S. F. Spinnangr,  
susanne.spinnangr@uib.no

### Citation:

Spinnangr, S. F., Hesse, M., Tenfjord, P., Norgren, C., Kolstø, H. M., Kwagala, N. K., et al. (2022). Electron behavior around the onset of magnetic reconnection. *Geophysical Research Letters*, 49, e2022GL102209. <https://doi.org/10.1029/2022GL102209>

Received 21 NOV 2022  
Accepted 1 DEC 2022

© 2022. The Authors.

This is an open access article under the terms of the [Creative Commons Attribution License](https://creativecommons.org/licenses/by/4.0/), which permits use, distribution and reproduction in any medium, provided the original work is properly cited.

## Electron Behavior Around the Onset of Magnetic Reconnection

Susanne F. Spinnangr<sup>1</sup>, Michael Hesse<sup>2</sup>, Paul Tenfjord<sup>1</sup>, Cecilia Norgren<sup>1</sup>, Håkon M. Kolstø<sup>1</sup>, Norah K. Kwagala<sup>1</sup>, Therese Moretto Jørgensen<sup>2</sup>, and Tai Phan<sup>3</sup>

<sup>1</sup>University of Bergen, Bergen, Norway, <sup>2</sup>NASA Ames Research Center, Mountain View, CA, USA, <sup>3</sup>Space Sciences Laboratory, UC Berkeley, Berkeley, CA, USA

**Abstract** We investigate the onset of magnetic reconnection, utilizing a fully kinetic Particle-In-Cell (PIC) simulation. Characteristic features of the electron phase-space distributions immediately before reconnection onset are identified. These include signatures of pressure non-gyrotropy in the velocity distributions, and lemon shaped distributions in the in-plane velocity directions. Further, we explain how these features form through particle energization by the out-of-plane electric field. Identification of these features in the distributions can aid in analysis of data where clear signatures of ongoing reconnection are not yet present.

**Plain Language Summary** In any environment where magnetic fields and charged particles interact, magnetic reconnection will occur if the conditions are favorable. Magnetic reconnection can be described as magnetic explosions, since it releases stored magnetic energy and converts it into heat and movement of the plasma particles. In this paper, we use numerical simulations to take a closer look at how the reconnection process initiates, a fundamental question still not fully understood.

### 1. Introduction

While magnetic reconnection is one of the most important energy conversion processes in our near space environment, on the Sun and in highly magnetized astrophysical plasmas, the question of what controls its onset is still not completely understood. Magnetic reconnection has been extensively modeled and observed in a large variety of plasma environments, such as planetary magnetospheres, the solar corona, astrophysical plasmas and in laboratories and fusion reactors on Earth (Yamada et al., 2010). If we want to understand how, where, and why magnetic reconnection occurs, we must understand what physical conditions are necessary for the onset of reconnection. It has been shown that magnetic reconnection needs thin current sheets to occur (e.g., Lui, 2004; Nakamura et al., 2006; Sitnov et al., 2019), but in-situ observations prove that this alone is not a sufficient criteria for reconnection onset (e.g., Paschmann et al., 2018; Phan et al., 2020; R. Wang et al., 2018).

The onset is difficult to study with spacecraft due to its explosive nature, and varied temporal and spatial scales. The majority of reconnection studies are performed at locations and times where the data already shows clear signatures of ongoing reconnection. These signatures include ion (e.g., Paschmann et al., 1979) and electron jets (Phan et al., 2007; Torbert et al., 2018), Hall magnetic and electric fields (Eastwood et al., 2010; Mozer et al., 2002; M. Øieroset et al., 2001; Wygant et al., 2005), and non-isotropic and non-gyrotropic particle distributions (e.g., Burch, Torbert, et al., 2016; Chen et al., 2016; Hesse et al., 2021; Li et al., 2019; Shuster et al., 2015; Z. Wang et al., 2019).

Some simulation studies have aimed to understand the physics of reconnection onset. Hesse et al. (2001) show that the presence of non-gyrotropy in the electron pressure is necessary for the generation of the diffusive electric field in the location where the X-line will form. This electron non-gyrotropy generates a linear instability of the system which eventually causes the onset of reconnection. A thorough study of the effect of the ion to electron mass ratio and the strength of the driving, was presented in Liu et al. (2014). They found that the slow change in  $B_z$  prior to onset, and the rapid evolution after onset were unaffected by the mass ratio. They did however find that the time of the reconnection onset was strongly influenced by the mass ratio. This difference in onset time allowed them to identify the instability leading to reconnection onset as electron tearing. The importance of electron dynamics in reconnection onset was even further emphasized by Lu et al. (2020), who show both through observation and simulation that full scale magnetic reconnection initiates from electron-only reconnection in the presence of a strong external driver.

In this study, we investigate the electron dynamics right before the initial formation of an X-line, to identify signatures that are indicative of an imminent onset of reconnection. Recognizing such signatures will aid in the classification of reconnecting and non-reconnecting current sheets, which can broaden our understanding of what conditions are necessary for reconnection onset. In the following section we describe our simulation setup. In Section 3, we identify when onset occurs, then we discuss onset signatures in the electron phase space distributions in Section 4, while Section 5 is a summary and discussion about our results.

## 2. Simulation Design

We simulate magnetic reconnection in the magnetotail using a fully kinetic, 2.5D Particle-In-Cell (PIC) simulation. In our coordinate system,  $x$  is the reconnection outflow direction,  $y$  is the initial current direction, and  $z$  is the inflow direction. Our simulation starts with a tail-like equilibrium (Birn et al., 1975) with oppositely directed magnetic fields and a current sheet with no perturbation. The initial magnetic field configuration is given by

$$B_x = \alpha(x) \tanh\left(\alpha(x) \frac{z}{l}\right) \quad (1)$$

$$B_z = \alpha'(x) \left(-z \tanh\left(\alpha(x) \frac{z}{l}\right) + \frac{l}{\alpha(x)}\right) \quad (2)$$

$$\alpha(x) = \left(1 + \frac{bx}{\gamma l}\right)^{-\gamma} \quad (3)$$

where  $l = 2 d_i$  is the half-width of the current sheet,  $b = 0.05$ , and  $\gamma = 0.6$ . To establish converging flow toward the current sheet, the top, bottom and left boundaries of the simulation domain are subjected to an electric field driver, given by

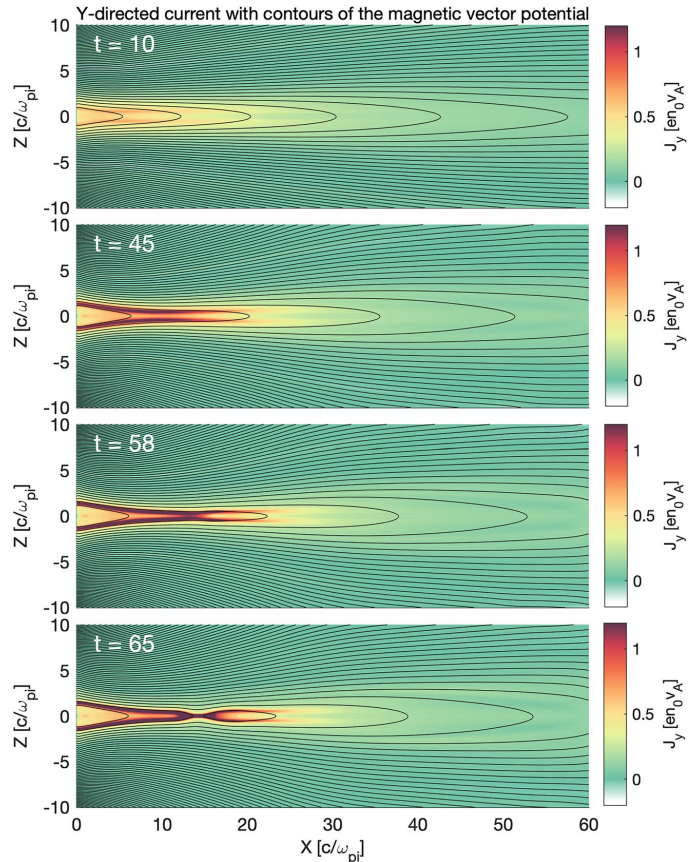
$$\text{Left : } E_x(x = 0, z, t) = \Gamma(t) \left(\frac{z}{z_{\max}}\right)^2 b_{xt} \quad (4)$$

$$\text{Top : } E_x(x, z = z_{\max}, t) = \Gamma(t) \left|\frac{x_{\max} - x}{x_{\max}}\right| b_{xt} \quad (5)$$

$$\text{Bottom : } E_b(x, z = -z_{\max}, t) = \Gamma(t) \left|\frac{x_{\max} - x}{x_{\max}}\right| b_{xb} \quad (6)$$

which increases the asymptotic magnetic field strength ( $B_x$ ) through Faraday's law and leads to current sheet thinning. The  $b_x$  terms are expressions for the  $z$ -average of  $B_x$  in the boundary cells,  $\Gamma(t) = \tanh(0.1t)/\cosh^2(0.1t)$ , and  $t$  is time. The electric field driver peaks around  $t = 7$  before it falls off, such that the driving phase is over around  $t = 35$ , long before the system eventually reconnects. Similar driving mechanisms that mimic the loading of magnetic flux in the inflow regions by the solar wind have been employed in previous studies, successfully resulting in reconnection (e.g., Hesse et al., 2001; Liu et al., 2014; Pritchett, 2005, 2010). The particular form of the driving can influence the timing of the onset and the location of the  $x$ -point, but the kinetic physics of the onset should remain unaffected when the driver is turned off early.

Lengths are normalized to the ion inertial length,  $d_i = \frac{c}{\omega_{pi}}$ , where  $\omega_{pi} = \sqrt{\frac{n_0 e^2}{\epsilon_0 m_i}}$  is the ion plasma frequency with  $n_0$  being the initial current sheet density and  $m_i$  is the ion mass. Time is normalized to the inverse ion cyclotron frequency,  $\Omega_i^{-1} = \frac{m_i}{e B_0}$ , where  $B_0$  is the initial asymptotic magnetic field. We employ a time step of  $\omega_{pe} \delta t = 1$ . Densities are normalized to  $n_0$ , velocities to the ion Alfvén velocity,  $v_A = B_0 / \sqrt{\mu_0 m_i n_0}$ , and kinetic energies to  $m_i v_A^2$ . The boundary conditions are reflective in both the inflow and outflow directions. We use a total of  $6.7 \times 10^9$  macro-particles. The size of the simulation domain is  $60 d_i \times 20 d_i$  divided into a grid of  $2,048 \times 1,024$  cells, resulting in about 3,200 particles per cell. The ions and electrons have a mass ratio of  $\frac{m_i}{m_e} = 100$  and their temperature ratio is  $\frac{T_e}{T_i} = 0.2$ . The ratio of the ion plasma frequency to the electron cyclotron frequency is  $\omega_{pe} / \Omega_e = 2$ .



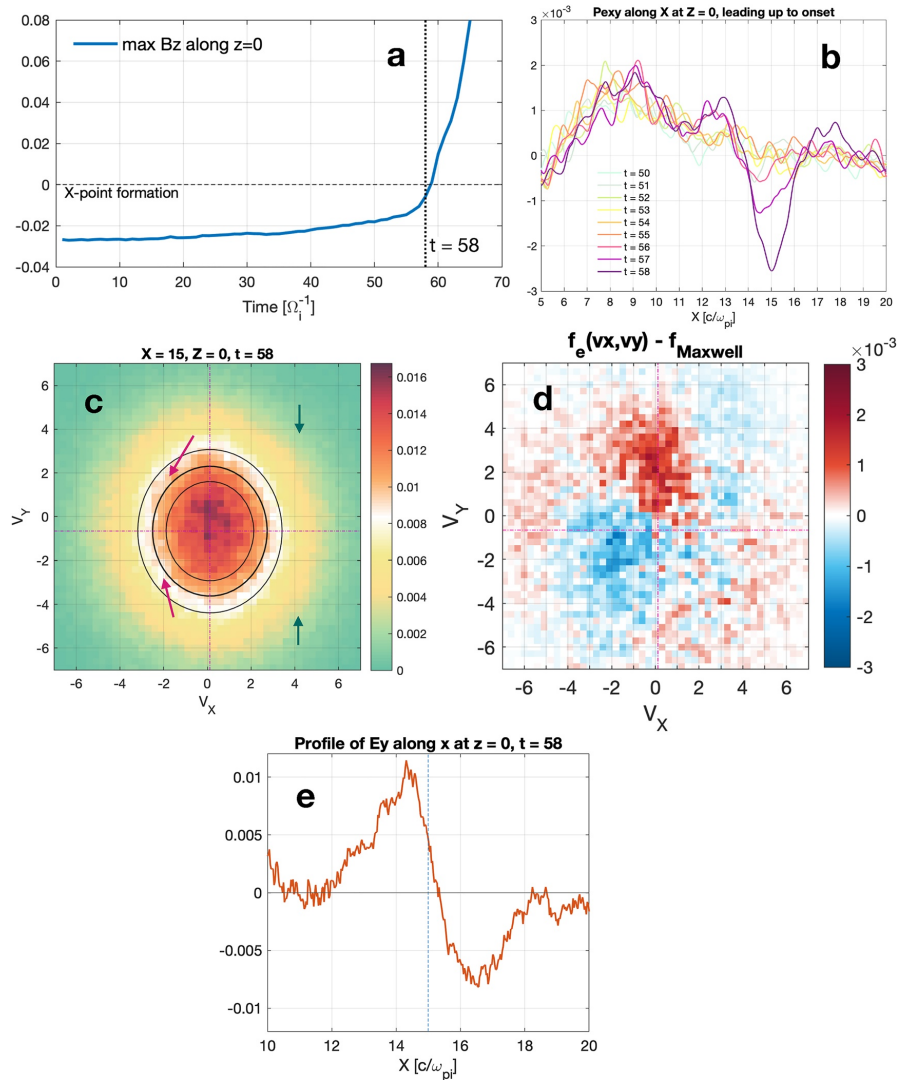
**Figure 1.** Evolution of the in-plane magnetic field (contours) and out-of-plane current density  $J_y$  (color). The current sheet becomes thinner and eventually reconnects. The penultimate panel shows the time of investigation,  $t = 58 \Omega_e^{-1}$ , discussed later in the paper.

In Figure 1 we show an overview of the in-plane magnetic field (contour lines) and out-of-plane current  $J_y$  (color), for four different times. We see how the thick current sheet becomes thinner as the magnetic field in the asymptotic regions become stronger, and that the thinning continues after the driving phase is over, until reconnection occurs. The penultimate panel in Figure 1 shows the simulation at the time ( $t = 58$ ) we will investigate in detail in the following analysis.

### 3. Onset of Reconnection

To investigate the onset of magnetic reconnection, we must first determine when onset occurs. We follow a similar tactic as employed in (Liu et al., 2014). In our set up, the direction of  $B_z$  is initially  $< 0$  everywhere. In order for  $B_z > 0$  to appear at the neutral plane ( $z = 0$ ), reconnection must have occurred. We therefore determine the time of investigation by finding the maximum value of  $B_z(x, z = 0)$  (Figure 2a), as a function of time. An X-line forms as the max value of  $B_z$  intersects 0, which is marked in the figure with a horizontal dotted line, after which reconnection is definitely ongoing. Liu et al. (2014) determined the onset time by comparing the behavior of  $B_z$  to a stable reference simulation in which reconnection did not occur. Onset was defined as the time when the behavior of  $B_z$  started to deviate significantly from this reference run, in which  $B_z$  just showed a smooth change





**Figure 2.** (a) Maximum value of  $B_z$  along  $z=0$  as a function of time. When we see a significant change in the slope of this value we are close to reconnection onset. We define the time of investigation as the last output time before the formation of the X-line (indicated by the dotted line). (b) Cut through  $z=0$  of  $P_{ey}$ , for different times leading up to the onset. The data has been averaged with a running mean in order to remove noise and extract the average behavior. We see the necessary gradient for the generation of a diffusive electric field starts to appear and grow bigger from  $t=56$ . (c)  $f_e(v_x, v_y)$  at  $x=15, z=0$  and  $t=58$ . The dotted pink lines show the bulk velocity. The three black contour lines show how the distribution would look if it was purely bi-Maxwellian. (d) The difference between the distribution in (c) and the corresponding bi-Maxwellian distribution. (e) The reconnection electric field along  $x$  at  $z=0$  and  $t=58$ . The data is averaged over  $0.5 d_i$  in the  $z$ -direction to reduce noise. We see that the amplitude of  $E_y$  is higher to the left of where the X-line forms than to the right. This is also true for earlier times (not shown).

with a fairly even slope. This is similar to what we see in Figure 2a until  $t \approx 55$ . We have chosen to treat the last output time of our simulation before the X-line forms as the time of investigation, to ensure that we will see the system in the immediate pre-reconnection state. The time of investigation is  $t=58$ , which is marked in Figure 2a with a vertical dotted line.

Next we study the off-diagonal electron pressure tensor. Magnetic reconnection can only happen in a small diffusion region where an electric field parallel to the current direction dominates the particle dynamics. This electric field is often referred to as the reconnection electric field or the diffusive electric field, and is necessary to break the frozen-in condition and allow particles to diffuse across magnetic field lines. This reconnection electric field is generated through the non-gyrotropic contributions of the electron pressure tensor (Hesse et al., 1999, 2001; Kuznetsova et al., 1998; Vasyliunas, 1975). In our setup, this electric field can be expressed as

$$E_y = -\frac{1}{n_e e} \left( \frac{\partial P_{exy}}{\partial x} + \frac{\partial P_{eyz}}{\partial z} \right). \quad (7)$$

The dominating contribution around reconnection onset comes from  $\partial P_{exy}/\partial x$  (Hesse et al., 2001). Figure 2b shows  $P_{exy}$  along the  $x$ -axis at  $z = 0$  for the times leading up to the reconnection onset. A clear increase in  $P_{exy}$  starts to form at  $t = 56$ , and a significant peak is present at  $x = 15$  and  $t = 58$ , the chosen time of investigation. The existence of this peak and consequently the gradient along  $x$  around it confirms that our choice of investigation time is appropriate. In the following analysis of the electron behavior, we will investigate phase space distributions centered around this peak in  $P_{exy}$ .

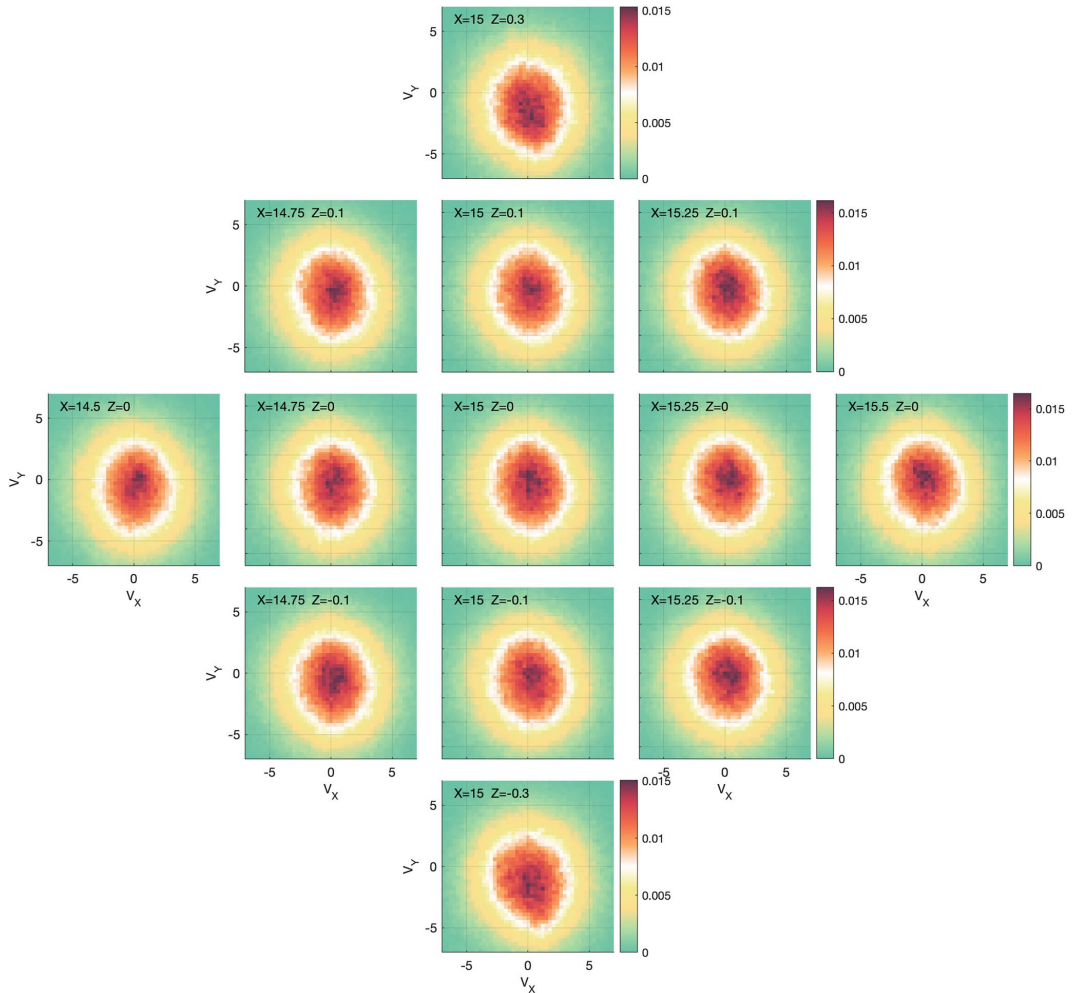
#### 4. Particle Behavior

In the preceding section we saw that a reconnection X-line forms close to  $x = 15$  and  $z = 0$ . To investigate the electron behavior leading up to onset, we select boxes centered around this point in which we construct the distribution functions in phase space. The boxes have  $dx = 0.125 d_i$  and  $dz = 0.05 d_i$  in each direction from their center value, such that the total length and height of each box is  $0.25 d_i$  and  $0.1 d_i$  respectively. The box sizes were chosen to optimize the resolution of the distributions without losing statistics by having too few particles in each box. Figures 3 and 4 show maps of the reduced distribution functions  $f_e(v_x, v_y)$  and  $f_e(v_x, v_z)$ , respectively, at  $t = 58$ . For completeness, a corresponding map in the  $v_y v_z$  plane is included as Figure S1. In the following, we will discuss features in these distributions.

As can be seen in Figure 3,  $f_e(v_x, v_y)$  is fairly similar in the different locations. This means that the features we will point out are present not only at the exact location where the X-line forms, but in a larger area around it. To aid in the analysis of the smaller scale electron behavior, we choose to use the center distribution as an example.

Figure 2c shows  $f_e(v_x, v_y)$  centered around  $x = 15$  and  $z = 0$ , at  $t = 58$ . The most prominent feature we see is a shift toward the negative  $v_y$ -direction. The two dotted pink lines show the bulk flow. Previously, we found that  $P_{exy} \neq 0$  at this location and time. We therefore expect the distribution to show non-gyrotropic features. However, since the relative magnitude of the non-gyrotropic pressure to the total pressure is small ( $P_{exy}/P_{exx} \approx 3\%$ ), these features are subtle. To make them easier to identify, we have overlaid the contours of a corresponding bi-Maxwellian distribution, centered at the bulk flow. As it is the higher energy parts of the distribution that provide the largest contribution to the pressure, we are more interested in the features we see further away from the center than the peak around the bulk flow. For particles with negative  $v_x$ , we see a clear asymmetry between the top and bottom quadrants, indicated by the two magenta arrows. A similar, but opposite asymmetry is found for particles with positive  $v_x$  where the green arrows are pointing. If we imagine the distribution is divided vertically along the  $x$ -directed bulk flow into two semicircles, we see that the result of the asymmetries is that the two halves are shifted along the  $v_y$ -direction with respect to each other. A similar feature was found by Hesse et al. (2011) for guide field reconnection. An additional way of illustrating this is provided in Figure 2d, showing the difference between the distribution and the corresponding bi-Maxwellian from 2c.

We can explain the shifted semicircles by investigating the history of the particles making up the distribution. In Figure 2e we show a cut of  $E_y(x, z = 0, t = 58)$ . The data has been averaged over  $\pm 0.5 d_i$  in the inflow direction to reduce noise. The dotted blue line shows the  $x$ -location of the box in which we took the discussed distribution. As we can see,  $E_y$  is positive in this location, as well as to the left of it, while it turns negative to the right at  $x > 15.3$ . In the region  $z = 0, x > 18$ ,  $E_y = -(\mathbf{v}_e \times \mathbf{B})_y$  (not shown), as the formation of a local minimum in  $B_z$  causes the frozen-in electrons to convect tailwards here. However, the reversal we see between  $x = 12$  and  $x = 18$  is also supported by the pressure divergence and the temporal inertia. The electrons are accelerated anti-parallel to  $E_y$ . This means that the electrons entering the box centered at  $x = 15$  from the right with negative  $v_x$  are accelerated in the positive  $y$ -direction, while electrons entering from the left with positive  $v_x$  are accelerated in the

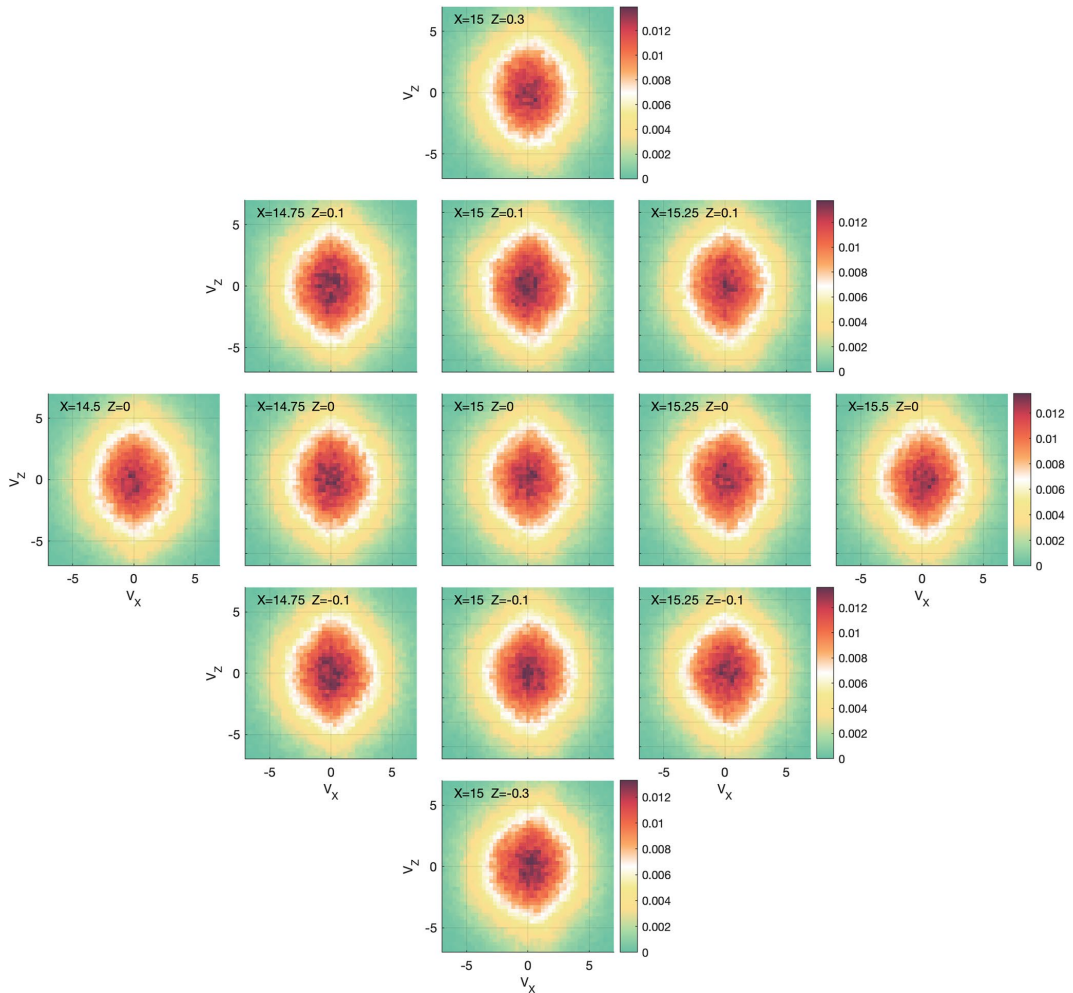


**Figure 3.** Reduced distributions  $f_e(v_x, v_y)$  centered around the point where the contribution to the reconnection electric field from the non-gyrotropic pressure reaches a maximum at  $t = 58$ . The location of the center of each box is given in the top left corner of each distribution.

negative  $y$ -direction. Additionally, the magnitude of  $E_y$  is on average slightly higher to the left of the box location than to the right. This means that particles entering this location from the left with positive  $v_x$  have on average experienced more acceleration by  $E_y$  than the particles coming from the right with negative  $v_x$ . This explains the non-gyrotropic feature of  $f_e(v_x, v_y)$ .

This feature is visible along the  $z = 0$  plane, but as can be seen in Figure 3, it is even clearer as we move out in the inflow direction. This is likely because the magnitude of  $E_y$  is greater at the boundaries where we see a larger gradient in  $B_x$ , which we will discuss below.

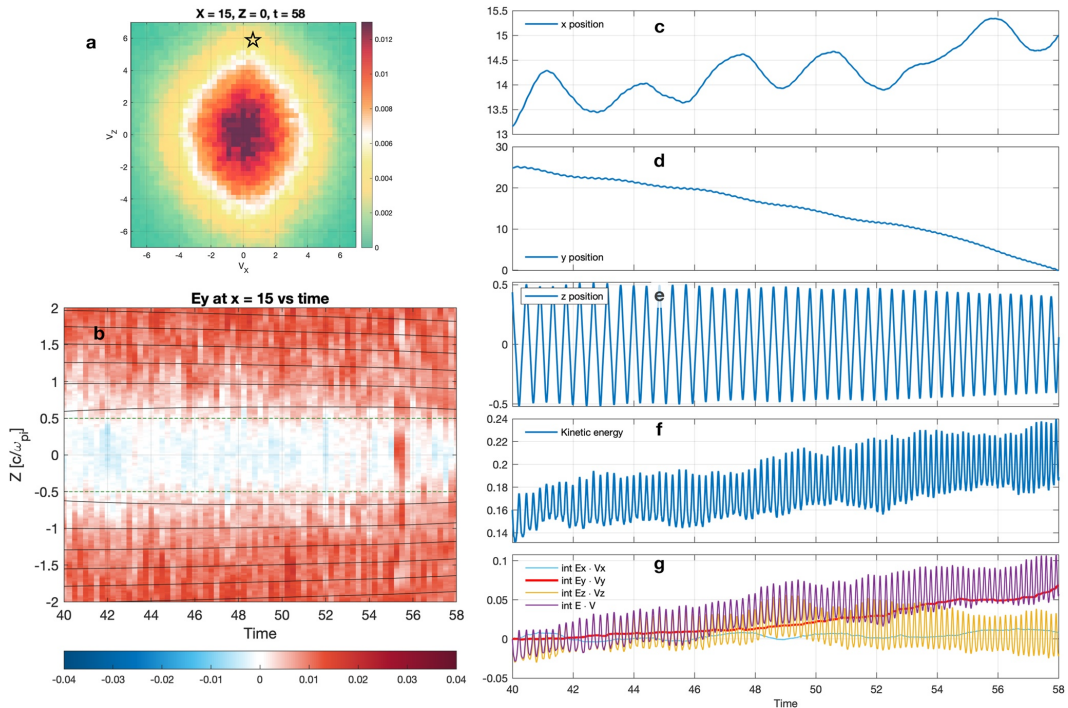
Figure 4 shows a map of  $f_e(v_x, v_z)$  for the same locations as in Figure 3. As with  $f_e(v_x, v_y)$ , we see that the distributions display fairly similar features in all the locations. The most prominent feature is an elongation along the  $v_z$ -axis around  $v_x = 0$ , resulting in lemon-shaped distributions. This tells us that particles with none or very small



**Figure 4.** A map of  $f_i(v_x, v_z)$  for the same boxes as in Figure 3 at  $t = 58$ .

$v_x$  are experiencing larger acceleration in the  $z$ -direction. To explain this lemon shape, we investigate how the particles are being energized.

In Figure 5 we again choose the distribution at  $x = 15$ ,  $z = 0$  as an example to discuss the features we see in all the distributions in Figure 4. In Figure 5a, we have chosen a test-particle to trace backwards in time to investigate how it gained the accelerated  $v_z$ , indicated by the star. Figure 5c through 5g show the particle position, kinetic energy, and the work done on the particle by the electric field,  $-\int \mathbf{E} \cdot \mathbf{v} dt$ , from a time long before the onset up to the investigation time. We see that the particle has a general drift in the negative  $y$ -direction, while it is bouncing in the  $z$ -direction and mirroring in the  $x$ -direction. The amplitude of the bouncing in  $z$  is fairly constant through the full time interval, although we do see a general change toward smaller amplitudes from about  $t = 54$  and onward. Figure 5b shows cuts along  $z$ , through  $x = 15$ , of  $E_y$  averaged over  $0.5 d_i$  in  $x$ , plotted as a function of time. The black contour lines are the contours of the magnetic vector potential, indicating the motion of the magnetic field at this  $x$ . The two green dotted lines indicate where  $z = 0.5 d_i$  for comparison with the particle position. We see



**Figure 5.** (a)  $f_s(v_x, v_z)$  at  $x = 15, z = 0, t = 58$ . (b) Slices along  $z$  at  $x = 15$  of  $E_y$  (averaged over  $0.5 d_i$  in  $x$ ), plotted as a function of time, with contours of the magnetic potential. (c–g) Position, kinetic energy and  $\int \mathbf{E} \cdot d\mathbf{v}$  for a test-particle, as a function of time.

that  $E_y$  is mostly negative and close to 0 in the center, while it is positive and with a larger amplitude further out. This is consistent with the evolution of the thinning current layer. The boundary between the positive and negative  $E_y$  regions is fairly stationary until around  $t = 56$ , when it starts to move inwards. The short burst of positive  $E_y$  in the center just before this is a transient, temporary, large-scale fluctuation that dissipates before the time of investigation, possibly caused by reflecting waves resulting from the driving.

Comparing the position of the turning point in the  $z$ -direction with the shape of the  $E_y$  profile, we see that it coincides with the region where  $E_y$  turns positive. A closer look at the work terms in Figure 5g reveals that the increase in kinetic energy comes from interactions with  $E_y$ , which results from the changing  $B_x$ . As the current sheet thins,  $B_x$  above and below it increases and propagates toward the center. This leads to a build up of  $E_y$  through Faraday's law. At the turning points in  $z$ , the particle motion is parallel to  $E_y$ , leading to energy gain through  $\mathbf{E} \cdot \mathbf{v}$ , as can be seen in Figure 5g. As the particle continues its meandering motion, this energy gain by  $E_y$  is turned into an increased  $v_z$  through the Lorentz force,  $e v_y B_x$ . The acceleration by  $E_y$  thus manifests as the lemon shaped distribution in the  $f_s(v_x, v_z)$ . In Figure 5b, we also see the contours of the magnetic field start to move inwards and become closer together, with an increasing rate after about  $t = 54$ . Comparing this to the movement of the particle in  $z$ , we see the same behavior in the amplitude of the meandering motion. This shows that the particle bounces between the magnetic walls of the inflow magnetic field. As the meandering in  $z$  and the propagation of the magnetic walls are oppositely aligned, this energy gain through  $E_y$  can also be described as simple Fermi acceleration (Fermi, 1949; Northrop, 1963). Fermi acceleration between moving regions of increased magnetic field is a common acceleration mechanism in space plasmas in general, and has recently been used to describe acceleration of electrons inside magnetic islands (Drake et al., 2006) and between merging flux ropes (Arnold et al., 2021).

## 5. Summary and Discussion

This study is part of a larger effort to understand why, when and where magnetic reconnection occurs. To answer these questions we must understand why some current sheets reconnect while others do not. The results of this study may help to expand our pool of data to investigate in this regard. By being able to identify current sheets that are close to or at reconnection onset, data from current sheet observations that were previously discarded since they do not show signatures of ongoing reconnection could be included in analyses of reconnecting current sheets.

We identified two key signatures of reconnection onset in the electron distribution functions in our simulation. The first is non-gyrotropy in  $f_e(v_x, v_y)$ , seen as shifted semicircles along the  $y$ -directed bulk flow, consistent with the necessary gradient in the non-gyrotropic electron pressure contribution to the reconnecting electric field. The second signature is lemon shaped distributions in  $f_e(v_x, v_z)$  due to Fermi acceleration of the electrons bouncing between the inward propagating magnetic field of the inflow regions. Later in our simulation (not shown), the electron distributions transition to exhibit the typical signatures of active reconnection, such as distinct counter-streaming electrons in the direction normal to the current sheet, cigar shapes in the inflow region and emerging crescents (e.g., Egedal et al., 2013; Shuster et al., 2015; Torbert et al., 2018). In principle, it is possible that lemon shapes in  $f_e(v_x, v_z)$  could be generated in a non-reconnecting, thinning current sheet. Therefore, we note that both the non-gyrotropy and lemon shapes should be present simultaneously in a thinning current sheet for it to be an indicator of reconnection onset.

In our setup, the onset signatures are clear. We have confirmed that the results discussed in this paper are not affected by the boundary conditions. The temporal resolution of the Magnetospheric Multiscale satellites (MMS) is on electron scales (Burch, Moore, et al., 2016; Pollock et al., 2016), which is high enough that the signatures could be resolved. If we assume  $B_0 = 20$  nT and  $n_0 \sim 0.3\text{--}0.8$  cm<sup>-3</sup> (Toledo-Redondo et al., 2021), one ion cyclotron time in our simulation corresponds to about 3 s, and one ion inertial length corresponds to 255–420 km. The identified onset signatures in our simulation persist over several ion times and at least a full ion inertial length around the forming X-line, which increases the probability of detection. Identifying currents sheets that show signs of being close to reconnection onset would enable us to include them in research of reconnecting currents sheets, which might further our understanding of which conditions are necessary for reconnection to occur.

## Data Availability Statement

The data used in this study was created using Fortran90. Replication data and instructions on how to use it is available at the data repository site DataverseNO, via Spinnangr (2022).

## Acknowledgments

This study was supported by NOTUR/NORSTOR under project NN4946K. SFS, CN, PT, and HK received support from the Research Council of Norway under contract 300865.

## References

- Arnold, H., Drake, J. F., Swisdak, M., Guo, F., Dahlin, J. T., Chen, B., et al. (2021). Electron acceleration during macroscale magnetic reconnection. *Physical Review Letters*, *126*(13), 135101. <https://doi.org/10.1103/PhysRevLett.126.135101>
- Birn, J., Sommer, R., & Schindler, K. (1975). Open and closed magnetospheric tail configurations and their stability. *Astrophysics and Space Science*, *35*(2), 389–402. <https://doi.org/10.1007/bf00637005>
- Burch, J. L., Moore, T. E., Torbert, R. B., & Giles, B. L. (2016). Magnetospheric multiscale overview and science objectives. *Space Science Reviews*, *199*(No. 1–4), 5–21. <https://doi.org/10.1007/s11214-015-0164-9>
- Burch, J. L., Torbert, R. B., Phan, T. D., Chen, L. J., Moore, T. E., Ergun, R. E., et al. (2016). Electron-scale measurements of magnetic reconnection in space. *Science*, *352*(6290). <https://doi.org/10.1126/science.aaf2939>
- Chen, L. J., Hesse, M., Wang, S., Bessho, N., & Daughton, W. (2016). Electron energization and structure of the diffusion region during asymmetric reconnection. *Geophysical Research Letters*, *43*(6), 2405–2412. <https://doi.org/10.1002/2016GL068243>
- Drake, J. F., Swisdak, M., Schoeffler, K. M., Rogers, B. N., & Kobayashi, S. (2006). Formation of secondary islands during magnetic reconnection. *Geophysical Research Letters*, *33*(13), 10–13. <https://doi.org/10.1029/2006GL025957>
- Eastwood, J. P., Phan, T. D., Øieroset, M., & Shay, M. A. (2010). Average properties of the magnetic reconnection ion diffusion region in the Earth's magnetotail: The 2001–2005 Cluster observations and comparison with simulations. *Journal of Geophysical Research*, *115*(8), 1–13. <https://doi.org/10.1029/2009JA014962>
- Egedal, J., Le, A., & Daughton, W. (2013). A review of pressure anisotropy caused by electron trapping in collisionless plasma, and its implications for magnetic reconnection. *Physics of Plasmas*, *20*(6), 1–18. <https://doi.org/10.1063/1.4811092>
- Fermi, E. (1949). On the origin of the cosmic radiation. *Physical Review*, *75*(8), 1169–1174. <https://doi.org/10.1063/1.3066619>
- Hesse, M., Kuznetsova, M., & Birn, J. (2001). Particle-in-cell simulations of three-dimensional collisionless magnetic reconnection. *Journal of Geophysical Research*, *106*(A12), 29831–29841. <https://doi.org/10.1029/2001ja000075>
- Hesse, M., Neukirch, T., Schindler, K., Kuznetsova, M., & Zenitani, S. (2011). The diffusion region in collisionless magnetic reconnection. *Space Science Reviews*, *160*(1–4), 3–23. <https://doi.org/10.1007/s11214-010-9740-1>

- Hesse, M., Norgren, C., Tenfjord, P., Burch, J. L., Liu, Y. H., Bessho, N., et al. (2021). A new look at the electron diffusion region in asymmetric magnetic reconnection. *Journal of Geophysical Research: Space Physics*, *126*(2), 1–16. <https://doi.org/10.1029/2020JA028456>
- Hesse, M., Schindler, K., Birn, J., & Kuznetsova, M. (1999). The diffusion region in collisionless magnetic reconnection. *Physics of Plasmas*, *6*(5), 1781–1795. <https://doi.org/10.1063/1.873436>
- Kuznetsova, M. M., Hesse, M., & Winske, D. (1998). Kinetic quasi-viscous and bulk flow inertia effects in collisionless magnetotail reconnection. *Journal of Geophysical Research*, *103*(A1), 199–213. <https://doi.org/10.1029/97ja02699>
- Li, X., Wang, R., Lu, Q., Hwang, K. J., Zong, Q., Russell, C. T., & Wang, S. (2019). Observation of nongyrotropic electron distribution across the electron diffusion region in the magnetotail reconnection. *Geophysical Research Letters*, *46*(24), 14263–14273. <https://doi.org/10.1029/2019GL085014>
- Liu, Y. H., Birn, J., Daughton, W., Hesse, M., & Schindler, K. (2014). Onset of reconnection in the near magnetotail: PIC simulations. *Journal of Geophysical Research: Space Physics*, *119*(12), 9773–9789. <https://doi.org/10.1002/2014JA020492>
- Lu, S., Wang, R., Lu, Q., Angelopoulos, V., Nakamura, R., Artemyev, A. V., et al. (2020). Magnetotail reconnection onset caused by electron kinetics with a strong external driver. *Nature Communications*, *11*(1), 1–7. <https://doi.org/10.1038/s41467-020-18787-w>
- Lui, A. T. Y. (2004). Potential plasma instabilities for substorm expansion onsets. *Space Science Reviews*, *113*(1/2), 127–206. <https://doi.org/10.1023/b:spac.0000042942.00362.4e>
- Mozer, F. S., Bale, S. D., & Phan, T. D. (2002). Evidence of diffusion regions at a subsolar magnetopause crossing. *Physical Review Letters*, *89*(1), 1–4. <https://doi.org/10.1103/PhysRevLett.89.015002>
- Nakamura, R., Baumjohann, W., Runov, A., & Asano, Y. (2006). Thin current sheets in the magnetotail observed by cluster. *Space Science Reviews*, *122*(1–4), 29–38. <https://doi.org/10.1007/s11214-006-6219-1>
- Northrop, T. G. (1963). Adiabatic charged-particle motion. *Reviews of Geophysics*, *1*(August), 283. <https://doi.org/10.1029/rg001i003p00283>
- Øieroset, M., Phan, T. D., Fujimoto, M., Lin, R. P., & Lepping, R. P. (2001). In situ detection of reconnection in the Earth's magnetotail. *Nature*, *412*(July), 414–417. <https://doi.org/10.1038/35086520>
- Paschmann, G., Haaland, S. E., Phan, T. D., Sonnerup, B. U., Burch, J. L., Torbert, R. B., et al. (2018). Large-scale survey of the structure of the dayside magnetopause by MMS. *Journal of Geophysical Research: Space Physics*, *123*(3), 2018–2033. <https://doi.org/10.1002/2017JA025121>
- Paschmann, G., Sonnerup, B. U., Papamastorakis, I., Scopke, N., Haerendel, G., Bame, S. J., et al. (1979). Plasma acceleration at the Earth's magnetopause: Evidence for reconnection. *Nature*, *282*(5736), 243–246. <https://doi.org/10.1038/282243a0>
- Phan, T. D., Bale, S. D., Eastwood, J. P., Lavraud, B., Drake, J. F., Øieroset, M., et al. (2020). Parker solar probe in situ observations of magnetic reconnection exhausts during encounter 1. *The Astrophysical Journal - Supplement Series*, *246*(2), 34. <https://doi.org/10.3847/1538-4365/ab55ee>
- Phan, T. D., Drake, J. F., Shay, M. A., Mozer, F. S., & Eastwood, J. P. (2007). Evidence for an elongated (>60 ion skin depths) electron diffusion region during fast magnetic reconnection. *Physical Review Letters*, *99*(25), 1–4. <https://doi.org/10.1103/PhysRevLett.99.255002>
- Pollock, C., Moore, T., Jacques, A., Burch, J., Gliese, U., Saito, Y., et al. (2016). Fast plasma investigation for magnetospheric multiscale. *Space Science Reviews*, *199*(1–4), 331–406. <https://doi.org/10.1007/s11214-016-0245-4>
- Pritchett, P. L. (2005). Externally driven magnetic reconnection in the presence of a normal magnetic field. *Journal of Geophysical Research*, *110*(A5), A05209. <https://doi.org/10.1029/2004JA010948>
- Pritchett, P. L. (2010). Onset of magnetic reconnection in the presence of a normal magnetic field: Realistic ion to electron mass ratio. *Journal of Geophysical Research*, *115*(10), 1–9. <https://doi.org/10.1029/2010JA015371>
- Shuster, J. R., Chen, L. J., Hesse, M., Argall, M. R., Daughton, W., Torbert, R. B., & Bessho, N. (2015). Spatiotemporal evolution of electron characteristics in the electron diffusion region of magnetic reconnection: Implications for acceleration and heating. *Geophysical Research Letters*, *42*(8), 2586–2593. <https://doi.org/10.1002/2015GL063601>
- Sitnov, M., Birn, J., Ferdousi, B., Gordeev, E., Khotyaintsev, Y., Merkin, V., et al. (2019). Explosive magnetotail activity. *Space Science Reviews*, *215*(4), 31. <https://doi.org/10.1007/s11214-019-0599-5>
- Spinnangr, S. F. (2022). Replication data for: Electron behaviour around the onset of magnetic reconnection. *DataverseNO*. <https://doi.org/10.18710/Z2XUSW>
- Toledo-Redondo, S., André, M., Aunai, N., Chappell, C. R., Dargent, J., Fuselier, S. A., et al. (2021). Impacts of ionospheric ions on magnetic reconnection and Earth's magnetosphere dynamics. *Reviews of Geophysics*, *59*(3). <https://doi.org/10.1029/2020rg000707>
- Torbert, R. B., Burch, J. L., Phan, T. D., Hesse, M., Argall, M. R., Shuster, J., et al. (2018). Electron-scale dynamics of the diffusion region during symmetric magnetic reconnection in space. *Science*, *362*(6421), 1391–1395. <https://doi.org/10.1126/science.aat2998>
- Vasyliunas, V. M. (1975). Theoretical models of magnetic field line merging. *Reviews of Geophysics*, *13*(1), 303–336. <https://doi.org/10.1029/RG013i001p00303>
- Wang, R., Lu, Q., Nakamura, R., Baumjohann, W., Huang, C., Russell, C. T., et al. (2018). An electron-scale current sheet without bursty reconnection signatures observed in the near-earth tail. *Geophysical Research Letters*, *45*(10), 4542–4549. <https://doi.org/10.1002/2017GL076330>
- Wang, Z., Fu, H. S., Liu, C. M., Liu, Y. Y., Cozzani, G., Giles, B. L., et al. (2019). Electron distribution functions around a reconnection X-line resolved by the FOTE method. *Geophysical Research Letters*, *46*(3), 1195–1204. <https://doi.org/10.1029/2018GL081708>
- Wygant, J. R., Cattell, C. A., Lysak, R., Song, Y., Dombek, J., McFadden, J., et al. (2005). Cluster observations of an intense normal component of the electric field at a thin reconnecting current sheet in the tail and its role in the shock-like acceleration of the ion fluid into the separatrix region. *Journal of Geophysical Research*, *110*(A9), 1–30. <https://doi.org/10.1029/2004JA010708>
- Yamada, M., Kulsrud, R., & Ji, H. (2010). Magnetic reconnection. *Reviews of Modern Physics*, *82*(1), 603–664. <https://doi.org/10.1103/RevModPhys.82.603>



Graphic design: Communication Division, UIB / Print: Skjipes Kommunikasjon AS



[uib.no](http://uib.no)

ISBN: 9788230841983 (print)  
9788230856215 (PDF)